



TECHNISCHE
UNIVERSITÄT
WIEN



Master thesis

Metrological Characterization of the Intel RealSense D415 Stereo Depth Camera for Additive Manufacturing

carried out for the purpose of obtaining a Double Degree Master Program held by EIT Manufacturing Master School in the specialization People and Robots for Sustainable Work (PR) with partner universities Mondragon Unibertsitatea (Entry University) and Technische Universität Wien (Exit University)

under the supervision of

Univ.-Prof. Dr.-Ing. Markus Vincze

(Vision for Robotics Group)

and

Univ.-Prof. Dr.-Ing. Eñaut Muxika Olasagasti

(Mondragon Group)

submitted to

Technische Universität Wien

Faculty of Mechanical Engineering and Business Administration

and

Mondragon Unibertsitatea

Faculty of Engineering

from

Shaheem Ahmed Khan

Matr. no. 12202193 (TU Wien) and 44065 (MU)

Vienna, September 2024

Shaheem Ahmed Khan



TECHNISCHE
UNIVERSITÄT
WIEN



I therefore acknowledge the printing of my work under the designation

Master Thesis

is only authorized with the approval of the examination board.

I also declare in lieu of an oath that I have carried out my diploma thesis independently according to the recognized principles for scientific papers and have named all the aids used, in particular the literature on which they are based.

As a part of the dual Master program, I also authorize EIT Manufacturing Master School, Mondragon Unibertsitatea and Technische Universität Wien to publish the work in this thesis with discretion of my permission.

Furthermore, I declare that I have not submitted this thesis topic either in Austria or abroad (to an assessor for assessment) in any form as an examination paper and that this work corresponds to the work assessed by the assessor.

Vienna, September 2024

Shaheem Ahmed Khan

Acknowledgement

I would like to express my deepest gratitude to my supervisors from both Technische Universität Wien and Mondragon Unibertsitatea. First and foremost, I extend my sincerest thanks to Dr. Markus Vincze, whose expertise and insightful feedback helped shape my work and deepen my understanding of the subject matter. I am equally grateful to Professor Eñaut Muxika Olasagasti, whose invaluable guidance, support, and encouragement have been essential to the successful completion of this thesis. Your mentorship has been an indispensable asset throughout this journey.

I would also like to extend my heartfelt thanks to my family, whose unwavering love and support have carried me through this demanding process. To my parents, Mr. Mehmood Ahmed Khan and Ms. Fareeha Niazi, your endless encouragement and belief in me have been a constant source of strength. To my siblings, Mr. Humza Khan and Ms. Wajeeha Mehmood, thank you for your patience and understanding during the times when my focus was elsewhere.

I am equally grateful to my friends and colleagues at both universities. Your camaraderie and support made the challenging moments bearable, and your encouragement helped make the successes even more meaningful. Your contributions have profoundly impacted my academic journey, and I am forever humbled by your support.

Finally, I would like to express my appreciation to Matthias Hirschmanner for providing the template that served as the foundation for formatting this thesis. Your contribution was an essential part of completing this work.

Thank you all for your support and guidance throughout this journey.

Abstract

Additive manufacturing has emerged as a disruptive technology for producing complex and customized components across various industries. As the demand for high-quality parts grows, the need for robust quality inspection methods becomes critical. This master's thesis investigates the feasibility and accuracy of utilizing a single stereo camera system, specifically the Intel RealSense D415, for quality assessment of miniature components derived from the additive manufacturing process. Unlike traditional inspection techniques that primarily focus on dimensional inaccuracies and defects, this research introduces a novel evaluation approach, termed the Stereo Accuracy Assessment in Additive Manufacturing via Plane Fitting (SAAPF), designed to verify the accuracy of stereovision cameras for uniform, low-texture parts with millimeter-scale dimensions at close-range distances of 50 cm. The methodology involves creating CAD models, producing them via additive manufacturing using the Ultimaker Connect 2+, and capturing point cloud data with the Intel RealSense D415. The data is analyzed using the Intel RealSense Viewer and CloudCompare software, with accuracy assessed through plane fitting, cloud-to-cloud distance, and Gaussian distribution techniques. The research contributes a structured process for evaluating the camera's resolution limits and accuracy in this specific application. If validated, this approach could be integrated into additive manufacturing systems, paving the way for next-generation 3D printers with built-in precision quality control capabilities.

Keywords: Intel RealSense D415, 3D printing, additive manufacturing, quality control, point cloud, accuracy metrics

Contents

1	Introduction	1
1.1	Challenge	1
1.2	Contribution	2
1.3	Thesis Outline	3
2	State of the Art	4
2.1	Search Criteria	4
2.2	Literature	5
2.2.1	Evaluation Criteria	6
2.2.2	Summary of Evaluation Metrics	7
2.2.3	Stereo Vision-Based Depth-Sensing Technologies	8
2.2.4	Time-of-Flight (ToF) and LiDAR-Based Depth-Sensing Technologies	9
2.2.5	Cross-Technology Studies	10
3	Background	15
3.1	Camera Operation and Working Principle	15
3.2	Camera Models	17
3.2.1	Pinhole camera model	17
3.2.2	Central projection model	18
3.2.3	Camera Calibration Parameters	19
	Principal Point Offset	19
	Effective Focal Length	19
	Skew	20
	Intrinsic Parameters	20
	Extrinsic Parameters	21
3.2.4	Complete Camera Model	21
3.3	Stereo Vision	22
	Passive stereo vision	22
	Active stereo vision	22
3.3.1	Stereo vision fundamentals	22
3.3.2	Epipolar Geometry	23
	Epipoles	24
3.3.3	Fundamental and Essential Matrices	25
	Nomralized Image Coordinates	25
	Essential Matrix	26
	Fundamental Matrix	26
3.3.4	Stereo Calibration	26
3.3.5	Distortion	28
	Radial Distortion	28
	Tangential Distortion	28

3.3.6	Image Rectification	29
3.3.7	Stereo 3D reconstruction pipeline	30
3.4	PointCloud	30
4	SAAPF Framework	32
4.1	Evaluative Techniques in the SAAPF Framework	32
4.2	Hardware Components	33
4.2.1	Ultimaker 2+	33
4.2.2	Staircase Reference Models	34
4.2.3	Camera Setup	34
4.3	Software Components	36
4.3.1	RealSense Viewer	36
4.3.2	CloudCompare	36
4.4	Preliminary Setup	38
4.4.1	Camera Calibration	39
4.4.2	Data Acquisition	39
4.5	Application Methodology	41
4.5.1	Data Processing and Analysis	41
4.5.2	Statistical Analysis and Evaluation	42
5	Experiments & Results	43
5.1	Experimental Setup and Process	43
5.1.1	Data Acquisition and Collection	44
5.1.2	Data Pre-Processing	44
5.1.3	Plane Fitting	45
5.1.4	Evaluation Techniques	45
Distance Between Primitive and Point Cloud	47	
Cloud to Cloud Distance Measurement	47	
Statistical Distribution Analysis	48	
5.2	Results	49
5.2.1	Model 1: Detailed Accuracy Assessment	49
High Density Preset Analysis	50	
Pose 2: High Accuracy Preset Analysis	51	
Pose 2: High Density Preset Analysis	51	
Pose 3: High Accuracy Preset Analysis	52	
Pose 3: High Density Preset Analysis	52	
5.2.2	Summary of Results for Model 1	54
5.2.3	Model 2: Detailed Accuracy Assessment	54
Pose 1: High Accuracy Preset	55	
Pose 1: High Density Preset	56	
Pose 2: High Accuracy Preset	57	
Pose 2: High Density Preset	57	
Pose 3: High Accuracy Preset	59	
Pose 3: High Density Preset	61	
5.2.4	Summary of Results for Model 2	62
5.2.5	Model 3: Detailed Accuracy Assessment	63
Pose 1: High Accuracy Preset	63	

	Pose 1: High Density Preset	63
	Pose 2: High Accuracy Preset	64
	Pose 2: High Density Preset	66
	Pose 3: High Accuracy Preset	68
	Pose 3: High Density Preset	69
5.2.6	Summary of Results for Model 3	69
5.2.7	Model 4	71
	Pose 1: High Accuracy Preset	71
	Pose 1: High Density Preset	72
	Pose 2: Visual Segmentation Challenge	74
	Pose 3: High Accuracy Preset	74
	Pose 3: High Density Preset (Segmentation Challenge)	74
5.2.8	Summary of Results for Model 4	76
5.3	Results Overview	76
5.3.1	Model 1 (30mm, 25mm, 20mm)	77
5.3.2	Model 2 (19mm, 18mm, 17mm, 16mm, 15mm)	77
5.3.3	Model 3 (14mm to 10mm)	77
5.3.4	Model 4 (10mm to 6mm)	77
5.4	Accuracy Assessment	77
5.5	Quantization Effects on C2C Distances	78
5.5.1	General Impact of Quantization on Results	78
6	Conclusion	80
6.1	Summary of the Proposed Solution	80
6.2	Results and Evaluated Outcome	81
6.3	Future Work	81

List of Figures

1.1	Overview of the AM process using a reference object.	2
1.2	SAAPF Framework Process	3
2.1	Quantitative Overview of the Literature Review	5
3.1	Intel RealSense D415 [35]	15
3.2	RealSense Module Composition [36]	16
3.3	Pinhole camera model [37]	17
3.4	Pinhole terminology [38]	18
3.5	Central projection model [39]	19
3.6	Digital camera model adapted from [40]	20
3.7	Stereo system [41]	23
3.8	Epipolar geometry in stereo vision [42]	24
3.9	Epipoles [39]	25
3.10	Epipoles [43]	27
3.11	Distortion [44]	28
3.12	Image rectification in stereo vision [45]	29
3.13	Reconstruction pipeline	30
4.1	Ultimaker 2+ Cura	33
4.2	Reference staircase models	35
4.3	Workspace setup consistent with testing conditions.	36
4.4	RealSense Viewer High Accuracy Preset	37
4.5	Point Cloud Visualization in CC	38
4.6	Visualization of RealSense D415 Depth Quality Specifications [47]	39
4.7	Flowchart illustrating the data acquisition process	41
5.1	Workspace setup consistent with testing conditions	43
5.2	Reference model 3 viewed from the Intel RealSense Viewer	44
5.3	Reference model 1 viewed from CC	45
5.4	Data pre-processing carried out in CC	45
5.5	Plane fitting on the 20mm step	46
5.6	Cloud to Primitive distance	47
5.7	Cloud to Cloud distance	48
5.8	Statistical evaluation of pointcloud data	48
5.9	Gaussian distributions of C2C distances in Model 1, acquired via a high-accuracy preset	50
5.10	Comparative Gaussian distributions of C2C distances for the 30mm-25mm and 25mm-20mm stair steps under the high density preset	50
5.11	Comparative Gaussian distributions of C2C distances for the 30mm-25mm and 25mm-20mm stair steps under the high accuracy preset in Pose 2.	51

5.12	Comparative Gaussian distributions of C2C distances for the 30mm-25mm and 25mm-20mm stair steps under the high density preset in Pose 2. . . .	52
5.13	Comparative Gaussian distributions of C2C distances for the 30mm-25mm and 25mm-20mm stair steps under the high accuracy preset in Pose 3. . .	53
5.14	Comparative Gaussian distributions of C2C distances for the 30mm-25mm and 25mm-20mm stair steps under the high density preset in Pose 3. . . .	53
5.15	Comparative Gaussian distributions of C2C distances for consecutive steps under the high accuracy preset in Pose 1 of Model 2. This comparative view highlights the camera's precision across smaller dimensional intervals.	55
5.16	Comparative Gaussian distributions of C2C distances for consecutive steps under the high density preset in Pose 1 of Model 2. This comprehensive view demonstrates the effects of increased data density on measurement precision across closely spaced intervals.	56
5.17	Comparative Gaussian distributions of C2C distances for consecutive steps under the high accuracy preset in Pose 2 of Model 2. This comprehensive view demonstrates the precision achievable under controlled measurement settings.	58
5.18	Comparative Gaussian distributions of C2C distances for consecutive steps under the high density preset in Pose 2 of Model 2. This analysis aims to evaluate the impact of increased data density on measurement accuracy and precision.	59
5.19	Comparative Gaussian distributions of C2C distances for consecutive steps under the high accuracy preset in Pose 3 of Model 2. This section underscores the camera's reliability and precision across varying poses and setup orientations.	60
5.20	Comparative Gaussian distributions of C2C distances for consecutive steps under the high density preset in Pose 3 of Model 2, indicating the preset's effectiveness in detail capture and its potential impact on measurement noise.	61
5.21	Comparative Gaussian distributions of C2C distances for consecutive steps under the high accuracy preset in Pose 1 of Model 3, highlighting the preset's precision in detail capture and its consistency in measurement across finer scales.	64
5.22	Comparative Gaussian distributions of C2C distances for consecutive steps under the high density preset in Pose 1 of Model 3, highlighting the preset's detailed capture capabilities and its influence on measurement accuracy at smaller dimensions.	65
5.23	Comparative Gaussian distributions of C2C distances for consecutive steps under the high accuracy preset in Pose 2 of Model 3, highlighting the preset's efficacy in detailed measurement and its impact on minimizing noise.	66
5.24	Comparative Gaussian distributions of C2C distances for consecutive steps under the high density preset in Pose 2 of Model 3, highlighting the preset's detailed data capture and its impact on precision and noise.	67
5.25	Comparative Gaussian distributions of C2C distances for consecutive steps under the high accuracy preset in Pose 3 of Model 3, demonstrating the preset's precision and detail capturing capability.	68

5.26	Comparative Gaussian distributions of C2C distances for consecutive steps under the high density preset in Pose 3 of Model 3, showcasing the preset's capability to capture detailed but varied point cloud data.	70
5.27	Comparative Gaussian distributions of C2C distances for consecutive steps under high accuracy preset in Pose 1 of Model 4.	72
5.28	Comparative Gaussian distributions of C2C distances for consecutive steps under high density preset in Pose 1 of Model 4.	73
5.29	Comparative Gaussian distributions of C2C distances for consecutive steps under the high accuracy preset in Pose 3 of Model 4, highlighting the preset's detailed data capture across finer scale measurements.	75
5.30	Quantization effect in C2C distances for Model 1 (Step 30mm to 25mm), Pose 2, High Density preset.	79

List of Tables

2.1	Summary of Research Papers Included in the Literature Review	11
3.1	Specifications of Depth-Sensing Cameras Discussed in the Research	16
4.1	Comparison of Calibration Parameters for Intel RealSense D415: High Accuracy vs. High Density	40

List of Abbreviations

2D	Two-Dimensional
3D	Three-Dimensional
AM	Additive Manufacturing
C.O.V	Coefficient of Variation
C2C	Cloud-to-Cloud
C2M	Cloud-to-Mesh
CCD	Charge-Coupled Device
CMOS	Complementary Metal-Oxide-Semiconductor
IR	Infrared
LIDAR	Light Detection and Ranging
MAE	Mean Absolute Error
M3C2	Multiscale Model to Model Cloud Comparison
MSE	Mean Square Error
MVS	Multi-View Stereo
RGB-D	Red, Green, Blue, and Depth (camera)
RMSE	Root Mean Square Error
RRA	Radius Reconstruction Accuracy
SAAPF	Stereo Accuracy Assessment in Additive Manufacturing via Plane Fitting
SDK	Software Development Kit
SfM	Structure-from-Motion
stl	Standard Tessellation Language
ToF	Time-of-Flight
WCS	World Coordinate System

1 Introduction

Additive Manufacturing (AM), commonly known as three-dimensional (3D) printing, has transformed the manufacturing industry by enabling the production of complex, customized components. Since its commercialization in the 1980s, AM has developed into a versatile production method that fabricates products through a layer-by-layer material deposition process. This approach provides exceptional flexibility in material selection, surface texture, and geometric complexity, making it a powerful tool for both industrial applications and research endeavors [1], [2]. The ability of AM to produce intricate designs unconstrained by traditional manufacturing limitations has driven its widespread adoption across various sectors.

The global AM market was valued at approximately USD 14.5 billion in 2022 and is projected to reach USD 69.3 billion by 2030 [3]. As the technology advances, substantial investments from companies, research institutions, and universities continue to propel growth and innovation in the field. The materials used in AM have expanded beyond polymers to include metals, ceramics, and composites, significantly broadening its application range.

One of the earliest and most prominent uses of AM is in rapid prototyping, where it enables the quick production of complex parts with significantly reduced lead times. This capability not only allows the fabrication of geometries that would be challenging or impossible to achieve through conventional methods but also offers substantial savings in both cost and development time during product design [4].

Traditionally, sourcing parts from overseas suppliers often involves long shipping times and complex logistics, which can delay production by several weeks or even months. In contrast, AM facilitates the in-house production of components within hours, drastically reducing lead times. This shift also significantly lowers the carbon footprint associated with long-distance transportation. By eliminating the need for extensive shipping and packaging, AM supports more sustainable manufacturing practices. Research shows that localized production through AM can achieve considerable reductions in greenhouse gas emissions by minimizing energy-intensive supply chains and reducing material waste [5].

1.1 Challenge

The AM process generally involves six key stages, which can be illustrated through the inspection of an experimental part. The first step entails designing the required component using CAD software, such as Autodesk Fusion 360. Once the design is completed, it is exported as a Standard Tessellation Language (stl) file, a format essential for the slicing process that defines the layer-by-layer material deposition. The 'stl' file is then processed in Cura Slicer using the generic PLA print settings for the Ultimaker 2+ printer, generating a 'gcode' file for printing. This file is transferred to the printer, which is pre-configured during its initial setup. The printing process is initiated by selecting the print option and confirming the desired settings. Depending on the complexity of the design, the print

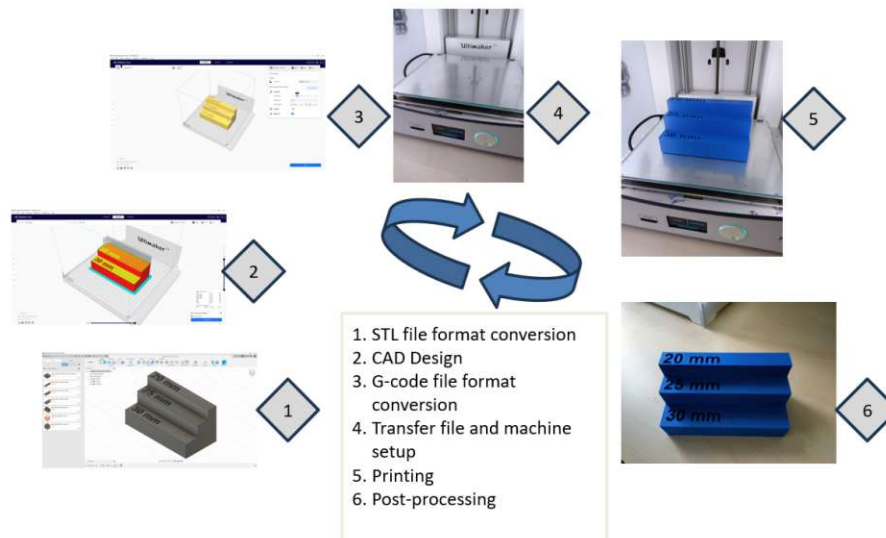


Figure 1.1: Overview of the AM process using a reference object.

time may vary; in this example, the process takes approximately fourteen and a half hours. Upon completion, the part is removed from the print bed and undergoes minimal post-processing, such as removing the first adhesion layer. The final component is then ready for its intended application, as shown in Figure 1.1.

Before a part produced via AM can be used for its intended purpose, it must undergo a rigorous quality assurance process to ensure that it meets the required reliability and performance standards. This quality verification must account for the potential variations introduced at every stage of the AM process, ultimately contributing to a robust and continuously improving quality framework.

After post-processing, the next critical step is to verify the component's suitability for its intended application. This verification is challenging due to the many factors that influence the final product quality, including print bed and nozzle temperatures, material properties, and the process parameters set during slicing. To simplify the study, this research focuses on evaluating post-processed small components (with millimeter-scale dimensions). The objective of this thesis is to assess the feasibility and accuracy of using a specific stereovision camera, the Intel RealSense D415, for the evaluation of such additive-manufactured parts, particularly focusing on low-texture, uniform surfaces at close-range distances of 50 cm.

1.2 Contribution

The primary contribution of this research is the development of a novel assessment method, termed **Stereo Accuracy Assessment in Additive Manufacturing via Plane Fitting (SAAPF)**. This method is specifically designed to evaluate the accuracy of stereovision cameras, such as the Intel RealSense D415, in capturing uniform, low-texture components with millimeter-scale features at a close range of 50 cm. The SAAPF method introduces a structured approach that includes detailed steps to quantify the precision of

the stereo camera. The methodology is accompanied by a comprehensive flowchart for clear visualization and improved comprehension, as illustrated in Figure 1.2.

Stereo Accuracy Assessment in Untextured AM via Plane Fitting (SAAPF)

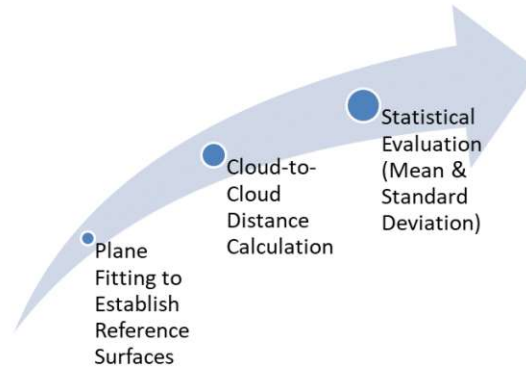


Figure 1.2: SAAPF Framework Process

Key contributions include:

- Introduction and validation of the SAAPF method to assess the minimum resolution and accuracy limits of the Intel RealSense D415.
- A comparative analysis of various metrics relevant to accuracy evaluation in low-texture, small-scale AM products.
- The experiments demonstrated that the Intel RealSense D415 camera is capable of reliably measuring step sizes down to 10mm with minimal deviation under the high accuracy preset. For steps below 10mm, the camera performed well but introduced challenges in segmentation under the high density preset. These findings confirm that the Intel RealSense D415 is suitable for precise metrological applications, particularly in the quality control of additive-manufactured products with low-texture surfaces.

This methodology holds the potential for integration within AM systems, paving the way for a new generation of 3D printers with enhanced in-process quality control capabilities. The research outcomes and data collection methods are further elaborated in Chapter 4.

1.3 Thesis Outline

The thesis is organized as follows: Chapter 2 covers a literature review on AM part evaluation. Chapter 3 investigates the background of the solution further. Chapter 4 describes the experimental setups and proposed solutions. Chapter 5 details the experiments and results in depth. Finally, Chapter 6 concludes all the results.

2 State of the Art

This chapter presents a comprehensive overview of the current state of the art in quality assessment for post-processed parts produced through AM, with a particular focus on 3D scanning camera technologies. The primary aim of this section is to gain a deep understanding of existing research and methodologies related to evaluating such parts. Specifically, this work addresses the following research question: *What are the accuracy limits of stereovision cameras for 3D digital model reconstruction of AM parts with uniform low texture and millimeter-scale features at a close distance of 50 cm?*

This chapter summarizes the methods and quantitative findings from the literature review and identifies key research studies. Additionally, it provides a qualitative evaluation of the reviewed literature. The discussion begins by exploring existing quality assessment methods commonly applied in AM. Following this, the focus shifts to the 3D scanning technologies that have been adopted for this purpose. The evaluation of finished AM parts is then carefully examined. By thoroughly investigating the research question, this thesis seeks to offer a comprehensive understanding of the current landscape of quality and accuracy assessments for AM end products. The selection of an appropriate camera system for further research will be made based on the findings from this literature review.

2.1 Search Criteria

A systematic electronic search was conducted across two major databases, Scopus and IEEE, to capture an overview of the current research landscape on the topic. The search was limited to studies published in English and spanned from the inception of the databases to July 11, 2024.

The search query and strategy are briefly outlined here. Initially, several exploratory searches were performed using a trial-and-error approach to identify the optimal keywords for capturing relevant studies on the accuracy evaluation of stereovision cameras. These keywords were then employed to retrieve pertinent results from the two selected databases. To further refine the search, additional keyword filters within the databases were used to narrow down the results to the most relevant studies. The final search results were exported to an Excel sheet, capturing various details such as author(s), title, year, and abstract.

The first search query was straightforward and included the following keywords: Intel, RealSense, and D415. This query was applied to both databases, yielding 39 results in Scopus and 10 in IEEE.

The second search query included the following keywords: (3D AND reconstruction) AND (realsense OR stereo OR rgbd) AND (comparison OR accuracy) AND (evaluation OR assessment). This search produced 439 results in Scopus and 182 in IEEE. To further narrow the results, keyword-based filtering was applied. The IEEE search was refined using the keyword “stereo camera,” reducing the entries to 34 results. Similarly, the

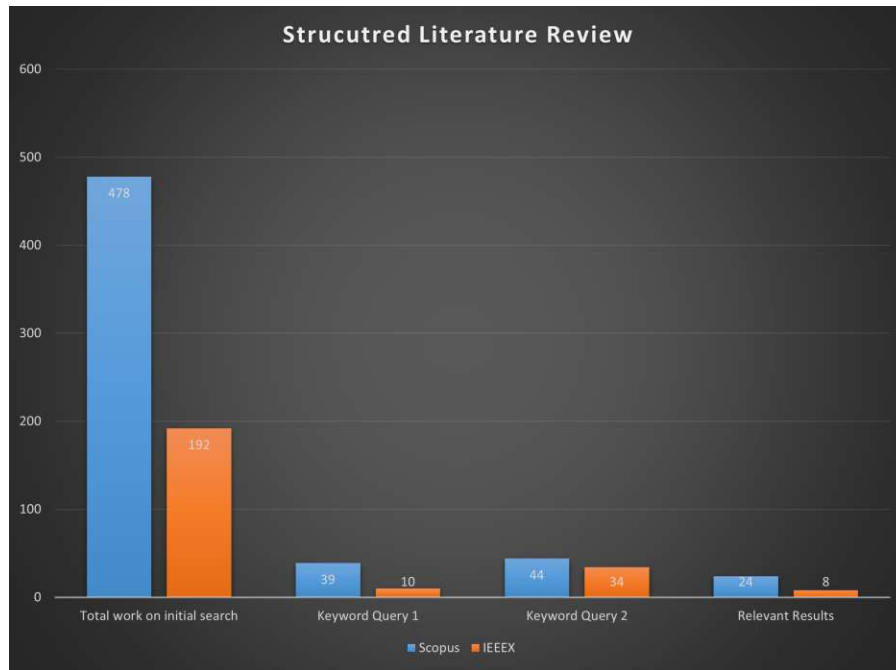


Figure 2.1: Quantitative Overview of the Literature Review

Scopus search was refined using the keyword “accuracy assessment,” bringing the entries down to 44 results.

The combined initial search yielded a total of 670 studies. After applying the keyword filters, 127 studies remained. A preliminary sanity check was conducted to verify the available metadata, such as author names, publication dates, and abstracts. At the first level of filtering, studies were screened for relevance based on their titles, with non-relevant topics being excluded. The remaining studies were then reviewed by carefully reading their abstracts to gain a better understanding of the literature, further eliminating irrelevant work. A quantitative overview of the results is presented in Figure 2.1.

2.2 Literature

The selected studies encompass a broad spectrum of research focusing on evaluation criteria, stereo vision-based depth-sensing technologies, time-of-flight (ToF) and LiDAR-based systems, and comparative or cross-technology assessments. These works provide critical insights into the performance, strengths, and limitations of various stereovision systems, offering guidance for selecting an appropriate camera for further research into accuracy assessment in AM processes. The literature is now categorized into four key sections: evaluation criteria, stereo vision-based depth-sensing technologies, ToF and LiDAR-based technologies, and comparative or cross-technology studies. This organization allows for a comprehensive yet structured analysis of factors impacting the precision and applicability of these technologies in AM applications. A detailed summary of the reviewed research papers, categorized by their technological focus and evaluation criteria, is presented in Table 2.1.

2.2.1 Evaluation Criteria

This subsection focuses on studies that discuss various evaluation criteria for assessing the performance and accuracy of stereovision camera systems. Key factors such as resolution, depth accuracy, robustness in low-texture environments, and calibration methodologies are explored. Understanding these criteria is essential for determining the suitability of a camera system for specific applications in additive manufacturing, particularly when dealing with millimeter-scale components and uniform low-texture surfaces.

The study by D'Angelo, Pablo, and Christian Wöhler [6] introduces a technique to integrate dense yet noisy depth data derived from intensity and polarization images with sparse and precise depth data from stereo vision to enhance the accuracy of the resulting 3D reconstruction. Although the study mentions the use of two CCD cameras for stereo vision, the specific camera model is not identified. The application of this experiment spans industrial quality inspection of raw forged iron surfaces and space-based planetary exploration. However, the paper lacks an explicit method to assess the accuracy of the stereo vision data.

The research conducted by Borgmann, Thilo, Michael Tok, and Thomas Sikora [7] emphasizes improving robustness in dynamic scene capture by introducing two novel approaches for more precise 3D reconstruction. The evaluation section introduces a noteworthy approach for assessing differences between reconstructed surfaces by comparing depth maps generated by projecting the obtained 3D model into the image plane of one of the cameras and computing the mean square error (MSE) in the depth domain. The stereo setup in this study is based on the method outlined by Ide, Kai, and Thomas Sikora [8].

Mathavan, Senthana, Khurram Kamal, and Mujib Rahman [9] review various 3D imaging technologies used for accurate pavement inspection. Although initially included in the literature review based on an interesting abstract, the study highlights the necessity for precise estimates to capture small road defects. Several relevant works are reviewed, including studies by [10], [11], [12], [13], [14], [15], and [16]. Among these, [12] reports a depth accuracy of 5mm. Despite the inclusion of relevant studies, the article lacks a methodology for accuracy assessment.

The work by Stumpf, André, et al. [17] provides an excellent review of multi-view photogrammetry applications for monitoring landslide deformation. The study quantitatively evaluates the accuracy of dense point clouds generated by several Structure-from-Motion (SfM) and Multi-View Stereo (MVS) pipelines. The paper is particularly noteworthy for its exploration of point cloud accuracy assessment, detailing common methods such as cloud-to-mesh (C2M) computation [18] and Multiscale Model to Model Cloud Comparison (M3C2) [19]. The paper notes that while C2M offers highly accurate distance measurements, it poses challenges when point clouds do not overlap, whereas M3C2 avoids the need for explicit surface interpolation. The experiments utilized CloudCompare to manually remove non-overlapping parts of point clouds before computing C2M. Delaunay Triangulation with a least-squares fit was used to interpolate the reference for C2M. The evaluation metrics included the Mean Absolute Error (MAE), Root Mean Squared Error (RMSE), and Mean Distance (MD) between clouds.

In the study by Slocum, Richard K., and Christopher E. Parrish [20], one of the common challenges in determining the spatial accuracy of a point cloud derived from SfM-MVS algorithms is highlighted. Typically, this involves a comparison against independent

reference data of higher accuracy, but acquiring such data can be cost-prohibitive and time-consuming. The research proposes a workflow to simulate real-world environments using computer-generated imagery. An experiment assesses the accuracy of an SfM-derived point cloud from the artificial imagery. Dense point clouds are processed using CloudCompare and compared to the ground truth mesh using the "point to plane" tool, which calculates the signed distance from every point in the cloud to the nearest surface on the mesh.

Fan, Rui, Xiao Ai, and Naim Dahnoun [21] propose a dense subpixel disparity estimation algorithm that offers both high computational efficiency and robustness to achieve millimeter-level accuracy needed for road condition assessments. The accuracy of the 3D reconstruction is evaluated by fitting a surface equation to the four corners of the selected area of interest. Random points are then chosen on the surface of the model to estimate the distance between those points and the road surface. The paper reports a maximum absolute error of approximately 3mm for the 3D reconstruction.

Berveglieri, Adilson, and Antonio MG Tommaselli [22] present a technique for reconstructing cylindrical surfaces using stereo images and an extension of least squares matching. The approach involves stereo image acquisition along the length of cylindrical objects, followed by calculating the cylinder diameter using circle fitting via the least squares method on selected XY coordinates. The accuracy is assessed by comparing the estimated diameter with measurements obtained using a digital caliper, achieving a precision of 0.1 mm. Standard deviation and diameter difference are the key metrics used in the assessment, making this methodology suitable for evaluating the accuracy of 3D reconstructions of cylindrical objects.

The study by Moghari, M. Dashtbani, et al. [23] evaluates the Intel RealSense D415 stereo depth camera's performance in enhancing CT scan precision by tracking head movements. The accuracy is assessed using the root mean square error (RMSE) between the D415 and ground truth pose measurements (UR3 and OptiTrack).

Al Muallim, Mohammad Tarek, et al. [24] develop a dimension measurement system for logistics applications using a depth camera. The Intel RealSense D415 is used to obtain point cloud data, with metrics such as average, standard deviation, and maximum absolute error being calculated to evaluate system accuracy.

In a subsequent study, Dawda, Arpita, and Minh Nguyen [25] present an automated defect detection technique utilizing laser line projection and stereovision concepts. Building upon earlier work [26], the study compares the 3D profile of a defective product with a non-defective product to assess accuracy.

Shatnawi, Nawras [27] utilizes statistical measures, including mean, standard deviation, and coefficient of variation (COV), to assess the accuracy of a 3D model generated using a laser scanner, cellular phone, and 360-degree camera for a historical site.

2.2.2 Summary of Evaluation Metrics

The literature review on evaluation criteria has highlighted several metrics used to assess the performance and accuracy, summarizing these metrics:

- **Mean Square Error (MSE):** Utilized for assessing differences between reconstructed surfaces by comparing depth maps generated from 3D models.

- **Depth Accuracy:** Specific metrics such as a reported depth accuracy of 5mm in studies focused on pavement inspection technologies.
- **Cloud-to-Mesh (C2M) Computation:** Employed for highly accurate distance measurements in point cloud assessments, requiring significant point cloud overlap.
- **Multiscale Model to Model Cloud Comparison (M3C2):** Used for comparing point clouds without the need for explicit surface interpolation.
- **Mean Absolute Error (MAE), Root Mean Squared Error (RMSE), and Mean Distance (MD):** Commonly used to evaluate the spatial accuracy of point clouds against high accuracy reference data or simulations.
- **Maximum Absolute Error:** Assessed in subpixel disparity estimation for road condition assessments, aiming for millimeter-level accuracy.
- **Standard Deviation and Diameter Difference:** Applied to evaluate the accuracy of diameter measurements in cylindrical object reconstructions using stereo images.
- **Average, Standard Deviation, and Maximum Absolute Error:** Calculated to assess the accuracy of depth cameras in logistics applications for dimension measurement.
- **Coefficient of Variation (COV):** Used alongside mean and standard deviation to evaluate the statistical accuracy of 3D models in the documentation of historical sites.

These metrics provide a comprehensive toolkit for evaluating the suitability and accuracy of stereovision systems, especially in applications involving precise dimensional requirements and low-texture surfaces.

2.2.3 Stereo Vision-Based Depth-Sensing Technologies

This section covers research related to active stereo vision cameras, structured light systems integrated with stereo setups, and hybrid approaches such as laser triangulation combined with stereo vision. These technologies are particularly relevant for applications where precise depth sensing is needed in controlled environments or low-texture scenarios.

- **Carfagni et al. (2019) [28]:** This study provides a comprehensive metrological evaluation of the Intel RealSense D415, focusing on close-range applications (100–1000 mm) following standards like German VDI/VDE 2634 Part 2. The experiments assess the camera's performance in terms of probing errors, sphere spacing errors, and flatness errors. The study highlights the D415's adjustable settings, such as laser power and disparity shift, which enhance its adaptability to different environments. The study compares the D415's performance with other models like the Intel SR300, Kinect v2, and PrimeSense Carmine, concluding that the D415 offers the best combination of accuracy and flexibility in close-range applications.
- **Servi et al. (2021) [29]:** The paper evaluates the metrological performance of three Intel RealSense cameras: D415, D455, and L515. The study uses the ISO

10360-13 standard for assessing probing errors, systematic depth errors, and 3D object reconstruction. The research focuses on close-range applications (100–1500 mm), highlighting that the D415 performs well at very close distances, while the L515 excels in reducing systematic depth errors at longer ranges. The experiments involve systematic tests that highlight each camera's strengths, providing a well-rounded comparison.

- **Lourenço and Araujo (2021) [30]:** This study compares the performance of the Intel RealSense D415, SR305, and L515 across various distances in indoor environments. The research evaluates point-to-plane error measurements, consistency analysis, and outlier detection. The D415 is noted for its consistent performance at mid-range distances, balancing depth accuracy and stability. The experiments involve point-to-plane distance measurements with different outlier rejection thresholds (± 10 cm and ± 35 cm) to assess accuracy.
- **Curto and Araujo (2022) [31]:** This paper focuses on the depth estimation capabilities of the Intel RealSense D415, SR305, and L515 when dealing with transparent and translucent materials, which are particularly challenging for depth sensors. The experiments evaluate depth accuracy and repeatability under various lighting conditions, with the D415 consistently outperforming the other models in terms of statistical variability and reliability. The study uses scenarios that simulate real-world challenges, such as scenes containing glass objects or translucent plastics.
- **Dawda et al. (2019) [26]:** The research introduces a hybrid approach that combines laser line triangulation with stereo imaging to enhance depth accuracy, particularly for reflective and low-texture surfaces. The method involves projecting a narrow light band onto the surface and capturing the distorted line using two cameras. The study details the algorithm used for stereo matching of the laser profiles and highlights the significant improvements in depth estimation achieved by integrating this hybrid system.

2.2.4 Time-of-Flight (ToF) and LiDAR-Based Depth-Sensing Technologies

This section discusses studies focused on ToF and LiDAR-based technologies, which are known for their accuracy in both short-range and long-range applications. These technologies are typically used in environments requiring fast depth measurements, such as robotics, metrology, and large-scale 3D mapping.

- **da Silva Neto et al. (2020) [32]:** The study compares the performance of ten RGB-D cameras, including time-of-flight models such as the Kinect V2 and Orbbec Astra. The evaluation uses a robotic arm to capture data across three distinct paths, with metrics such as trajectory error, point cloud density, and reconstruction completeness being analyzed. The research finds that time-of-flight technology consistently delivers stable depth measurements, though with some limitations in low-texture or reflective environments. The experiments involve capturing data in controlled indoor environments that include both highly textured and poorly textured regions.

- **Parr, Legg, and Alam (2022) [33]**: This study compares the performance of several depth cameras, including Kinect V1, Kinect V2, Azure Kinect, Intel RealSense D415, and L515, with a focus on outdoor applications. The research highlights the impact of sunlight on depth measurements, with time-of-flight cameras performing better in outdoor conditions. The experiments involve both indoor and outdoor environments, where the cameras are tested under different lighting scenarios. The results indicate that while ToF cameras are less affected by sunlight, they exhibit shape distortions that influence depth accuracy.
- **Servi et al. (2021) [29]**: In this paper, the Intel RealSense L515, a LiDAR-based camera, is evaluated alongside the D415 and D455. The research focuses on probing errors, systematic depth errors, and 3D reconstruction accuracy. The L515 demonstrates excellent depth accuracy at longer ranges but struggles with consistent measurements at very close distances. The experiments involve metrological testing in controlled environments, highlighting the trade-offs between accuracy and range when using LiDAR for depth sensing.
- **Lourenço and Araujo (2021) [30]**: The study includes a detailed comparison of the L515's depth-sensing capabilities, particularly in terms of point cloud precision and RMSE. The research emphasizes the camera's performance under indoor conditions, where the L515 shows the lowest root mean square error (RMSE) in longer-range tests. However, the study also notes challenges with biases when dealing with reflective surfaces.
- **Curto and Araujo (2022) [31]**: The paper investigates the L515's performance in scenes containing transparent and translucent objects. The study assesses depth estimation errors, consistency checks, and failure rates, finding that while the L515 performs well in less transparent conditions, it faces difficulties with highly transparent materials. The experiments simulate real-world conditions where transparent objects are scanned, showing the limitations of LiDAR technology in such scenarios.

2.2.5 Cross-Technology Studies

This section includes studies that compare multiple depth-sensing technologies across various scenarios, providing a broad overview of the performance differences between stereo vision, structured light, ToF, and LiDAR technologies.

- **Adamides et al. (2023) [34]**: The study compares three depth-sensing technologies—stereoscopic (Intel RealSense D435i), time-of-flight (Azure Kinect DK), and LiDAR (Ouster OS0-32)—focusing on their performance in dynamic environments. The research is particularly relevant for robotic applications, where real-time depth sensing is essential. The experiments evaluate metrics such as radius reconstruction accuracy (RRA), frame rates, and edge detection in both static and dynamic conditions. The study finds that while the LiDAR-based system excels in high-resolution static measurements, it struggles with latency and noise in dynamic scenarios, making the stereo and ToF systems more suitable for applications requiring real-time responses.

- **da Silva Neto et al. (2020) [32]**: This comprehensive study assesses ten RGB-D cameras, analyzing depth accuracy across structured light, stereo vision, and time-of-flight technologies. The experiments involve capturing data in controlled indoor environments using a robotic arm and evaluating metrics such as point cloud completeness and trajectory error. The study concludes that while stereo vision cameras perform well in mid-range applications, ToF cameras are better suited for dynamic environments due to their fast response times.
- **Parr, Legg, and Alam (2022) [33]**: This paper evaluates the performance of depth cameras in agricultural applications, where environmental factors such as sunlight and varying textures play a significant role. The research compares Kinect V1, Kinect V2, Azure Kinect, Intel RealSense D415, and L515 under both indoor and outdoor conditions. The experiments focus on factors like shape distortions and depth accuracy in different lighting scenarios. The study highlights that while ToF cameras are more robust outdoors, stereo vision systems like the D415 provide better accuracy in controlled indoor settings.
- **Dawda and Nguyen (2020) [25]**: Building on earlier research, this study proposes an automated defect detection technique that utilizes laser line projection and stereovision concepts. The research compares the 3D profiles of defective and non-defective products, focusing on the accuracy of defect identification. The experiments involve simulating common defects in industrial products and assessing the system's ability to detect them using depth maps generated from stereo vision and laser triangulation.
- **Al Muallim et al. (2019) [24]**: The study develops a logistics dimension measurement system using the Intel RealSense D415, comparing its performance with other depth cameras in terms of accuracy, standard deviation, and maximum absolute error. The experiments involve capturing point cloud data from objects of varying sizes and shapes and analyzing the accuracy of the measurements.

Table 2.1: Summary of Research Papers Included in the Literature Review

Sr. No.	Author	Year	Evaluation Criteria	Stereo Vision-Based Technologies	ToF and LiDAR-Based Technologies	Cross-Technology	Part of Literature Review
1	D'Angelo, P.; Wöhler, C.	2008	✓	✗	✗	✗	Y
2	Borgmann, T.; Tok, M.; Sikora, T.	2015	✓	✗	✗	✗	Y

Continued on next page

Table 2.1: (continued)

Sr. No.	Author	Year	Evaluation Criteria	Stereo Vision-Based Technologies	ToF and LiDAR-Based Technologies	Cross-Technology	Part of Literature Review
3	Mathavan, S.; Kamal, K.; Rahman, M.	2015	✓	✗	✗	✗	Y
4	Hou, Z.; Wang, K. C. P.; Gong, W.	2007	✗	✗	✗	✗	N
5	Stumpf, A.; Malet, J.-P.; Allemand, P.	2015	✓	✗	✗	✗	Y
6	Slocum, R. K.; Parrish, C. E.	2017	✓	✗	✗	✗	Y
7	Fan, R.; Ai, X.; Dahnoun, N.	2018	✓	✗	✗	✗	Y
8	Berveglieri, A.; Tommaselli, A. M. G.	2018	✓	✗	✗	✗	Y
9	Hui, F.; Zhu, J.; Hu, P.; et al.	2018	✓	✗	✗	✗	Y
10	Giancola, S.; Valenti, M.; Sala, R.	2018	✗	✓	✗	✗	Y
11	Dawda, A.; Nguyen, M.; Klette, R.	2019	✓	✓	✗	✗	Y
12	Moghari, M. D.; Noonan, P.; Henry, D. L.; et al.	2019	✓	✗	✗	✗	Y
13	Al Muallim, M. T.; Küçük, H.; et al.	2019	✗	✓	✗	✗	Y

Continued on next page

Table 2.1: (continued)

Sr. No.	Author	Year	Evaluation Criteria	Stereo Vision-Based Technologies	ToF and LiDAR-Based Technologies	Cross-Technology	Part of Literature Review
14	Carfagni, M.; Furferi, R.; Governi, L.; et al.	2019	✓	✓	✗	✗	Y
15	Dawda, A.; Nguyen, M.	2020	✓	✓	✗	✗	Y
16	da Silva Neto, J. G.; Lima Silva, P. J.; et al.	2020	✗	✗	✓	✗	Y
17	Shatnawi, N.	2020	✓	✗	✗	✗	Y
18	De Gregorio, D.; Poggi, M.; et al.	2021	✗	✗	✗	✗	Y
19	Battistoni, G.; Cassi, D.; et al.	2021	✗	✗	✗	✗	Y
20	Servi, M.; Mussi, E.; et al.	2021	✓	✓	✗	✓	Y
21	Lourenço, F.; Araujo, H.	2021	✓	✓	✗	✓	Y
22	Morrison, M. J.; Gahagan, A. C.; et al.	2021	✗	✗	✗	✗	Y
23	Parr, B.; Legg, M.; Alam, F.	2022	✓	✗	✓	✗	Y
24	Jin, X.; Tang, L.; Li, R.; et al.	2022	✗	✗	✗	✗	Y
25	Ye, Q.; Bai, Y.; Chen, L.; et al.	2022	✗	✗	✗	✗	Y
26	Curto, E.; Araujo, H.	2022	✓	✓	✗	✓	Y

Continued on next page

Table 2.1: (continued)

Sr. No.	Author	Year	Evaluation Criteria	Stereo Vision-Based Technologies	ToF and LiDAR-Based Technologies	Cross-Technology	Part of Literature Review
27	Bairagi, A.; Frear, C.; et al.	2022	✗	✗	✗	✗	Y
28	Adamides, O. A.; Avery, A.; Subramanian, K.; et al.	2023	✗	✗	✓	✗	Y
29	Burger, L.; Sharan, L.; et al.	2023	✗	✗	✗	✗	Y
30	Servi, M.; Mussi, E.; et al.	2024	✓	✗	✗	✗	Y

3 Background

Based on the insights from the literature review, the Intel RealSense D415 (shown in the Fig. 3.1) emerges as a highly suitable candidate for AM applications involving low-texture surfaces. Several key factors support this choice:

- **Adaptability in Low-Texture Environments:** The D415's active stereo vision system, which includes an infrared projector, enhances depth capture accuracy in environments with minimal texture, a common scenario in AM products [28], [29], [31].
- **Close-Range Precision:** Research by Carfagni et al. [28], Servi et al. [29], and Curto and Araujo [31] demonstrates the D415's superior performance in close-range applications (150–1000 mm), which is crucial for the precise 3D reconstruction needed in AM.
- **Configurability:** The D415 provides flexible settings, such as adjustable laser power and disparity shift, enabling optimized performance across various AM scenarios [28], [29].
- **Proven Performance:** Several studies highlight the D415's balanced combination of accuracy, reliability, and cost-effectiveness, making it ideal for consistent and repeatable measurements in industrial AM applications [28], [29], [31].



Figure 3.1: Intel RealSense D415 [35]

3.1 Camera Operation and Working Principle

To fully understand the factors influencing accuracy in AM applications, it is essential to delve into the working principles of the selected Intel RealSense D415 camera. The D415

Table 3.1: Specifications of Depth-Sensing Cameras Discussed in the Research

Camera Model	Technology Type	Resolution (Depth)	Depth Range
Intel RealSense D415	Active Stereo Vision	1280 × 720	0.3 – 10 m
Intel RealSense D435i	Active Stereo Vision	1280 × 720	0.2 – 10 m
Intel RealSense D455	Active Stereo Vision	1280 × 720	0.4 – 6 m
Intel RealSense L515	LiDAR	1024 × 768	0.25 – 9 m
Microsoft Kinect v2	Time-of-Flight	512 × 424	0.5 – 4.5 m
Azure Kinect DK	Time-of-Flight	1024 × 1024	0.3 – 5.5 m
Orbbec Astra S	Structured Light	640 × 480	0.4 – 8 m
Intel RealSense SR305	Structured Light	640 × 480	0.2 – 2 m
Kinect V1	Structured Light	640 × 480	0.8 – 4 m

utilizes a stereo vision setup that includes a left imager, right imager, and an optional infrared projector as depicted in Figure 3.1. The infrared projector projects a non-visible static IR pattern, which enhances depth accuracy in low-texture environments.

The stereo vision system captures the scene using the left and right imagers, with the captured data sent to the depth imaging processor. The processor correlates points between the left and right images, determining depth values for each pixel by calculating the disparity between corresponding points. These depth values are processed to generate a depth frame, and subsequent frames create a continuous depth video stream.

Table 2-2. Depth Camera Product SKU Descriptions

Component	Subcomponent	Intel® RealSense™ Depth Camera D415	Intel® RealSense™ Depth Camera D435	Intel® RealSense™ Depth Camera D435i
Intel® RealSense™ Vision Processor D4	-	✓	✓	✓
Intel® RealSense™ Depth Module	Standard Stereo Imagers	✓	✗	✗
	Wide Stereo Imagers	✗	✓	✓
	Standard Infrared Projector	✓	✗	✗
	Wide Infrared Projector	✗	✓	✓
	RGB color sensor	✓	✓	✓
Inertial Measurement Unit (IMU)		✗	✗	✓

Figure 3.2: RealSense Module Composition [36]

Understanding the operation of the D415 camera, including the role of individual components like the IR projector and stereo imagers illustrated in the Fig. 3.2, is critical to evaluating its performance in the context of AM accuracy assessments. In the next section, the discussion will focus on the key theoretical concepts and parameters relevant to 3D scanning and accuracy evaluation.

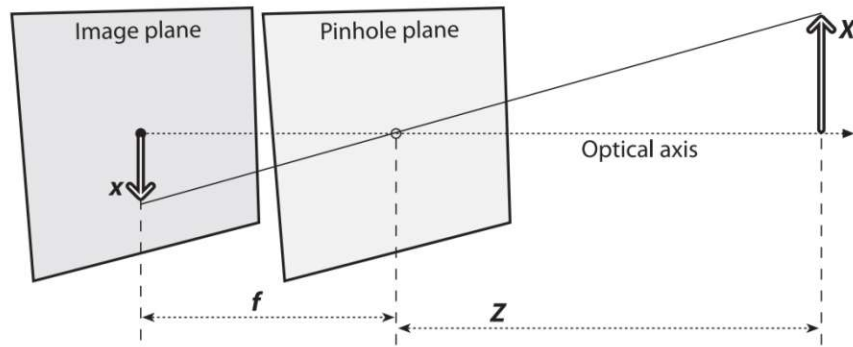


Figure 3.3: Pinhole camera model [37]

3.2 Camera Models

Camera models are fundamental to understanding how three-dimensional scenes are projected onto two-dimensional image planes. These models serve as the mathematical foundation for various computer vision tasks, including the stereo vision systems central to this research. While the pinhole camera model is often used for its simplicity and effectiveness, several other models exist to account for various optical phenomena and to improve accuracy in specific applications. Let's take a closer look into image formation.

3.2.1 Pinhole camera model

The pinhole camera model is a mathematical abstraction, commonly used in computer vision, to describe the geometric relationship between 3D points in a scene and their 2D projections onto an image plane. It consists of two planes which are perfectly parallel to each other in the model, namely, the image and pinhole plane. The distance between them is the focal length f . The pinhole plane is almost optical opaque except for a infinitesimal small hole (aperture) big enough for the intersecting light ray to pass. The light rays intersect a photosensitive film located at the back of the box, generating an inverted image of the scene on the image plane. The optical axis is defined as the axis which normal to both planes and passes through the center of the pinhole. Fig 3.3 illustrates a pinhole camera, where ' f ' is the focal length, ' Z ' is the distance from the camera to the object, ' X ' is the length of the object, and ' x ' is the object's image on the imaging plane. In the figure, similar triangles are observed, using the similar triangles equation $-x/f = X/Z$, or

$$-x = f \frac{X}{Z} \quad (3.1)$$

As can be seen from the Fig 3.3, the projection is inverted as compared to original position. Moreover, the aperture of the pinhole does not provide bright enough images. In order to solve the inconveniences, the simple pinhole camera model needs to be adjusted. The most common solution in practice is to use a lens instead of a pinhole. Lenses allow for a larger aperture while still focusing light onto the image plane.

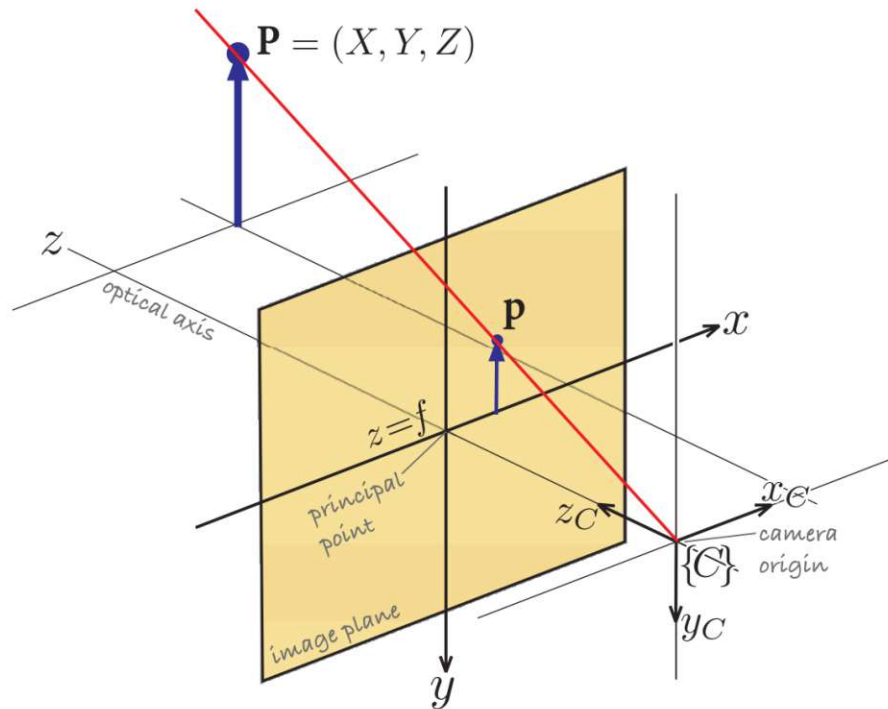


Figure 3.4: Pinhole terminology [38]

3.2.2 Central projection model

Figures 3.4, 3.5 illustrates the central projection model and defines some terminology. The aperture is called the optical center (Oc), and it defines the origin of the camera coordinate frame. The virtual image is created on the image plane, and is located at a distance f in front of the camera's origin. The line passing through Oc perpendicularly to the image plane defines the optical axis Z_c . The point where the optical axis strikes the image plane is known as the principal point. The distance between the principal point and the optical center (i.e., the distance between the image plane and the pinhole) is known as the focal length.

The main difference is that the object now appears rightside up. The point in the pinhole is reinterpreted as the center of projection. Every ray leaves a point on the distant object and heads for the center of projection. On this new image plane, the image of the distant object is exactly the same size as it was on the image plane in Figure 3.3. The image is generated by intersecting these rays with the image plane, which happens to be exactly a distance f from the center of projection. This makes the similar triangles relationship to $x/f = X/Z$, removal of the negative sign is because the object image is no longer inverted.

Digital cameras use an electronic image sensor—typically a Charge-Coupled Device (CCD) or Complementary Metal-Oxide-Semiconductor (CMOS) sensor—that functions as the image plane. This sensor is composed of a grid of light-sensitive elements known as pixels, each representing a specific point on the virtual image plane. When light rays hit the sensor, each pixel converts the light into an electrical signal. This signal is then

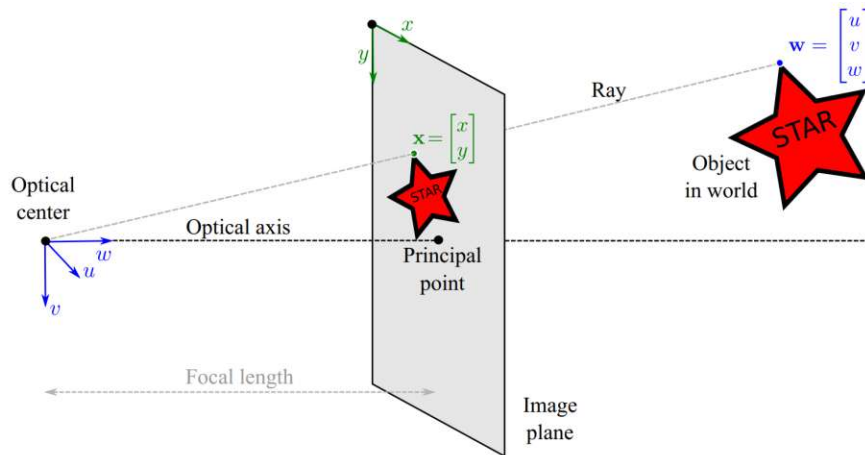


Figure 3.5: Central projection model [39]

digitized into numerical values that encode the intensity and color at that point in the image. The sensor's physical size and pixel count determine the camera's resolution and field of view.

3.2.3 Camera Calibration Parameters

In practice, real cameras deviate from the ideal pinhole model due to various factors. To account for these deviations and accurately describe the camera's imaging characteristics, several additional parameters need to be accounted for:

Principal Point Offset

Digital images are usually measured in pixels, with the origin of the image frame O_i located at the upper left corner of the image. The principal point, ideally located at the center of the image sensor, may be slightly offset due to manufacturing imperfections. This offset is described by two parameters (c_x, c_y) ¹, representing the displacement of the principal point from the image center as can be seen in the Fig 3.6.

Effective Focal Length

The focal length f is the distance between the lens's optical center and the image plane. In digital image processing, the concept of effective focal length in pixels, denoted as (f_x, f_y) , is utilized. This effective focal length represents the distance from the pinhole to the image plane measured in pixels. It accounts for potential differences in magnification along the x and y axes. The relationship between the physical focal length and the effective focal length in pixels is given by:

$$f_x = f/s_x, \quad f_y = f/s_y \quad (3.2)$$

where s_x and s_y correspond to the pixel size in corresponding direction. These effective pixel sizes relate to the physical sensor dimensions and the number of pixels:

¹ c_x and c_y are both measured in pixels

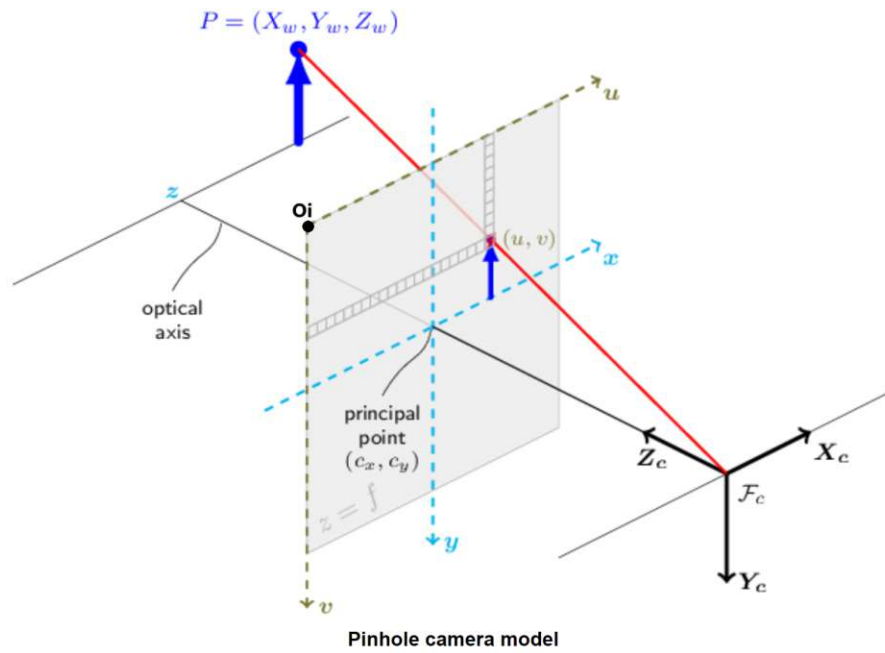


Figure 3.6: Digital camera model adapted from [40]

$$s_x = \frac{\text{sensor width}}{\text{number of pixels in x direction}}, \quad s_y = \frac{\text{sensor height}}{\text{number of pixels in y direction}} \quad (3.3)$$

The effective focal length in pixels is crucial for translating the camera's optical properties into digital image coordinates, maintaining consistency with the principles outlined by the thin lens equation.

Skew

Skew parameter γ accounts for distortions between the x and y axes of the pixel array. In most modern cameras, this value is very close to zero, but it's included for completeness:

$$\gamma = f_x \tan \alpha \quad (3.4)$$

where γ is the angle between the x and y pixel axes.

Intrinsic Parameters

The intrinsic parameters describe the internal optical characteristics of the camera. They are typically represented in a 3x3 matrix K :

$$K = \begin{bmatrix} f_x & \gamma & c_x \\ 0 & f_y & c_y \\ 0 & 0 & 1 \end{bmatrix} \quad (3.5)$$

The intrinsic parameter matrix converts points from the camera coordinate system to the pixel coordinate system. It inherently depends on camera properties such as focal length, pixel dimensions, resolution, principal point offset, and skew etc.

Extrinsic Parameters

The intrinsic parameters describe the camera's internal characteristics, while the extrinsic parameters define the camera's position and orientation in the world coordinate system. This is to account for the fact that the camera is not always centered at the origin of the world coordinate system. The extrinsic parameters are:

- A 3x3 rotation matrix R
- A 3x1 translation vector t

Together, these form a 3x4 matrix $[R|t]$ that transforms 3D world coordinates to camera coordinates:

$$[R|t] = \begin{bmatrix} r_{11} & r_{12} & r_{13} & t_x \\ r_{21} & r_{22} & r_{23} & t_y \\ r_{31} & r_{32} & r_{33} & t_z \end{bmatrix} \quad (3.6)$$

The extrinsic parameter matrix converts points from world coordinate system to camera coordinate system depending on the position and orientation of the camera. The complete projection of a 3D point X in world coordinates to a 2D point x in image coordinates can be expressed as:

$$x = K[R|t]X \quad (3.7)$$

3.2.4 Complete Camera Model

The complete camera model describes the projection of a 3D point in the world onto a 2D image plane. This can be better understood by combining the intrinsic and extrinsic parameters.

Let $X_w = [X_w, Y_w, Z_w, 1]^T$ be a homogeneous 3D point in world coordinates. The projection of this point onto the image plane can be described by the following equation:

$$\begin{bmatrix} u \\ v \\ 1 \end{bmatrix} = K[R|t] \begin{bmatrix} X_w \\ Y_w \\ Z_w \\ 1 \end{bmatrix} \quad (3.8)$$

Where:

- $[u, v]^T$ are the pixel coordinates in the image
- K is the intrinsic parameter matrix
- $[R|t]$ is the extrinsic parameter matrix

The equation 3.8 can be written as:

$$\begin{bmatrix} u \\ v \\ 1 \end{bmatrix} = \begin{bmatrix} f_x & s & c_x \\ 0 & f_y & c_y \\ 0 & 0 & 1 \end{bmatrix} \begin{bmatrix} r_{11} & r_{12} & r_{13} & t_x \\ r_{21} & r_{22} & r_{23} & t_y \\ r_{31} & r_{32} & r_{33} & t_z \end{bmatrix} \begin{bmatrix} X_w \\ Y_w \\ Z_w \\ 1 \end{bmatrix} \quad (3.9)$$

This encapsulates several transformations:

1. The extrinsic parameters (rotation and translation) $[R|t]$ transform the 3D point from world coordinates to camera coordinates.
2. The intrinsic parameters K then project the 3D point from camera coordinates to pixel (2D) coordinates .

This forms the basis of the working principle of a camera. Understanding these foundational principles is crucial, as they are applied directly in stereo vision systems, which rely on capturing and interpreting images from different viewpoints to recreate depth.

3.3 Stereo Vision

Stereo vision is a technique of estimating the three-dimensional information from two images taken from different viewpoints. This process mirrors the principles of human binocular vision. There are two main approaches to stereo vision:

Passive stereo vision

This traditional method relies solely on ambient lighting and natural features in the scene to perform stereo matching.

Active stereo vision

This technique enhances the process by employing an artificial light source, such as a laser or structured light pattern.

3.3.1 Stereo vision fundamentals

A stereo system is used primarily to record an image pair simultaneously. This requires two camera with identical parameters to capture an image pair in sync. Ideally, both cameras should be precisely aligned so that their image planes are coplanar. In this case, the optical center of the two camera are positioned in such way that they lie on each other's x-axis perpendicular to the baseline. In practice, this ideal alignment is rarely perfect, but these misalignments can be corrected during the camera calibration process.

Consider a calibrated stereo system, now, the primary focus is to estimate depth. In a calibrated stereo system configuration, let the optical center of the cameras be denoted as \mathbf{O}_l and \mathbf{O}_r , respectively. The vector \mathbf{b} represents the displacement between the two cameras. The principal points for each camera, \mathbf{C}_l and \mathbf{C}_r , are the locations where the principal rays intersect the image planes. These points are typically near the center of

the image. In an ideal system, the pixel coordinates of corresponding points in the left and right images would be identical, meaning that the principal points \mathbf{C}_l and \mathbf{C}_r should coincide. The cameras are assumed to have identical focal lengths f .

Consider a 3D point \mathbf{P} in the physical world that is visible in both cameras. This point is projected onto the image planes of both cameras with horizontal pixel coordinates u_l and u_r , respectively. For an infinite distance Z , the two coordinates u_l and u_r will be identical. With these coordinates disparity \mathbf{d} is defined as:

$$d = u_l - u_r \quad (3.10)$$

From the Fig. 3.7, similar triangles are observed which leads to:

$$\frac{b - (u_l - u_r)}{Z - f} = \frac{b}{Z} \implies Z = \frac{bf}{u_l - u_r} \quad (3.11)$$

Where Disparity \mathbf{d} is the difference in image location of the projection of a 3D point in two image planes. Baseline \mathbf{b} is the distance between the two cameras. Usually, this Z depth information is represented as a grey scale in the image, called Depth image or D-image. The rgb image with depth information is called RGB-D image and the cameras that capture this type of image are called RGBD cameras.

Eq. 3.11 shows that depth and disparity are inversely proportional, meaning, nearby objects are easier to distinguish compared to objects that lie further away.

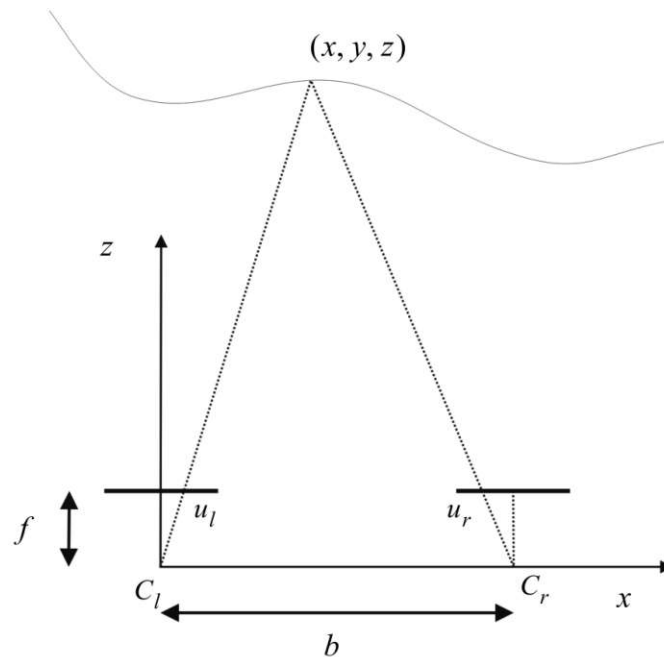


Figure 3.7: Stereo system [41]

3.3.2 Epipolar Geometry

In computer vision, passive stereo vision is one of the most studied fields. In order to understand it, one important concept is the “epipolar constraint”. Epipolar geometry

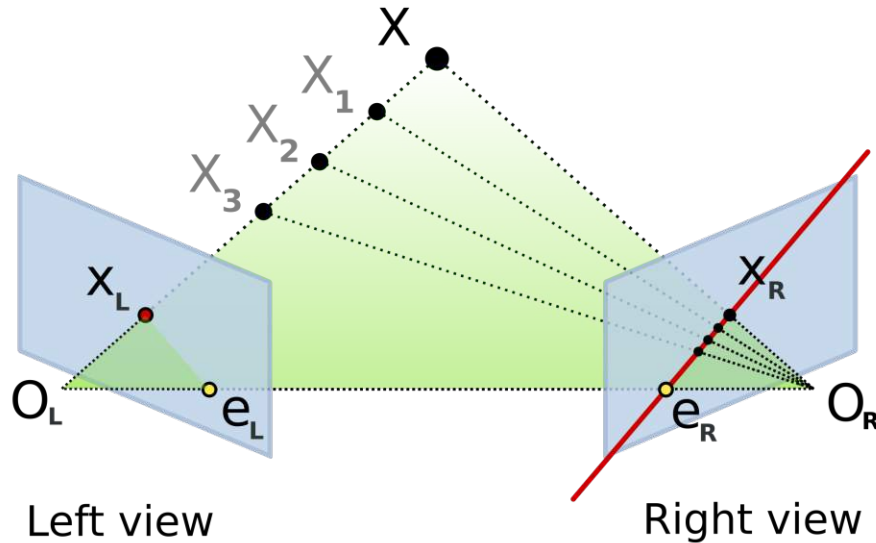


Figure 3.8: Epipolar geometry in stereo vision [42]

describes the intrinsic projective geometry between two views.

Consider a single camera viewing a 3D point X in the world. X must lie on the ray passing through the optical center (O_L) and position (X_L) on the image plane 3.8. However, from a single camera alone, depth estimation along the ray is not possible.

Now, consider a second camera viewing the same 3D point X with an optical center O_R . From the left camera, it is known that the point lies somewhere along the ray in 3D space. It follows that the projected position X_R of this point in the second image must lie somewhere along the projection of this ray in the second image. The ray in 3D projects to a 2D line which is known as an epipolar line (e_R in red). Therefore, for any point in the first image, the corresponding point in the second image is constrained to lie on a line. This is known as the 'epipolar constraint'. The particular line that it is constrained to on depends on the intrinsic and extrinsic parameters of the cameras.

Epipoles

Consider a number of points in the first image 3.8. Each is associated with a ray in 3D space. Each points projection is on a line on the right image (red line intersecting e_R and X_R). This line is called the right epipolar line. The plane between the two optical centers and the line 'X' is called the epipolar plane. The intersection of the epipolar plane and the left image is called the left epipolar line. The line through the left and the right optical center is called the baseline. The intersection between the baseline with the left and right image correspond to the left (e_L) and right (e_R) epipoles, respectively. Consequently, all epipolar planes pass through the baseline, also called epipolar pencil. Therefore, all epipolar lines pass through the epipoles. In other words, the epipoles are the intersection of all the epipolar lines 3.9.

To summarize, given the intrinsic and extrinsic parameters, point correspondences can be found relatively easily. For a given point in the first image, a 1D search is performed along

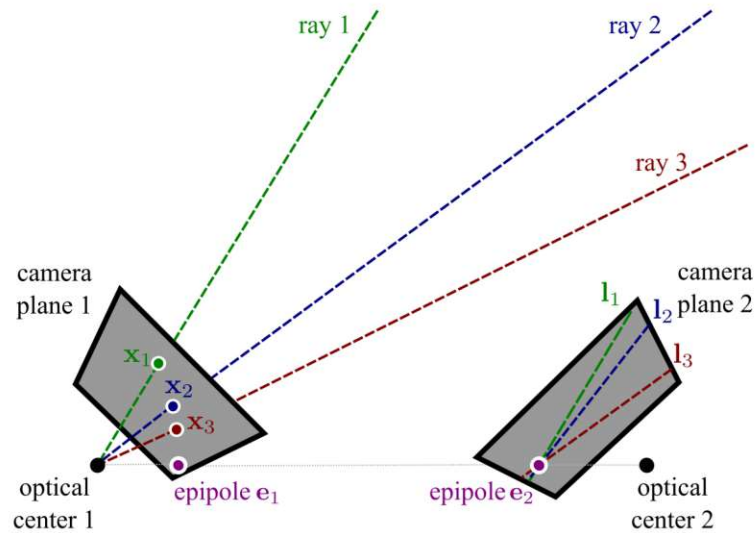


Figure 3.9: Epipoles [39]

the epipolar line in the second image for the corresponding position. As the constraint on the corresponding points is the function of intrinsic and extrinsic parameters, extrinsic parameters can be determined by using the observed point of correspondence and the intrinsic parameters, thereby, establishing the geometric relationship between the two cameras.

The problem with this constraint is that each pair of epipolar lines have a different direction in both the left and right images, significantly increasing the problem difficulty. The solution, called image rectification, consists of modify the images, so that the epipolar lines are on the same horizontal lines.

3.3.3 Fundamental and Essential Matrices

The fundamental matrix F and essential matrix E are crucial in describing the geometric relationship between two camera views. This section will describe the geometric relation between two cameras in the form of a mathematical model.

Nomralized Image Coordinates

Normalized image coordinates \tilde{m}_i refer to adjusted coordinates independent of the intrinsic parameters of a camera. The coordinates are typically in a unit space, where the focal length \mathbf{f} is set to 1mm, thereby, removing distortions introduced by the intrinsic parameters. For a point \mathbf{X} in 3D space is imaged as \mathbf{m}_i , the normalized coordinates are:

$$\tilde{m}_i = K_i^{-1} \cdot m_i \quad (3.12)$$

where \mathbf{K} is the intrinsic matrix.

Essential Matrix

The essential matrix \mathbf{E} establish constraints between matching image points but only in relation to calibrated cameras because the inner camera parameters must be known to achieve pixel normalization.

For a point \mathbf{X} in 3D space is imaged as \mathbf{m}_1 in the first view and \mathbf{m}_2 in the second view, the following epipolar constraint must hold:

$$\tilde{m}_2^T \cdot \mathbf{E} \cdot \tilde{m}_1 = 0 \quad (3.13)$$

where \mathbf{E} is the essential matrix, \tilde{m}_1 and \tilde{m}_2 are conjugate points in normalized image coordinates. The epipolar geometric constraint can be expressed in terms of normalized image coordinates in the equation 3.13.

Fundamental Matrix

The fundamental matrix \mathbf{F} is a 3x3 matrix of rank 2, i.e. it's determinant is zero. It encapsulates the epipolar intrinsic geometry. For a point \mathbf{X} in 3D space is imaged as \mathbf{m}_1 in the first view and \mathbf{m}_2 in the second view, then the image point satisfy the realtion,

$$\tilde{m}_2^T \cdot \mathbf{F} \cdot \tilde{m}_1 = 0 \quad (3.14)$$

From Eq. 3.12, substituting the expressions for $\hat{\mathbf{m}}_1$ and $\hat{\mathbf{m}}_2$ gives:

$$(\mathbf{K}_2^{-1} \mathbf{m}_2)^T \mathbf{E} (\mathbf{K}_1^{-1} \mathbf{m}_1) = 0 \quad (3.15)$$

The Eq. 3.15 can be written as:

$$\mathbf{m}_2^T (\mathbf{K}_2^{-T} \mathbf{E} \mathbf{K}_1^{-1}) \mathbf{m}_1 = 0 \quad (3.16)$$

Comparing this with the epipolar constraint in Eq. 3.14, it can be concluded:

$$\mathbf{E} \approx \mathbf{K}_2^T \mathbf{F} \mathbf{K}_1 \quad (3.17)$$

Where \mathbf{K}_1 and \mathbf{K}_2 are the intrinsic camera matrices of the first and second cameras, respectively. This transformation accounts for the cameras' intrinsic parameters, converting pixel coordinates into normalized image coordinates. This relationship allows us to calculate the essential matrix \mathbf{E} given the fundamental matrix \mathbf{F} and the intrinsic matrices of the cameras. It provides a bridge between pixel-based correspondences (in \mathbf{F}) and normalized, metric-based correspondences (in \mathbf{E}).

3.3.4 Stereo Calibration

Camera calibration is an offline process to determine the intrinsic parameters as well as distortion coefficients of a single camera. Building up on this, stereo calibration is a process to determine the geometric relationship (intrinsic and extrinsic parameters) between two cameras of a stereo system. This geometric relationship translates to the rotation matrix \mathbf{R} and the translation vector \mathbf{T} between the two cameras. By default the relation between two cameras in a stereo system is known. But this relation between two cameras is susceptible to change over time. Stereo calibration accounts for the change

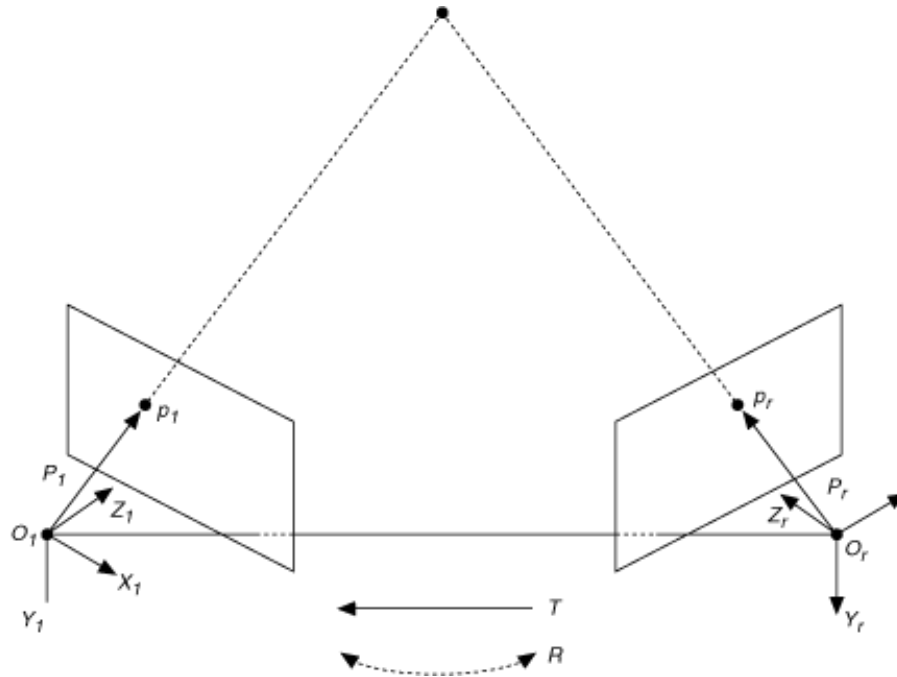


Figure 3.10: Epipoles [43]

in relation by estimating the measurable rotation and translation between two cameras. Camera calibration typically using a checkerboard pattern with odd rows and even column or viceversa with known dimensions. The inherent characteristic of a checkerboard pattern makes it easier to recognize its corner points in both stereo images. The process involves capturing image of the checkboard placed in front of the stereo system from different viewpoints. A point \mathbf{P} is projected to both images with coordinates \mathbf{P}_l and \mathbf{P}_r , respectively. Assuming the rotation matrices (\mathbf{R}_l , \mathbf{R}_r) and translation vectors (\mathbf{T}_l , \mathbf{T}_r) from the cameras to the point \mathbf{P} , the individual projection is calculated through the camera modeling as:

$$\mathbf{P}_l = \mathbf{R}_l \mathbf{P} + \mathbf{T}_l \quad \text{and} \quad \mathbf{P}_r = \mathbf{R}_r \mathbf{P} + \mathbf{T}_r. \quad (3.18)$$

From the Fig 3.12, the relation between the two views of \mathbf{P} are related by:

$$\mathbf{P}_l = \mathbf{R}^T (\mathbf{P}_r - \mathbf{T}) \quad (3.19)$$

Solving the Eq. 3.18 and Eq. 3.19 for the rotation and translation yields:

$$\mathbf{R} = \mathbf{R}_r (\mathbf{R}_l)^T \quad \text{and} \quad \mathbf{T} = \mathbf{T}_r - \mathbf{R} \mathbf{T}_l. \quad (3.20)$$

Given enough data points, the rotation matrix (\mathbf{R}) and translation vector (\mathbf{T}) defining the relation between two cameras can be estimated via Eq. 3.18, Eq. 3.19 and Eq. 3.20. Keep in mind, that different points do not always results in the same rotation matrix and translation vector due to different errors, for instance, noise and rounding error. The main task is to minimize the overall error by estimating the parameters.

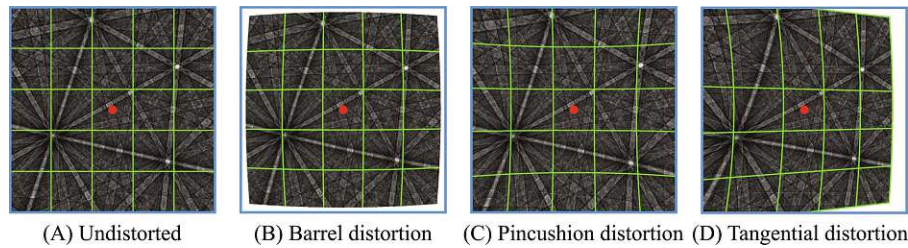


Figure 3.11: Distortion [44]

3.3.5 Distortion

As mentioned towards the end of the section 3.2.1, lens are utilized to overcome the limitations of the simple pinhole model. The disadvantage includes systematic errors and distortions inherent to lens design and manufacturing process. Two lenses produced under similar environmental conditions may slightly differ and create distortion errors. This is especially the case for low-cost lenses. Complex production process would result in minimal errors to a certain degree. The errors are described through mathematical models to correct the most common one. For this reason, camera calibration is used to estimate the necessary parameters. There are different types of distortion including radial, barrel, pincushion and tangential distortion. The most common distortion are radial and tangential distortion which will be briefly discussed below:

Radial Distortion

Radial distortion occurs when light rays passing through the lens farther away from the center appear curved compared to the rays closer to the center. This is due to the shape of the lens. For radial distortions, the distortion is zero at the optical center of the imager and increases as we move toward the edge. In practice, this occurs when the field of view of the lens system is large. It can easily be detected in an image, because straight lines in the world no longer project to straight lines in the image as seen in the Fig 3.11. The radial distortion error is approximated by Taylor series:

$$x_{\text{corrected}} = x \left(1 + k_1 r^2 + k_2 r^4 + k_3 r^6 \right) \quad (3.21)$$

$$y_{\text{corrected}} = y \left(1 + k_1 r^2 + k_2 r^4 + k_3 r^6 \right) \quad (3.22)$$

Where \mathbf{x} and \mathbf{y} are the original coordinates of a point in the image plane, \mathbf{r} is the radial distance from the principal point and $\mathbf{k1}$, $\mathbf{k2}$ and $\mathbf{k3}$ are the distortion parameters.

Tangential Distortion

Tangential distortion occurs due to the lens not being exactly parallel to the imaging plane as a consequence of manufacturing defects. The error is severe for a point further away from the center and can be expressed as:

$$x_{\text{corrected}} = x + \left(2p_1 y + p_2 \left(r^2 + 2x^2 \right) \right) \quad (3.23)$$

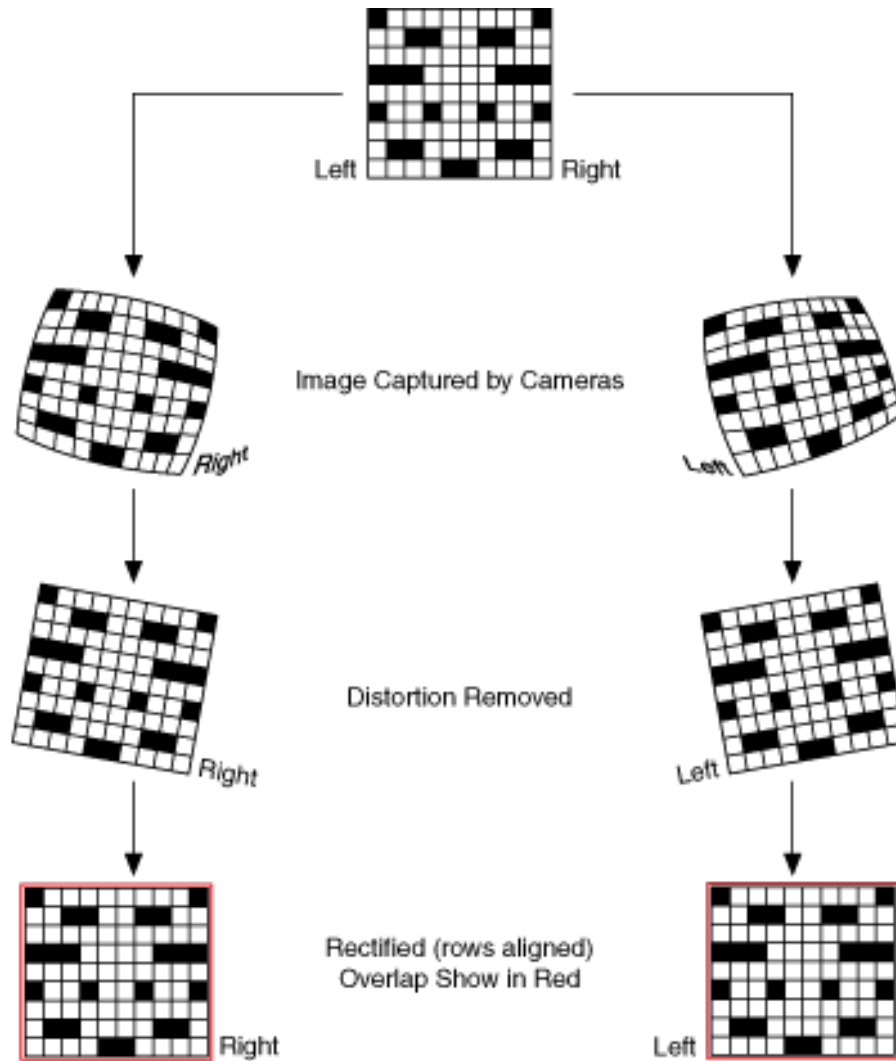


Figure 3.12: Image rectification in stereo vision [45]

$$y_{\text{corrected}} = y + \left(p_1 (r^2 + 2y^2) + 2p_2 y \right) \quad (3.24)$$

3.3.6 Image Rectification

Image rectification is the process of transforming stereo images so that pairs of conjugate epipolar lines become collinear and parallel to the horizontal image axis. This simplifies the stereo correspondence problem to a 1D search along corresponding scanlines. The complete process can be seen in the Fig 3.12.

The process involves a pair of images captured by a stereo vision system which are distorted and non-rectified. Firstly, the distortion is removed from the images. The images are stereo-rectified by calculating image transformations, based on homographies and stereo properties, such as, fundamental and essential matrices discussed above which transform the images so that the epipolar lines are parallel. Correspondence is made line

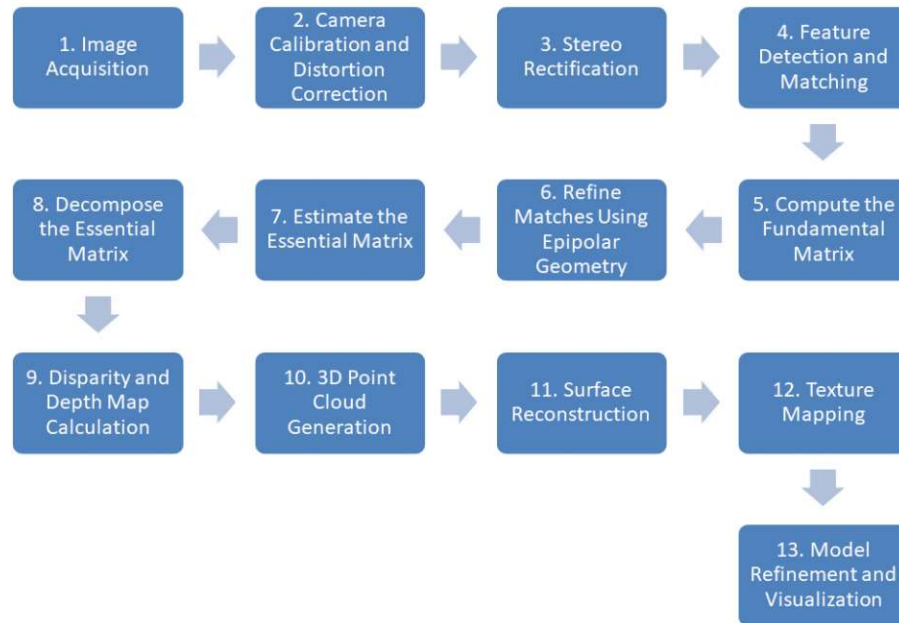


Figure 3.13: Reconstruction pipeline

by line in the same horizontal line.

3.3.7 Stereo 3D reconstruction pipeline

3D reconstruction is the process of creating three-dimensional models from two-dimensional data, such as images or depth maps. It's a critical component in stereo vision systems and has significant applications in different industries including but not limited to robotics, medical, manufacturing and automotive etc...

Fig. 3.13 illustrates the pipeline for reconstructing a 3D model from a stereo image pair, incorporating essential processes such as epipolar geometry, camera calibration, distortion correction, and image rectification as discussed previously in this section.

3.4 PointCloud

The output of a stereo vision system is either a depth map or the point cloud of a scene. A point cloud is a fundamental data structure that represents the three-dimensional geometry of a scene. Point clouds are composed of discrete data points, typically representing the external surface of objects. A point cloud is a collection of points defined by their three-dimensional coordinates (X, Y, and Z), capturing the spatial characteristics of a scene. Point clouds provide a direct representation of 3D geometry and are the primary output of 3D scanning and reconstruction techniques. A point cloud can be either an organized point cloud or an unorganized point cloud. The organized point cloud have a structured grid layout corresponding to the pixel array of a stereo camera, RGB-D camera or a structured light camera as opposed to an unorganized point cloud lacking

the inherent grid structure captured from multiple sources or LiDAR. Analyzing a point cloud involves the following common operations:

- Registration: Aligning multiple point clouds into a common coordinate system.
- Filtering: Removing noise and outliers.
- Downsampling: Reducing the number of points for computational efficiency.
- Segmentation: Dividing the point cloud into meaningful segments.
- Surface reconstruction: Converting the point cloud into a continuous surface representation.

Given that point clouds are a fundamental output in 3D reconstruction, accurately capturing the three-dimensional geometry becomes increasingly difficult for objects with low texture and small-scale features, typical in AM products. This challenge necessitates a specialized assessment methodology to evaluate the effectiveness of stereo vision under such conditions.

4 SAAPF Framework

As highlighted in Chapter 3, accurately matching corresponding features in two images to compute disparity is central to stereo vision. The process, however, becomes problematic for surfaces with insufficient texture, leading to inaccurate disparity calculations and ultimately poor depth estimation. The precision of stereo vision systems is directly tied to the quality of the point clouds generated. This challenge is particularly pronounced when dealing with low-texture, small-scale objects, where these point clouds frequently exhibit inaccuracies due to ambiguity in disparity computation. To address this challenge, this chapter introduces the **Stereo Accuracy Assessment in AM via Plane Fitting (SAAPF)** framework, applicable broadly to environments with uniform, low texture such as those found in AM.

The SAAPF framework is specifically designed to evaluate the performance of stereo vision systems in scenarios with minimal textural information. It incorporates advanced techniques such as plane fitting, C2C computation, and statistical assessments using mean and standard deviation—drawing on methodologies reviewed in the literature that emphasize the necessity for precise estimates and robust evaluation metrics in complex imaging scenarios [6], [7].

4.1 Evaluative Techniques in the SAAPF Framework

Building upon existing research that has explored various aspects of stereo vision accuracy, the SAAPF framework enhances and tailors these techniques to better suit environments with uniform, low texture. The SAAPF framework process is as follows:

- **Plane Fitting:** Inspired by the integration of dense and sparse depth data in studies such as those by D’Angelo et al. [6], plane fitting is utilized to define reference surfaces with high precision, crucial for environments where traditional methods often fail. Given that the reference surfaces are manually segmented and fitted with planes, the use of **Cloud-to-Cloud (C2C)** distance measurement becomes more viable. By reducing the complexity of the surface geometry through accurate plane fitting, the C2C approach can effectively handle point cloud comparisons without the need for more advanced techniques like M3C2. The simplified and well-defined geometry from manual segmentation ensures that nearest-point distance calculations will be accurate and reliable for this application.
- **Cloud-to-Cloud (C2C) Distance:** Extending the cloud comparison techniques like those discussed by Stumpf et al. [17], these metrics enable us to evaluate the spatial deviations and ensure dimensional accuracy of the reconstructed models.
- **Statistical Evaluation:** These methods are used to rigorously assess the statistical accuracy of the stereo vision outputs, ensuring the reliability and consistency of

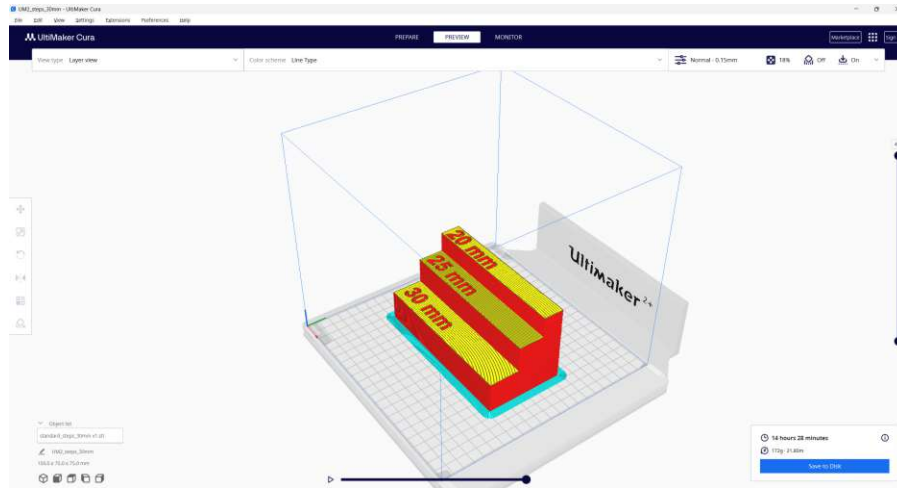


Figure 4.1: Ultimaker 2+ Cura

the measurements, much like the robust evaluations seen in pavement technology research by Mathavan et al. [9].

4.2 Hardware Components

To ensure the reliability and repeatability of the SAAPF methodology, several preparatory measures were taken before conducting the experiments. The accuracy of this framework depends on maintaining precise environmental controls, thorough equipment calibration, and standardized workspace settings. The following procedures were implemented to create a stable and reproducible testing environment:

4.2.1 Ultimaker 2+

The Ultimaker 2+ is a high-quality desktop 3D printer recognized for its precision, reliability, and versatility in the realm of AM. This printer was chosen to fabricate the reference objects due to its capability to produce intricate geometries with fine detail, which is critical for evaluating stereo vision systems.

The Ultimaker 2+ is equipped with interchangeable nozzles that range from 0.25mm to 0.8mm in diameter. For this study, a 0.4mm nozzle was used. The printer supports various materials, including PLA, ABS, and specialized filaments such as PVA and Nylon. PLA (Polylactic Acid) was selected for the reference objects due to its dimensional stability, ease of printing, and minimal warping, which ensures consistent layer adhesion and reliable results. The Ultimaker 2+ is fully integrated with Ultimaker Cura, an intuitive slicing software that enables extensive customization of print settings. For this study, the print resolution was set to 0.15mm, with additional parameters such as layer height, print speed, and infill density configured using the default Generic PLA (0.4mm nozzle) profile. Fig. 4.1 illustrates the slicing process in the Ultimaker Cura software.

4.2.2 Staircase Reference Models

The first step in assessing stereo camera accuracy is selecting a reference object that is well-suited to the task. For this study, a staircase pattern was chosen due to its geometric properties, making it particularly effective for depth evaluation. Due to limitations of the Ultimaker 2+ printer, the reference object was divided into four separate staircase models, each featuring sequentially decreasing depth levels as shown in Fig. 4.2. The specific dimensions of the staircase models are:

1. 30mm, 25mm, 20mm
2. 19mm, 18mm, 17mm, 16mm, 15mm
3. 14mm, 13mm, 12mm, 11mm, 10mm
4. 10mm, 9mm, 8mm, 7mm, 6mm

The staircase structure provides multiple depth levels within a single object, enabling detailed analysis of the system's ability to accurately reconstruct varying depth levels. Additionally, the sharp edges and smooth surfaces of the staircase pattern are ideal for evaluating surface reconstruction and edge detection. Each model represents a series of progressively decreasing step heights, allowing an in-depth analysis of the stereo camera's performance in capturing various depth levels with precision. The geometric consistency of the staircase pattern supports quantitative assessment through techniques such as plane fitting, angle measurements, and cloud-to-cloud distance analysis. The predefined dimensions of each step serve as reliable benchmarks against which the stereo system's outputs can be compared.

The dimensions and step heights were carefully controlled during fabrication to meet the experimental requirements. Since the 3D printer utilizes a single material and does not involve post-processing techniques such as additional texturing or smoothing, the resulting reference object has a uniform, low-texture surface. Before conducting the experiments, the geometry of the object was validated through precise measurements to confirm its adherence to the intended design specifications. This uniform reference object offers a robust basis for evaluating the stereo vision system's accuracy, presenting a well-defined structure that effectively tests the system's ability to reconstruct depth in environments with minimal texture.

4.2.3 Camera Setup

The workspace for stereo vision assessments is meticulously crafted to maximize consistency and accuracy in the imaging process, as demonstrated in Figure 4.3. This setup has been tailored specifically to meet the demands of stereo vision technology, focusing on optimizing environmental conditions, material properties, and precise camera positioning.

The reference objects are printed using generic Polylactic Acid (PLA), selected for its ease of printing, dimensional stability, and relatively consistent surface properties. These characteristics are essential for ensuring uniformity in the assessments. Due to the inherently low texture of PLA surfaces, precise lighting and imaging techniques are crucial for capturing accurate depth information.

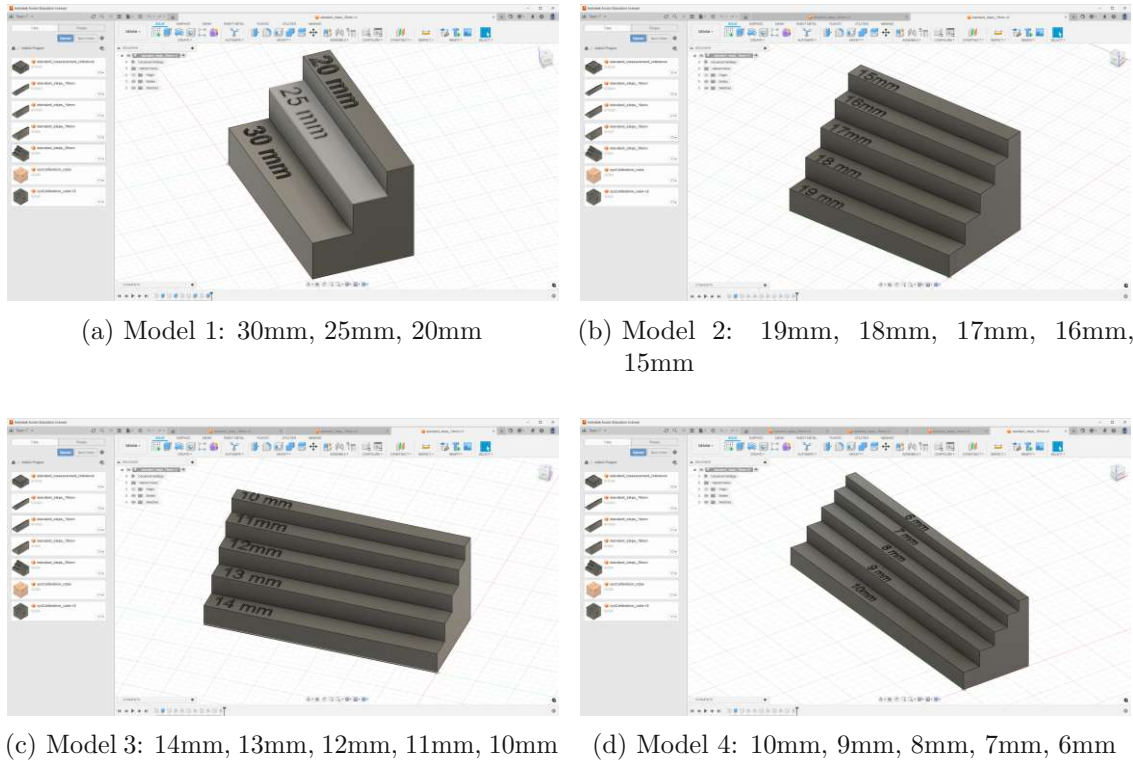


Figure 4.2: Reference staircase models

The workspace is configured in a typical office environment, where ambient lighting is primarily provided by natural light from an adjacent window. This arrangement not only ensures stable and diffused lighting to minimize harsh shadows and reflections but also mimics the lighting conditions typically encountered in real-world applications of the stereo vision systems.

The Intel RealSense D415 camera is strategically placed 50 cm away from the reference object. This distance, verified by a tape measure for accuracy, is optimal for the camera's field of view and focus depth. Such placement allows for an adequate imaging scale to comprehensively capture the object while maintaining the resolution necessary for detailed depth analysis. The camera is securely mounted to avoid any movement that could introduce errors in depth perception and is meticulously aligned to be parallel to the surface being scanned. This alignment is crucial for reducing geometric distortions and achieving high accuracy in depth measurements. Regular checks and adjustments are made to ensure this alignment is maintained, accommodating any potential shifts or environmental effects over time.

Attention is particularly focused on the lighting setup due to the low-texture surface of the printed objects and the need for precise depth measurement. The natural lighting provides a uniform light distribution, ideal for capturing the subtle contours and edges of the PLA objects without creating specular highlights or deep shadows. The position next to the window ensures ample lighting throughout the day, thereby eliminating the need for artificial lighting, which could introduce variability in the lighting conditions.

The design of the workspace also prioritizes the elimination of vibrations and other

disturbances that could affect the accuracy of the stereo vision system. A stable and controlled environment ensures that the experimental results are reliable and reproducible under similar conditions. Safety measures are in place to protect the equipment and personnel from any accidental damage or injury.



(a) Calibration distance measured by tape

(b) Consistent workspace setup

Figure 4.3: Workspace setup consistent with testing conditions.

4.3 Software Components

This section details the essential software components utilized in the SAAPF framework. These tools are integral to the acquisition, processing, and analysis of stereo vision data, each offering unique capabilities that enhance our methodology.

4.3.1 RealSense Viewer

The RealSense Viewer is a powerful tool provided by Intel for use with its RealSense cameras. This application serves as a user interface to visualize and manipulate the raw data captured by the camera as illustrated in the Fig. 4.4. Key features include:

- Real-time preview of both depth and color streams from the camera.
- Control over camera settings such as exposure, gain, and laser power to optimize data capture according to specific environmental conditions.
- Capability to record and save data streams, which can be used for offline analysis and processing.
- Support for multiple cameras, allowing for complex setups and advanced experimental configurations.

4.3.2 CloudCompare

CloudCompare (CC) is a free and open-source software designed for 3D point cloud and mesh processing. It is extensively used in the SAAPF framework for its robust analytical tools and user-friendly interface illustrated in the Fig. 4.5. Key capabilities include:



Figure 4.4: RealSense Viewer High Accuracy Preset

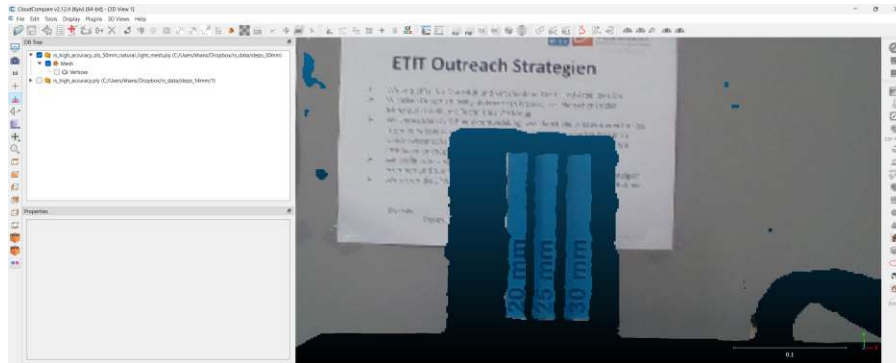


Figure 4.5: Point Cloud Visualization in CC

- Support for multiple file formats, enabling compatibility with data from various sources.
- Comprehensive tools for editing, processing, and analyzing point clouds, such as noise reduction, filtering, and geometrical transformations.
- Advanced features like registration, 3D comparisons, and statistical analysis, which are essential for detailed evaluation of stereo vision accuracies.
- Customizable plugins and scripts, offering flexibility to adapt the software for specific research needs.

Each of these software components plays a pivotal role in the data processing and analysis pipeline of the SAAPF framework, ensuring the successful implementation of the project's objectives.

4.4 Preliminary Setup

Before progressing to the detailed steps of camera calibration and data acquisition, it is crucial to establish a foundational setup that supports the effective implementation of the SAAPF framework. This preliminary setup requires configuring the necessary hardware, preparing the software environment, and ensuring that all components are seamlessly integrated and functioning correctly. One of the key components of this setup is ensuring stable mounting of the Intel RealSense D415 camera to maintain a constant distance of 50cm from the target throughout all testing phases, including calibration and data acquisition. This stability is vital for preserving the integrity of the depth measurements and ensuring consistent results. The Intel Depth Quality Tool is employed for precise calibration, while the RealSense Viewer is utilized to manage data acquisition and to verify the RGB and depth streams, ensuring the camera is operating correctly and is in good condition. These preparatory steps minimize variables that could affect the accuracy and reliability of subsequent experimental procedures, laying a solid groundwork for precise evaluations and analyses.

4.4.1 Camera Calibration

This section details the calibration process for the Intel RealSense D415 camera, specifically utilizing an active test with a textureless white target in an office environment, as outlined in the referenced document [46]. The aim is to ensure accurate depth measurements by appropriately configuring the target, camera, and lighting conditions.

The target employed for calibration is a smooth, white, matte surface known for its high diffuse reflectivity. It is strategically positioned 51 cm from the camera, within the recommended range of 50 cm to 2 meters, and aligned parallel to the camera's imaging plane as stipulated in the reference document. This precise alignment is crucial for accuracy and can be verified using the Depth Quality Tool provided by Intel. This tool is pivotal for providing real-time feedback and assists in the accurate measurement of depth. It ensures that the target's orientation relative to the camera remains within a permissible deviation of less than 5 degrees.

Calibration is conducted under standard office lighting conditions, which are sufficient for active tests. In these settings, the depth camera's projector effectively enhances the target's texture, crucial for accurate depth measurement. The tool also automatically generates metrics and visualizations, such as 3D point clouds, to facilitate real-time evaluation of depth data quality.

Camera settings should be adjusted based on feedback from the tool to optimize performance. The Depth Quality Tool is capable of saving all relevant data, including images and settings, for further analysis or documentation.

Table 4-14. Depth Quality Specification

Metric	D410/D415 (≤ 2 Meters and 80% ROI, HD Resolution)	D430/D435/ D435i/D435f/D435if (≤ 2 Meters and 80% ROI, HD Resolution)	D450/D455/ D455f/D456 (≤ 4 Meters and 80% ROI, HD Resolution)	D401/D405 (≤ 0.5 Meters and 80% ROI, HD Resolution)
Z-accuracy (or Absolute Error)	$\pm 2\%$	$\pm 2\%$	$\pm 2\%$	$\pm 2\%$
Fill rate	$\geq 99\%$	$\geq 99\%$	$\geq 99\%$	$\geq 99.5\%$
RMS Error (or Spatial Noise)	$\leq 2\%$	$\leq 2\%$	$\leq 2\%$	$\leq 1\%$
Temporal Noise	$\leq 1\%$	$\leq 1\%$	$\leq 1\%$	$\leq 0.5\%$
Lifetime	4 years	5 years	5 years	5 years

Figure 4.6: Visualization of RealSense D415 Depth Quality Specifications [47]

The calibration parameters acquired using the dedicated Depth Quality Tool by Intel meet the depth quality specifications shown in Figure 4.6. Table 4.1 displays the real-time calibration parameters using both high accuracy and high density presets.

4.4.2 Data Acquisition

The data acquisition phase is systematically organized to collect comprehensive stereo vision datasets across various models and under different presets, as detailed in the

Table 4.1: Comparison of Calibration Parameters for Intel RealSense D415: High Accuracy vs. High Density

Parameter	High Accuracy	High Density
Resolution	1280 x 720	1280 x 720
Frame Rate (FPS)	30	30
Region of Interest	40%	40%
Distance (mm)	501.30	501.45
Ground Truth (mm)	510	510
Angle (degrees)	4.09	4.07
Fill-Rate (%)	99.78	100.00
Z Accuracy (%)	-1.47	1.49
Plane Fit RMS Error (%)	0.37	0.40
Subpixel RMS Error (pixels)	0.34	0.37

structured flowchart illustrated in the Fig. 4.7. This phase is critical for gathering the necessary data to effectively apply and test the SAAPF framework.

The camera, an Intel RealSense D415, is mounted on a robust tripod and precisely aligned 50 cm away from the target models in a controlled office environment with consistent natural lighting. The setup ensures that the lighting conditions remain stable, utilizing ambient light from an adjacent window to illuminate the scene naturally.

- **Camera Positioning and Stability:** The camera’s alignment and distance are rigorously checked before each session to maintain the integrity of the depth measurements.
- **Lighting Conditions:** The constant natural lighting supports optimal data capture conditions and is monitored to ensure consistency throughout the data acquisition process.

Data is captured under two main camera presets, high accuracy and high density, to ensure the collection of detailed point clouds suitable for in-depth analysis. Each of the four reference models (as specified in Section 4.2.2) is positioned in three distinct poses—horizontal, vertical, and a 45-degree tilt—to capture diverse data scenarios, reflecting the complex dynamics of real-world applications.

- **Reference Models and Poses:** The models are systematically captured in designed poses to maximize data variability and applicability. Each model’s data acquisition is depicted in the flowchart, which outlines the sequence of capturing each pose under both preset conditions.
- **Capture Sessions:** Each session involves recording synchronized point clouds, depth maps, and RGB images, providing a multifaceted dataset that supports subsequent comparative and analytical evaluations.

Meticulous documentation accompanies each capture session, with metadata including lighting conditions, camera settings, and object details. Initial data processing such as

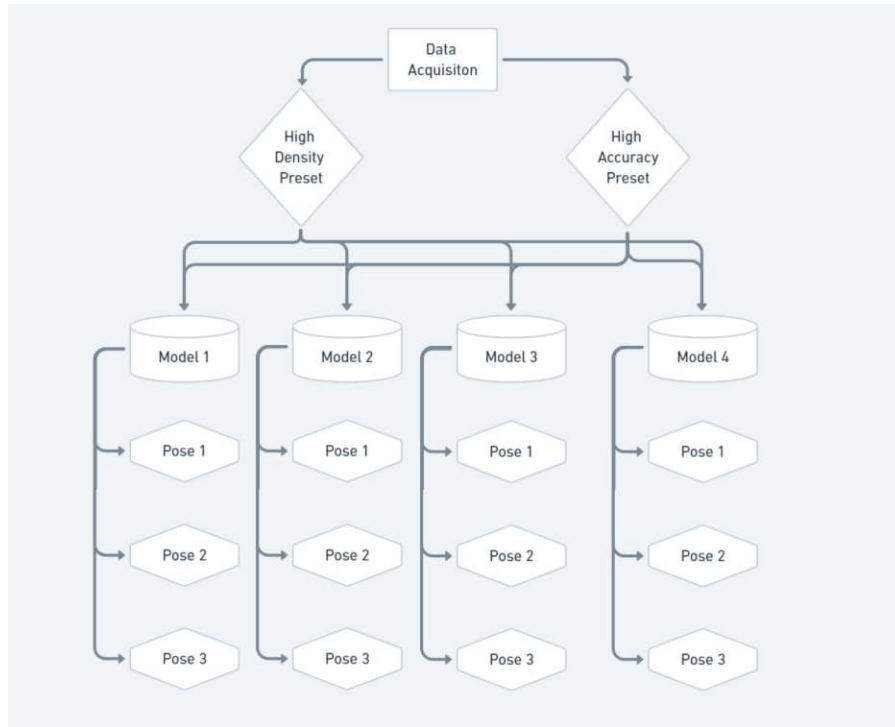


Figure 4.7: Flowchart illustrating the data acquisition process

labeling and preliminary noise filtering is conducted to prepare the datasets for deeper processing and analysis in the framework's later stages.

The structured approach detailed in the flowchart and this section ensures the collection of high-quality data, crucial for the rigorous analysis required within the SAAPF framework. The thoroughness of this data acquisition phase significantly influences the effectiveness and accuracy of the subsequent evaluative techniques.

4.5 Application Methodology

This section outlines the detailed steps for applying the SAAPF framework to evaluate stereovision systems, following preliminary setup, camera calibration, and data acquisition. The methodology is designed to rigorously analyze the system's capabilities in handling complex scenarios using specific software tools and processes.

4.5.1 Data Processing and Analysis

Upon acquiring the necessary data, the subsequent phase involves a structured approach to processing and analyzing the datasets:

- **Importing Data into CC:** Initially, point cloud data is imported into CC, ensuring the software is properly configured for the types of analyses required.
- **Segmentation of Data:** The data is segmented to isolate the staircase model from the surrounding environment, allowing for focused analysis on key components.

- **Cross-sectional Analysis:** Cross-sectional slices of the staircase are generated, facilitating detailed investigation of each individual step.
- **Geometric Evaluations:** Plane fitting techniques are applied to these slices to measure and validate the geometric accuracy of each stair step.
- **Computing Distances:** Cloud-to-cloud distance measurements are carried out between steps to evaluate the precision of the reconstructed model dimensions. Since manual segmentation and plane fitting have been applied, **Cloud-to-Cloud (C2C)** distance measurement is used to compare the reconstructed steps. The plane fitting ensures that each surface is clearly defined, reducing the risk of overestimating distances that might occur in irregular or poorly defined areas. This makes C2C an appropriate and efficient choice for measuring the spatial deviations between steps.

4.5.2 Statistical Analysis and Evaluation

A comprehensive statistical analysis follows to validate the reliability and accuracy of the measurements:

- **Histograms and Gaussian Distributions:** Data distributions are analyzed through histograms and Gaussian fitting, providing insights into data consistency and variance.
- **Comprehensive Evaluation:** All collected data is evaluated to determine the effectiveness of the stereovision system under test, using statistical metrics such as mean error and standard deviation.

5 Experiments & Results

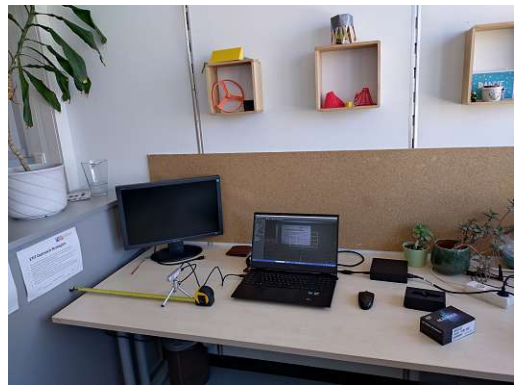
This chapter extends the discussion from Chapter 4, focusing on the empirical validation of the SAAPF Framework. The SAAPF framework is tailored to address and overcome challenges associated with stereo vision systems in AM, particularly in capturing low-texture, small-scale objects. Here, we detail the experiments conducted to evaluate the framework's efficacy, using a structured approach to examine the accuracy of stereo vision adjustments in real-world application scenarios.

5.1 Experimental Setup and Process

As outlined in section 4.2, the experimental setup includes the Intel RealSense D415 camera mounted on a tripod at a fixed distance of 50cm from the object, measured by a tape measure. The system is equipped with Intel RealSense Viewer and CC for data acquisition and analysis illustrated in Fig. 5.1.



(a) Calibration distance measured by tape



(b) Consistent workspace setup



(c) Reference model 1 under study viewed via Intel RealSense Viewer

Figure 5.1: Workspace setup consistent with testing conditions

After completing the hardware configuration, the next step is to acquire data from the

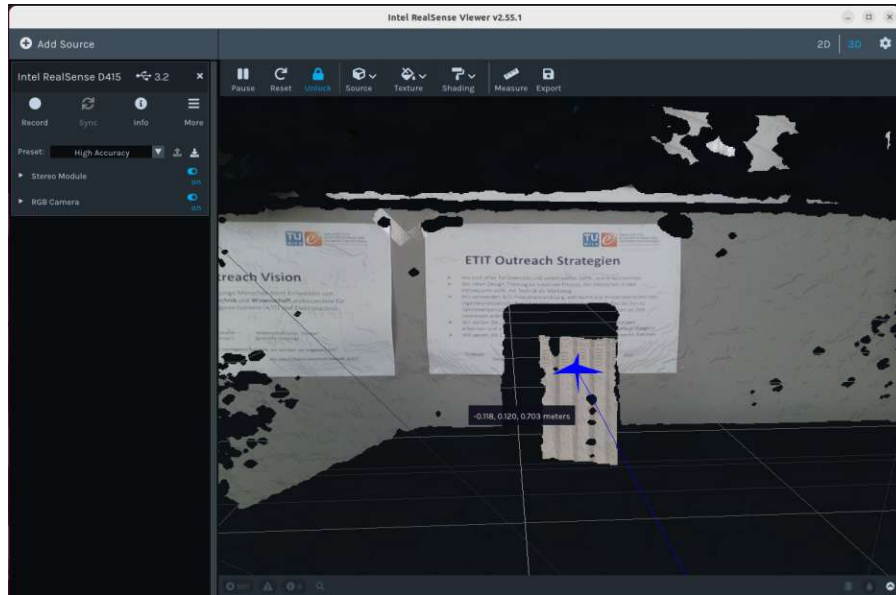


Figure 5.2: Reference model 3 viewed from the Intel RealSense Viewer

reference model under study.

5.1.1 Data Acquisition and Collection

In this step, the camera setup and current lighting conditions are observed to be consistent with the calibrated settings to ensure reliability and repeatability in data capture. Following that the reference model under study is observed from the Intel RealSense Viewer application as illustrated in the Fig. 5.2.

It can be observed that data can be acquired in either 2D or 3D information. Moreover, data information include depth maps, RGB images and the generated points clouds can be viewed in the 3D data panel. Preset can be applied for improved data collection depending on the application. This is critical to acquiring the necessary data for detailed analysis. After being satisfied with the visualized pointcloud, it can be exported as a (.ply) file to offline disk for further analysis.

5.1.2 Data Pre-Processing

In this step, the pointcloud acquired in the previous step is imported into CC. Fig. 5.3 illustrates the pointcloud of the reference model 1 aligned at a distance of 50cm visualized in CC.

The imported pointcloud data is visualized and observed in CC. Based on the observation, the pointcloud data is segmented to isolated the reference model from the background, thereby, focusing on the area of interest. The output of this procedure is the staircase reference model.

The Fig. 5.4(a) illustrates the staircase reference model under the effects of the cross-section tool. The pointcloud under study is obtained from "high accuracy preset" at a distance 50cm and the object is in a vertical pose. The cross-section tool is used to segment the individual planes of the staircase model illustrated in the Fig. 5.4(b).

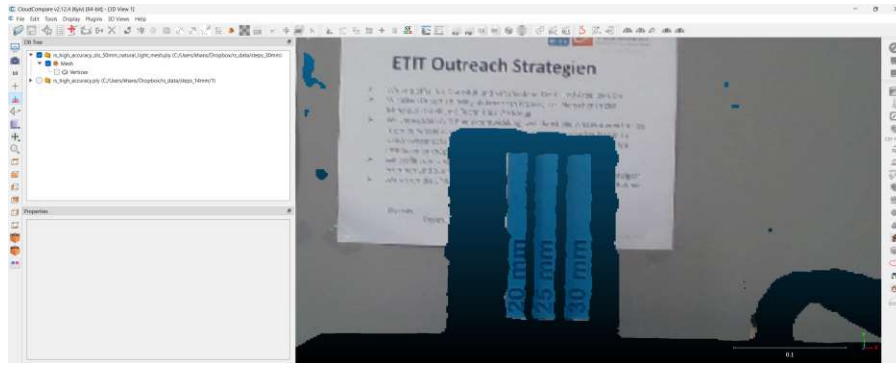
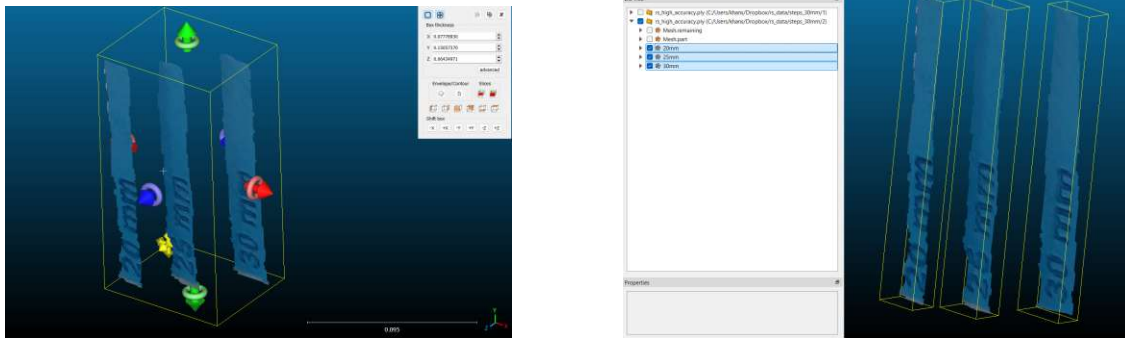


Figure 5.3: Reference model 1 viewed from CC



(a) Reference model 1 viewed from CC

(b) Individual planes of the reference model

Figure 5.4: Data pre-processing carried out in CC

5.1.3 Plane Fitting

The fit plane tool is used to process plane fitting on a surface in CC. Figure 5.5 illustrates a plane fitted on the 20mm step and the console output obtained from this process. The console provides output in the form of RMS 0.000681304, normals $(-0.114052, -0.0894956, 0.989435)$, Dip 8° , Dip direction: 232° , and the orientation matrix. The matrix that would make this plane horizontal (normal towards Z^+) is:

$$\begin{bmatrix} -0.005130687729 & 0.995974004269 & 0.089495643973 & 0.041151460260 \\ -0.114052169025 & -0.089495643973 & 0.989435493946 & -0.007231444120 \\ 0.000000000000 & 0.000000000000 & 0.000000000000 & 1.000000000000 \end{bmatrix}$$

This matrix can be used to transform the plane or associated data to align with the Z^+ axis positively.

5.1.4 Evaluation Techniques

In this section, we apply the evaluation techniques outlined in the SAAPF framework, detailed in Section 4.1, using CC. Each step is designed to systematically assess the accuracy of the stereo vision system.

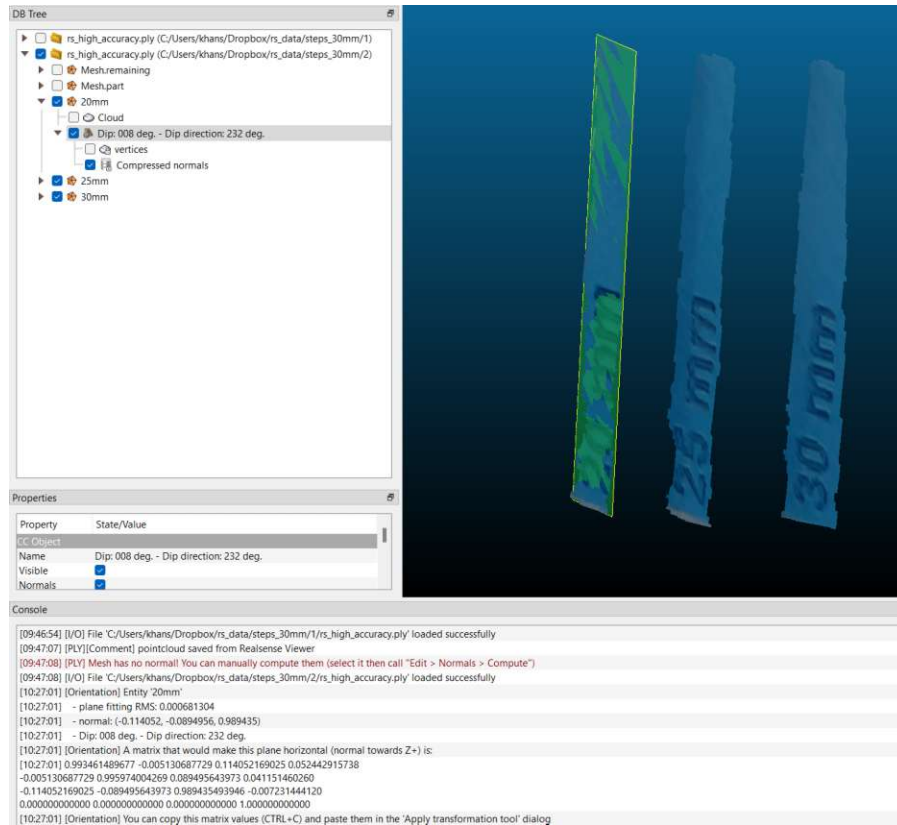


Figure 5.5: Plane fitting on the 20mm step

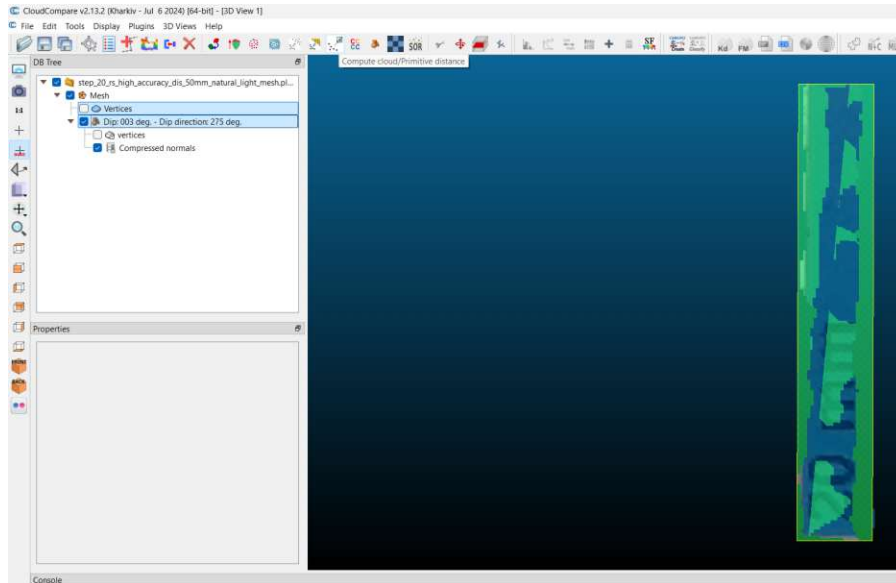


Figure 5.6: Cloud to Primitive distance

Distance Between Primitive and Point Cloud

The initial evaluative technique involves measuring the distance from the point cloud to a fitted plane, which is a critical indicator of accuracy. This is performed in CC by:

1. Selecting the point cloud and the previously fitted plane.
2. Using the *Compute Cloud/Primitive Distance* tool, which calculates the distances from each point in the cloud to the plane.

The results from this tool are presented as follows:

```
[10:55:12] [Compute Primitive Distances] [Primitive: Dip: 007 deg. - Dip
direction: 224 deg.] [Cloud: Cloud] [C2Prim signed distances] Mean distance
= 9.58078e-09 / std deviation = 0.000624496.
```

This output indicates extremely close proximity between the cloud points and the fitted plane, suggesting a high level of accuracy in the plane fitting process illustrated in the Fig. 5.6.

Cloud to Cloud Distance Measurement

The next evaluative step involves:

1. Using the *Compute Cloud/Cloud Distance* tool in CC, which measures the distances between corresponding points in two different point clouds.

The recorded output for this measurement is:

```
[10:57:10] [ComputeDistances] Mean distance = 0.0243906 / std deviation =
0.00362066.
```

This data helps assess the overall alignment and congruence between the two point clouds as illustrated in the Fig. 5.7.

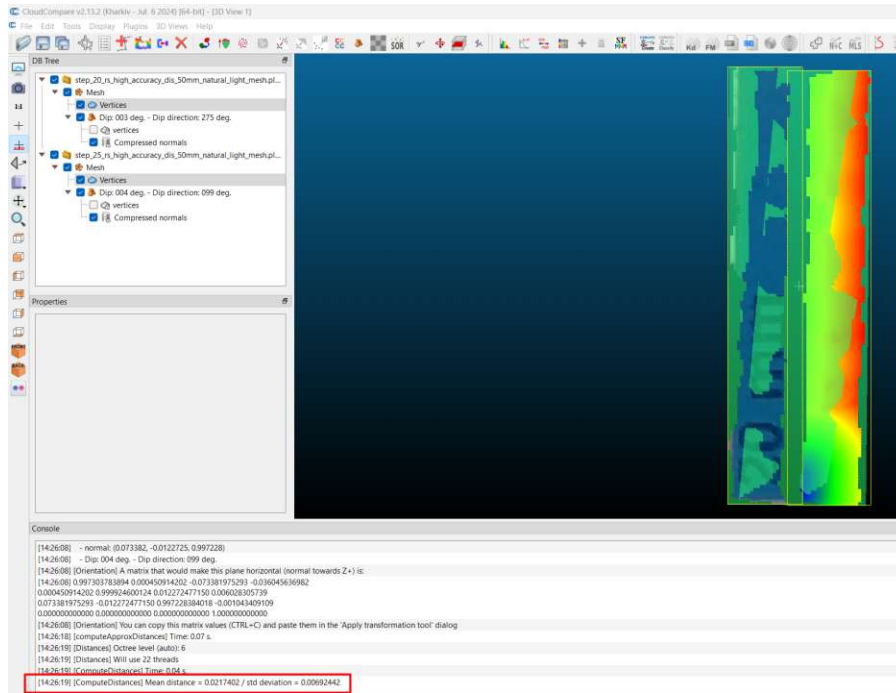


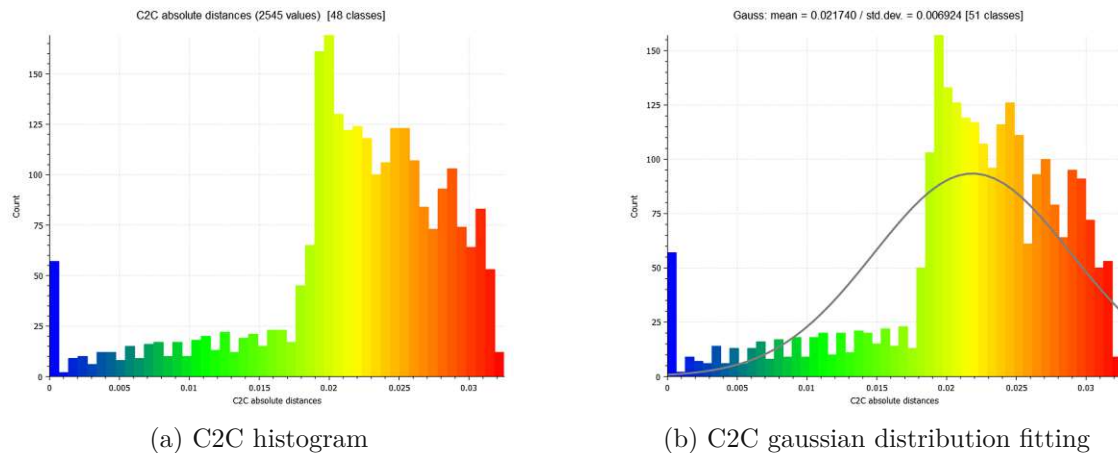
Figure 5.7: Cloud to Cloud distance

Statistical Distribution Analysis

Following the distance measurements:

1. A histogram and Gaussian distribution of the cloud-to-cloud distances are generated to visualize and statistically analyze the data.

These plots are crucial for understanding the variance and central tendency of the measured distances, providing insights into the consistency and reliability of the data as illustrated in the Fig. 5.8.



(a) C2C histogram

(b) C2C gaussian distribution fitting

Figure 5.8: Statistical evaluation of pointcloud data

Each of these techniques incrementally builds our understanding of the stereo vision system's accuracy, playing a pivotal role in the validation process of the SAAPF framework.

5.2 Results

This section presents the findings from applying the SAAPF methodology to metrologically characterize stereo vision systems for low-texture, small-scale surfaces in high-precision manufacturing environments. The primary objective is to determine the smallest accurate measurement that the Intel RealSense D415 can achieve, focusing on cloud-to-cloud (C2C) distance analysis as a key indicator of precision.

While the plane fitting process demonstrated excellent alignment with low RMS and C2Prim distances, it is not the central focus of this research and will not be discussed in detail due to the volume of experiments. Instead, the emphasis is on assessing the precision of the stereo camera system for capturing fine details on low-texture surfaces.

The results are organized into four sections—Model 1, Model 2, Model 3, and Model 4—each representing tests performed on respective reference models. These tests were conducted across three different poses and under two camera presets (high accuracy and high density), as detailed in section 4.4.2.

For each model, the analysis focuses on C2C distance measurements to evaluate precision and variability. This structured approach allows us to determine the minimum reliable measurement resolution of the system. By concentrating on the metrological aspect, we directly address the core research question: what is the smallest measurement that can be accurately captured using stereo vision in additive manufacturing (AM) environments?

5.2.1 Model 1: Detailed Accuracy Assessment

The statistical analysis of the cloud-to-cloud (C2C) distances was conducted using the high accuracy preset of the Intel RealSense D415, demonstrating the accuracy of the equipment used in the experimental setup. The Gaussian distributions, detailed in Figure 5.9, depict the results for two different step measurements.

The C2C distances between the 30mm and 25mm steps are represented in the left subfigure of Figure 5.9. The mean of these distances is 0.028524 with a standard deviation of 0.003439. The histogram shows a symmetric distribution around the mean, indicating consistent and reliable measurements. This distribution points to the camera's accurate performance in capturing the dimensional differences between these two steps.

The right subfigure of Figure 5.9 shows the Gaussian distribution of the C2C distances between the 25mm and 20mm steps. The mean C2C distance for this segment is 0.023443, with a standard deviation of 0.003100. The histogram reveals a nearly normal distribution, though with a slightly skewed tail.

Both histograms affirm the stereovision camera's efficacy in accurately measuring differences between the respective staircase steps, as demonstrated by the low standard deviations and the predominantly Gaussian nature of the data distributions. The analysis confirms the reliability of the measurement techniques and the camera technology employed in this study.

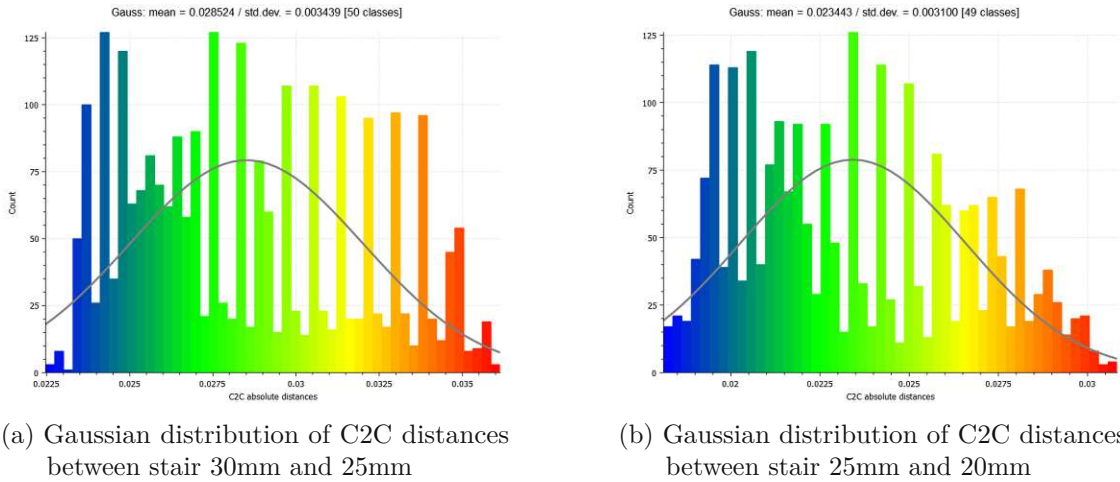


Figure 5.9: Gaussian distributions of C2C distances in Model 1, acquired via a high-accuracy preset

High Density Preset Analysis

The detailed examination of the cloud-to-cloud (C2C) distances under the high density preset of the Intel RealSense D415 stereovision camera provides insight into the accuracy and variability of depth measurements at different step intervals.

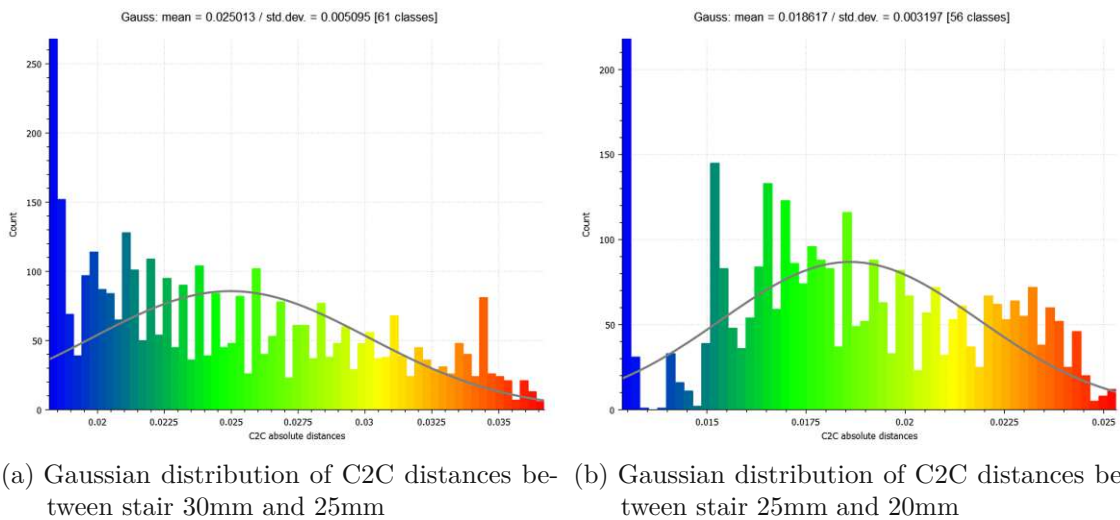


Figure 5.10: Comparative Gaussian distributions of C2C distances for the 30mm-25mm and 25mm-20mm stair steps under the high density preset

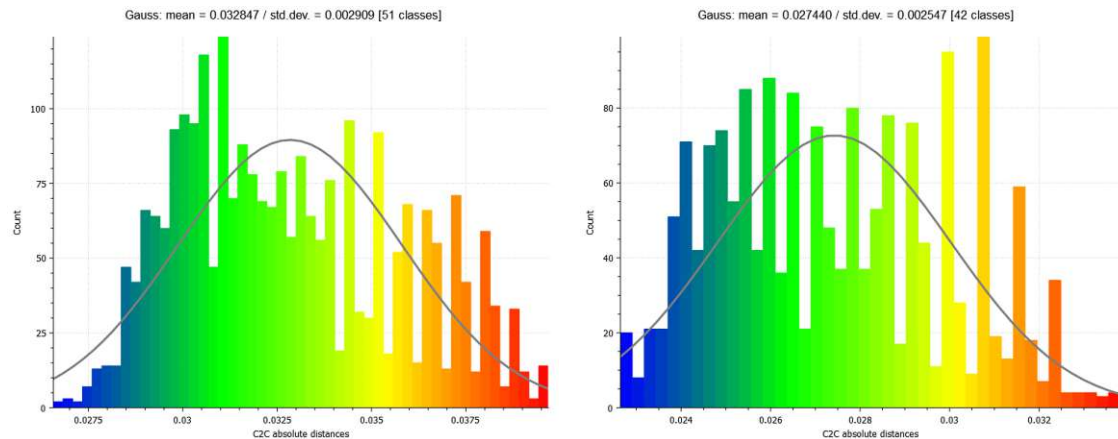
The Gaussian distributions captured under the high density preset show distinct patterns of variability and measurement precision across the two different step measurements.

The first subfigure (Figure 5.10a) presents the Gaussian distribution for the C2C distances between the 30mm and 25mm steps. The mean distance recorded is 0.025013 with a standard deviation of 0.005095, indicating a broad spread in measurements, which suggests higher data capture but potentially increased noise levels.

As shown in the second subfigure (Figure 5.10b), the distances between the 25mm and 20mm steps have a mean of 0.018617 and a standard deviation of 0.003197. This narrower distribution points to better measurement consistency and potentially more accurate segmentation at closer distances within the model.

Pose 2: High Accuracy Preset Analysis

The following presents the Gaussian distribution analysis for the C2C distances between different steps from a different pose of the model, utilizing the high accuracy preset of the stereovision camera. This analysis serves to compare how pose variations might affect the accuracy and consistency of measurements.



(a) Gaussian distribution of C2C distances between stair 30mm and 25mm in Pose 2 using the high accuracy preset. (b) Gaussian distribution of C2C distances between stair 25mm and 20mm in Pose 2 using the high accuracy preset.

Figure 5.11: Comparative Gaussian distributions of C2C distances for the 30mm-25mm and 25mm-20mm stair steps under the high accuracy preset in Pose 2.

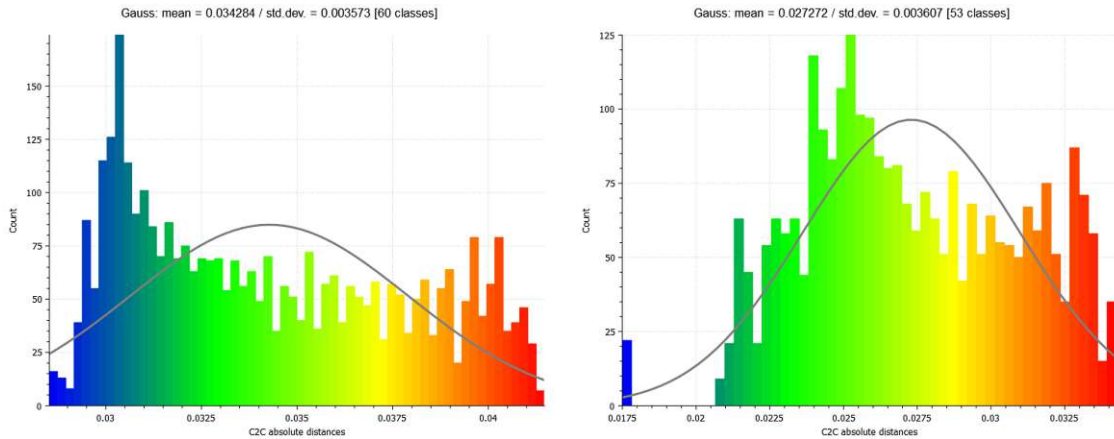
Staircase Steps 30mm and 25mm - Pose 2: The first subfigure (Figure 5.11a) presents a Gaussian distribution with a mean of 0.032847 and a standard deviation of 0.002909. This tight distribution suggests high precision and minimal measurement error.

Staircase Steps 25mm and 20mm - Pose 2: The second subfigure (Figure 5.11b) shows the Gaussian distribution with a mean of 0.027440 and a standard deviation of 0.002547. This also indicates a precise measurement albeit with slightly different characteristics in the distribution, possibly reflecting the physical and optical properties specific to the shorter distance between steps.

Pose 2: High Density Preset Analysis

The following sections present the Gaussian distribution analysis for the C2C distances between different steps from Pose 2 using the high density preset of the stereovision camera. This comparison elucidates the impact of data density on measurement accuracy and variability.

Staircase Steps 30mm and 25mm - High Density: Figure 5.12a indicates a Gaussian distribution with a mean of 0.034284 and a standard deviation of 0.003573. This



(a) Gaussian distribution of C2C distances between stair 30mm and 25mm in Pose 2 using the high density preset. (b) Gaussian distribution of C2C distances between stair 25mm and 20mm in Pose 2 using the high density preset.

Figure 5.12: Comparative Gaussian distributions of C2C distances for the 30mm-25mm and 25mm-20mm stair steps under the high density preset in Pose 2.

distribution suggests a broader spread of data points, reflecting a detailed capture of the surface irregularities which could introduce slight variations in the measurements.

Staircase Steps 25mm and 20mm - High Density: Figure 5.12b shows the Gaussian distribution with a mean of 0.027272 and a standard deviation of 0.003607. Compared to the distribution of the 30mm and 25mm steps, this graph displays a slightly lower mean but comparable variability, indicating consistent performance of the camera across different step measurements under the high density preset.

Pose 3: High Accuracy Preset Analysis

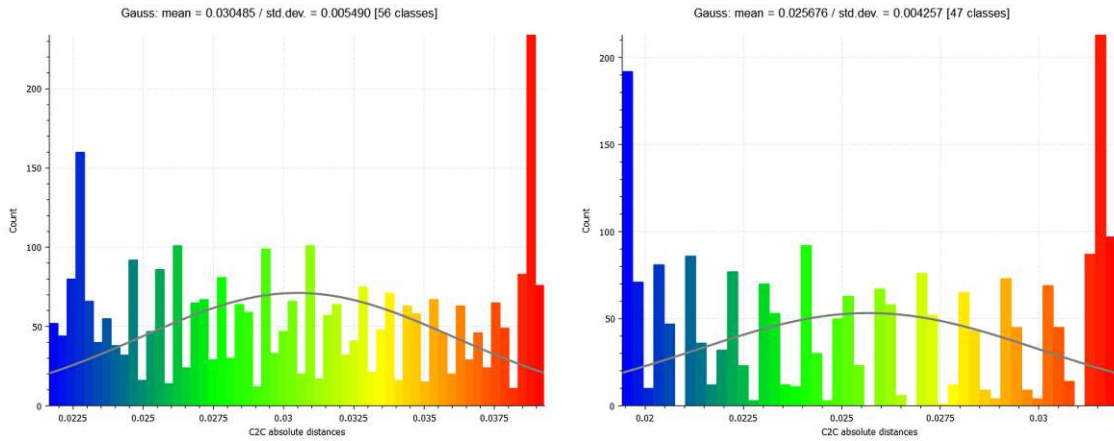
The data presented here is derived from Pose 3 of the model, using the high accuracy preset of the Intel RealSense D415 camera. This analysis aims to assess the Gaussian distribution of the C2C distances, illustrating the effect of pose variations on measurement accuracy.

Staircase Steps 30mm and 25mm - Pose 3: Figure 5.13a shows a Gaussian distribution with a mean of 0.030485 and a standard deviation of 0.005490. This indicates a relatively broad distribution, suggesting minor variances in capturing angle or environmental conditions that could affect the measurements.

Staircase Steps 25mm and 20mm - Pose 3: Figure 5.13b presents a Gaussian distribution with a mean of 0.025676 and a standard deviation of 0.004257. Compared to the distribution between the 30mm and 25mm steps, this shows a tighter distribution, reflecting potentially more consistent data capture for these steps under similar conditions.

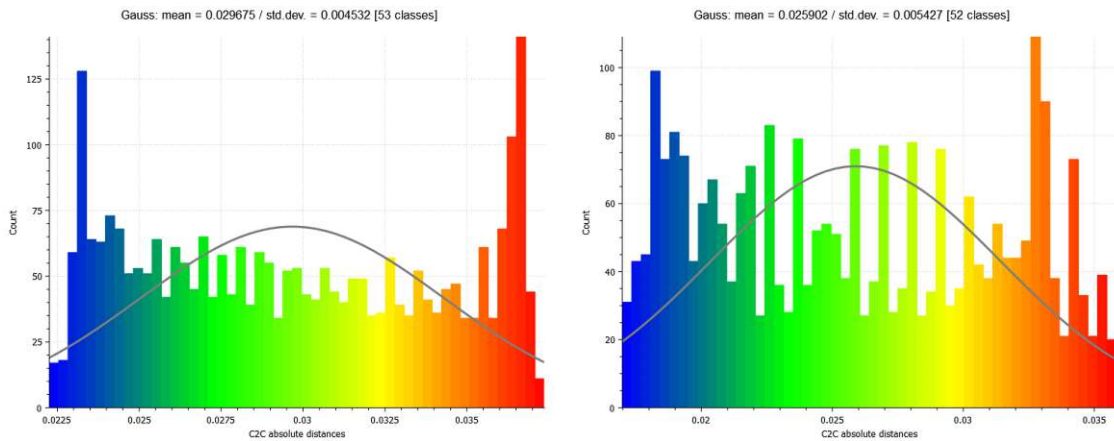
Pose 3: High Density Preset Analysis

This section compares the Gaussian distributions of C2C distances for different step measurements under the high density preset from Pose 3, illustrating how increased data density impacts measurement precision and variability.



(a) Gaussian distribution of C2C distances between stair 30mm and 25mm in Pose 3 using the high accuracy preset. (b) Gaussian distribution of C2C distances between stair 25mm and 20mm in Pose 3 using the high accuracy preset.

Figure 5.13: Comparative Gaussian distributions of C2C distances for the 30mm-25mm and 25mm-20mm stair steps under the high accuracy preset in Pose 3.



(a) Gaussian distribution of C2C distances between stair 30mm and 25mm in Pose 3 using the high density preset. (b) Gaussian distribution of C2C distances between stair 25mm and 20mm in Pose 3 using the high density preset.

Figure 5.14: Comparative Gaussian distributions of C2C distances for the 30mm-25mm and 25mm-20mm stair steps under the high density preset in Pose 3.

Staircase Steps 30mm and 25mm - High Density: As shown in Figure 5.14a, the Gaussian distribution indicates a mean of 0.029675 with a standard deviation of 0.004532, highlighting the increased spread possibly due to higher data density which captures more surface detail.

Staircase Steps 25mm and 20mm - High Density: Figure 5.14b presents a Gaussian distribution with a mean of 0.025902 and a standard deviation of 0.005427. This wider distribution compared to the previous steps under the same preset suggests varying levels of surface complexity or noise in the data capture process.

5.2.2 Summary of Results for Model 1

The stereovision camera's capability to accurately measure the step dimensions of Model 1 was assessed across three poses using two different presets—high accuracy and high density. The dimensions of the steps (30mm, 25mm, and 20mm) were validated against a vernier caliper, providing a precise reference for evaluating the camera's accuracy.

The analysis of Gaussian distributions of cloud-to-cloud (C2C) distances has yielded the following insights into the accuracy of the stereovision camera:

- **High Accuracy Preset:** The mean values recorded across all poses closely matched the actual dimensions of the steps, confirming high accuracy. The standard deviations were generally low, indicating consistent and reliable measurements:
 - Pose 1: Means close to 30mm, 25mm, and 20mm with minimal deviation.
 - Pose 2: Similar performance with slightly increased variability.
 - Pose 3: Consistency maintained with comparable precision.
- **High Density Preset:** While this preset exhibited increased standard deviations due to the higher data density, the mean values still closely aligned with the true step dimensions:
 - Pose 1: Slightly broader distributions reflecting more detailed data capture.
 - Pose 2: Increased variability, yet maintaining near-accurate mean values.
 - Pose 3: Higher measurement spread but continued accuracy in mean values.

The experiments confirm the stereovision camera's accuracy in measuring known distances within a structured experimental setup. The high accuracy preset is particularly recommended for applications requiring stringent accuracy due to its lower variability and reliable measurement closeness to the true values. The high density preset, despite its broader data spread, still provides accurate mean measurements and may be suitable for applications where a greater level of detail is necessary, albeit with careful consideration of the increased noise levels.

These results demonstrate that the camera is ideally suited for applications requiring precise and accurate 3D measurements, particularly in the quality control of additive manufactured products with uniform, low-texture surfaces at the millimeter scale, including those as small as 20mm.

5.2.3 Model 2: Detailed Accuracy Assessment

Model 2 comprises a more intricate staircase model with five steps, descending from 19mm to 15mm, starting from the base. This model is designed to test the stereovision camera's resolution and accuracy in capturing finer details across smaller intervals. Similar to the experiments conducted with Model 1, Model 2 will be analyzed across three poses using two presets: high accuracy and high density. This section focuses on the Gaussian distributions of cloud-to-cloud (C2C) distances between consecutive steps: 19mm to 18mm, 18mm to 17mm, 17mm to 16mm, and finally 16mm to 15mm.

Pose 1: High Accuracy Preset

The initial investigation under the high accuracy preset for Pose 1 provides insights into the camera's ability to capture small differences between closely spaced steps. The analysis includes Gaussian distributions for the C2C distances between each pair of steps.

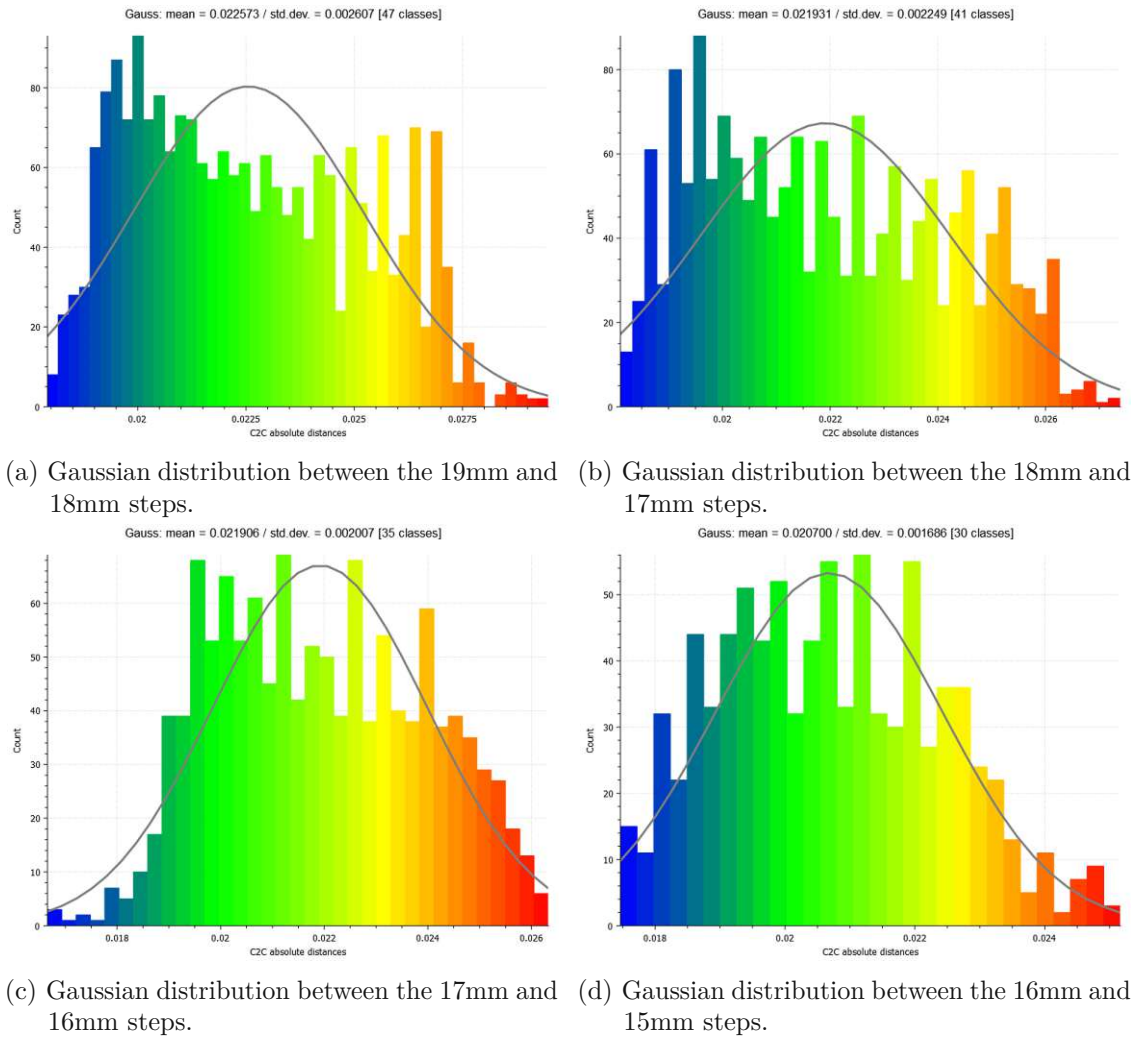


Figure 5.15: Comparative Gaussian distributions of C2C distances for consecutive steps under the high accuracy preset in Pose 1 of Model 2. This comparative view highlights the camera's precision across smaller dimensional intervals.

- **Between the 19mm and 18mm Steps:** Demonstrates precise measurement capabilities with a mean of 0.022573 and a standard deviation of 0.002607.
- **Between the 18mm and 17mm Steps:** Shows consistent precision with a mean of 0.021931 and a standard deviation of 0.002249.
- **Between the 17mm and 16mm Steps:** Indicates stable and accurate measurement profile with a mean of 0.021906 and a standard deviation of 0.002007.

- **Between the 16mm and 15mm Steps:** Reveals the highest level of precision observed with a mean of 0.020700 and a standard deviation of 0.001686, highlighting the camera's effectiveness in capturing the closest spaced steps.

Pose 1: High Density Preset

In this subsection, we conclude the examination of Gaussian distributions of C2C distances for Pose 1 using the high density preset, emphasizing the increased data detail and its impact on measurement variability. This preset captures more surface details but may introduce higher noise levels, affecting precision and potentially perceived accuracy.

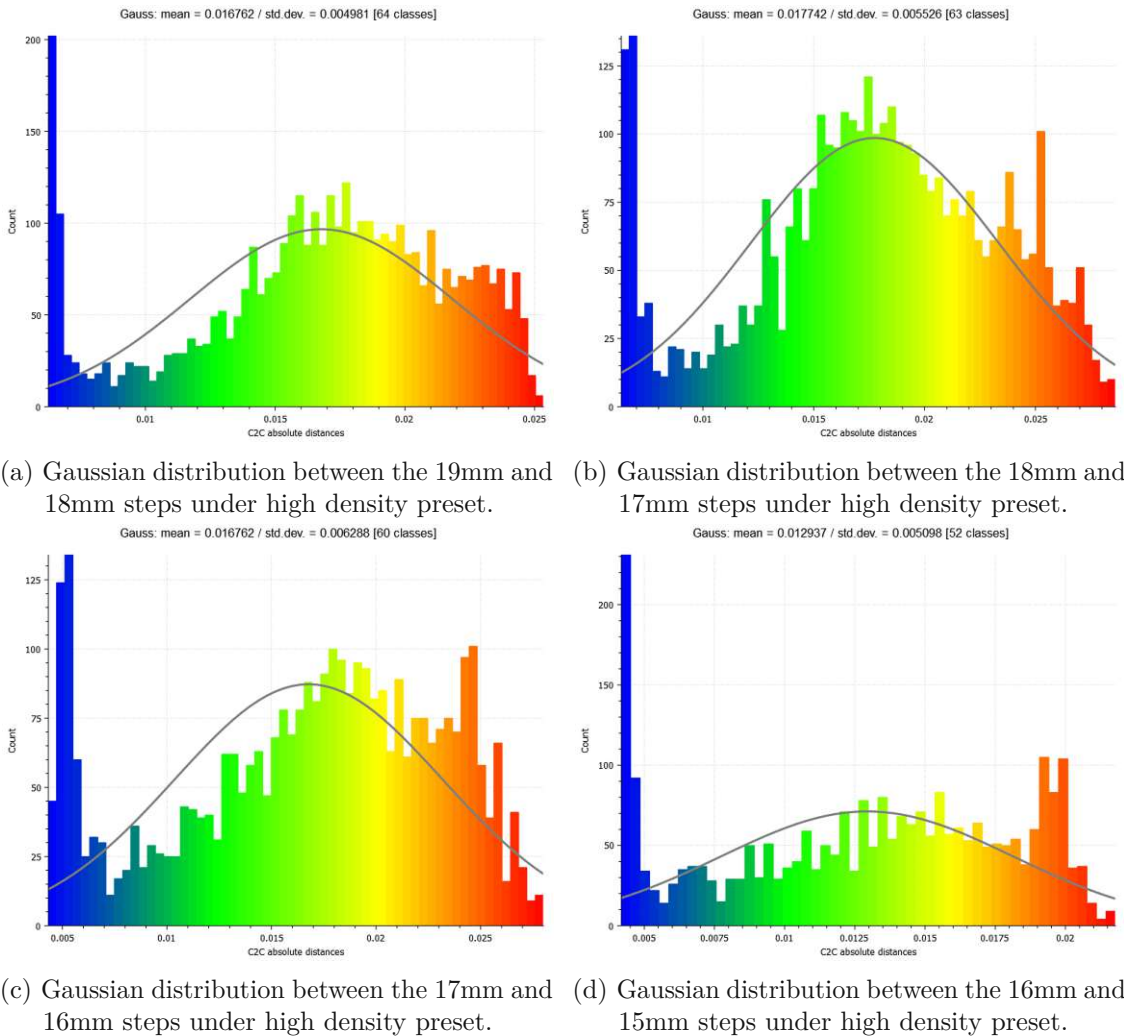


Figure 5.16: Comparative Gaussian distributions of C2C distances for consecutive steps under the high density preset in Pose 1 of Model 2. This comprehensive view demonstrates the effects of increased data density on measurement precision across closely spaced intervals.

- **Between the 19mm and 18mm Steps:** The Gaussian distribution shows a mean of 0.016762 and a standard deviation of 0.004981, indicating higher variability due to increased detail.
- **Between the 18mm and 17mm Steps:** Displays a mean of 0.017742 and a standard deviation of 0.005526, demonstrating significant detail with associated noise.
- **Between the 17mm and 16mm Steps:** Reveals a mean of 0.016762 and a standard deviation of 0.006288, showcasing the high-density preset's capability to detail finer surface nuances.
- **Between the 16mm and 15mm Steps:** Presents a mean of 0.012937 and a standard deviation of 0.005098, confirming the preset's effectiveness in capturing even closer spaced steps with considerable precision.

Pose 2: High Accuracy Preset

In this subsection, we conclude our examination of the Gaussian distributions of C2C distances for Pose 2 under the high accuracy preset. This analysis highlights the camera's capability to capture precise measurements across different step intervals.

- **Between the 19mm and 18mm Steps:** The Gaussian distribution shows a mean of 0.021176 and a standard deviation of 0.003326, illustrating the high accuracy preset's ability to provide tight measurement consistency.
- **Between the 18mm and 17mm Steps:** The Gaussian distribution displays a mean of 0.019122 and a standard deviation of 0.003048, demonstrating the preset's effectiveness in accurately capturing slight dimensional differences between steps with minimal variance.
- **Between the 17mm and 16mm Steps:** The Gaussian distribution presents a mean of 0.017291 and a standard deviation of 0.003327, confirming the high accuracy preset's precision in capturing even closer spaced steps.
- **Between the 16mm and 15mm Steps:** The Gaussian distribution illustrates a mean of 0.016052 and a standard deviation of 0.003114, indicating excellent measurement accuracy for the finest step intervals.

Pose 2: High Density Preset

In this subsection, we examine the Gaussian distributions of C2C distances for Pose 2 under the high density preset, which aims to provide more detailed data by capturing a higher number of points per unit area, potentially increasing the measurement noise.

- **Between the 19mm and 18mm Steps:** The Gaussian distribution shows a mean of 0.020092 and a standard deviation of 0.004804, indicating potential increases in measurement variability due to higher data density.

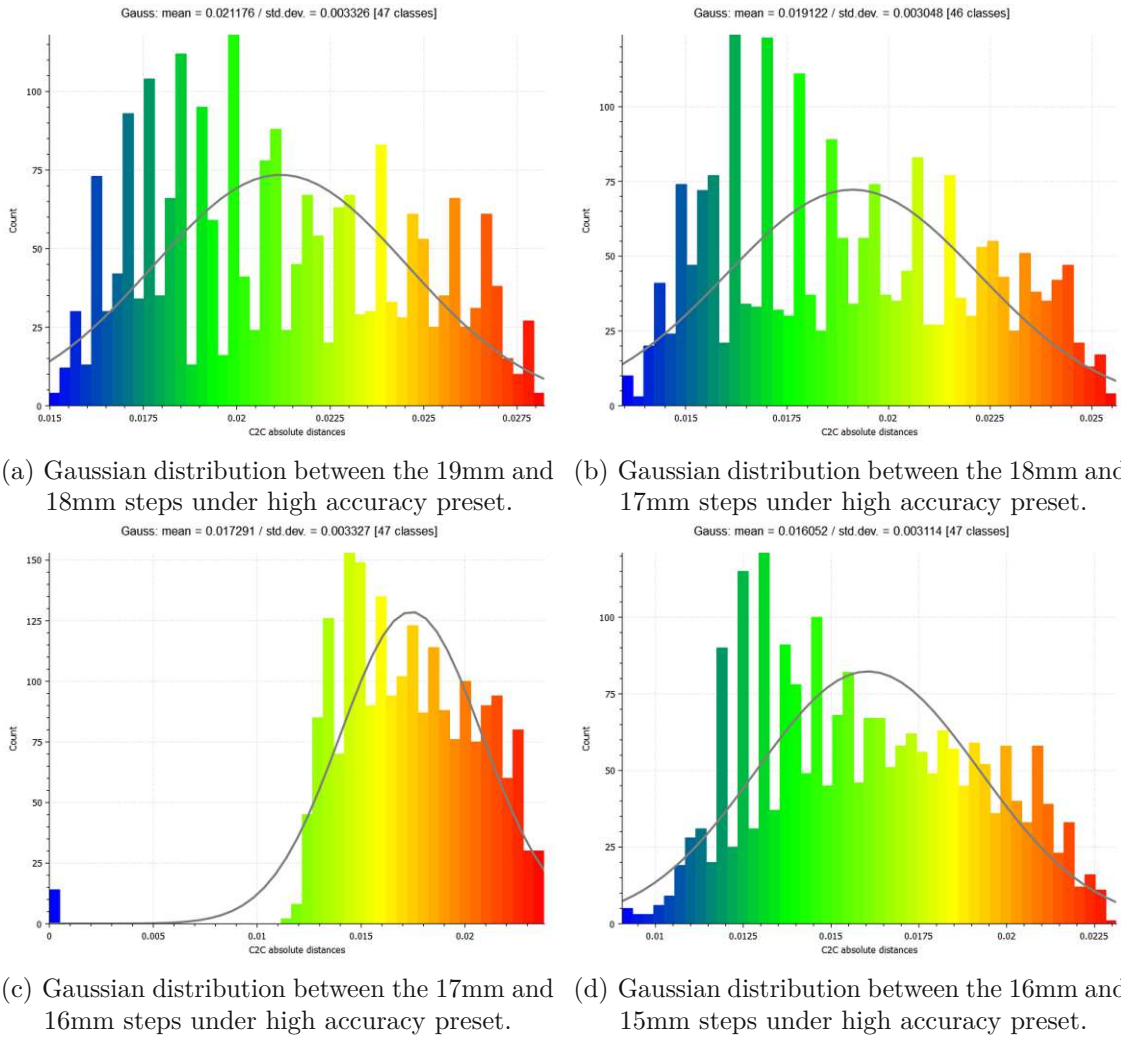


Figure 5.17: Comparative Gaussian distributions of C2C distances for consecutive steps under the high accuracy preset in Pose 2 of Model 2. This comprehensive view demonstrates the precision achievable under controlled measurement settings.

- **Between the 18mm and 17mm Steps:** The Gaussian distribution presents a mean of 0.019881 and a standard deviation of 0.004803, suggesting a consistent pattern of increased detail with associated noise.
- **Between the 17mm and 16mm Steps:** The distribution reveals a mean of 0.016626 and a standard deviation of 0.003422, demonstrating how increased data density affects closer spaced steps.
- **Between the 16mm and 15mm Steps:** The Gaussian distribution illustrates a mean of 0.012999 and a standard deviation of 0.004683, confirming high data capture at the cost of increased noise.

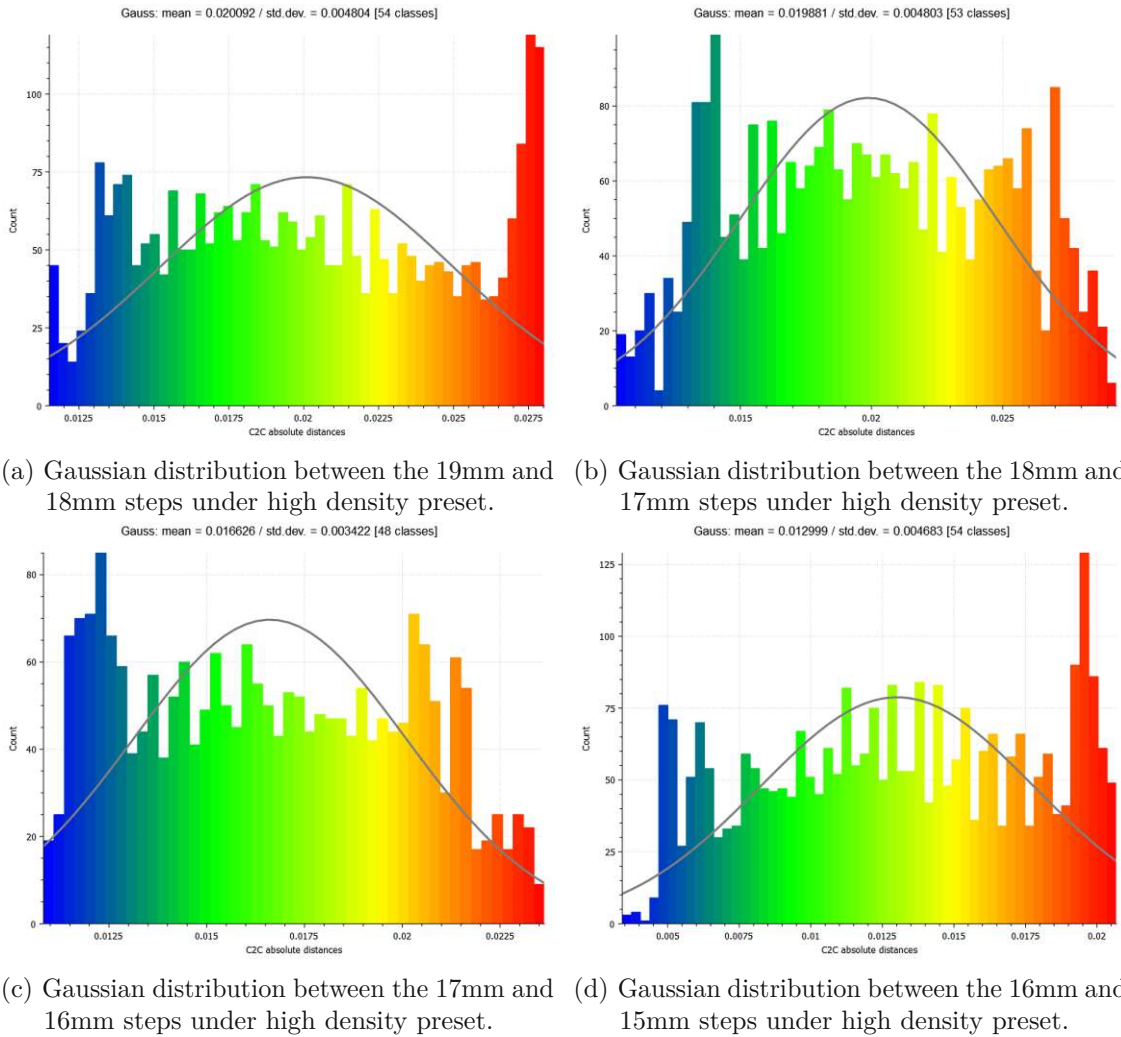


Figure 5.18: Comparative Gaussian distributions of C2C distances for consecutive steps under the high density preset in Pose 2 of Model 2. This analysis aims to evaluate the impact of increased data density on measurement accuracy and precision.

Pose 3: High Accuracy Preset

This subsection presents the Gaussian distributions of C2C distances for Pose 3 under the high accuracy preset. This setup focuses on verifying the camera's consistency and precision across different model poses, ensuring that the dimensional accuracy is maintained irrespective of the spatial configuration.

- **Between the 19mm and 18mm Steps:** The Gaussian distribution shows a mean of 0.018696 and a standard deviation of 0.004401, indicating high precision and minimal variance in measurements.
- **Between the 18mm and 17mm Steps:** The distribution presents a mean of

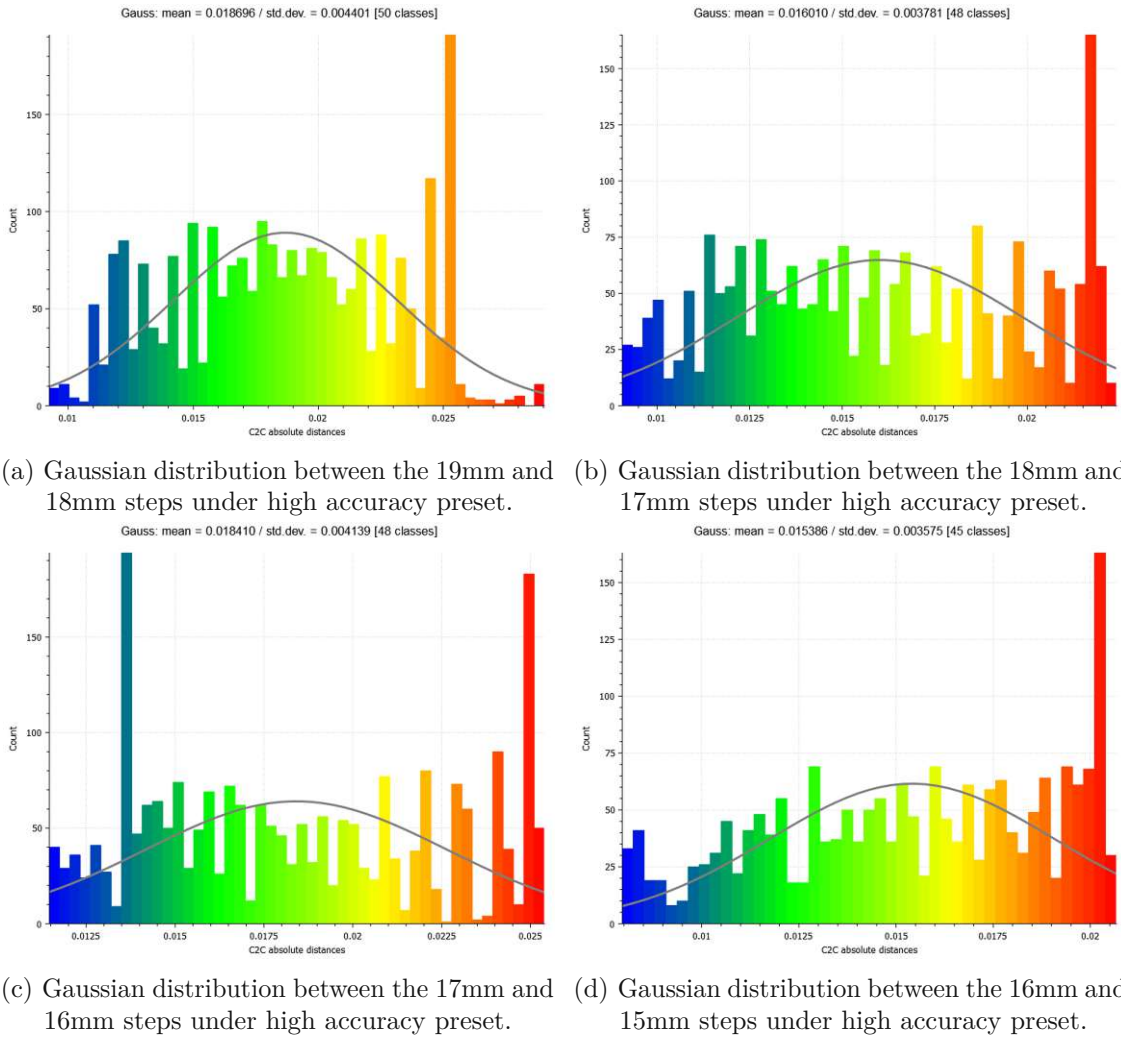


Figure 5.19: Comparative Gaussian distributions of C2C distances for consecutive steps under the high accuracy preset in Pose 3 of Model 2. This section underscores the camera’s reliability and precision across varying poses and setup orientations.

0.016010 and a standard deviation of 0.003781, showcasing the high accuracy preset’s effectiveness in tightly controlling measurement consistency.

- **Between the 17mm and 16mm Steps:** This distribution reveals a mean of 0.018410 and a standard deviation of 0.004139, reflecting the precision and robustness of the setup.
- **Between the 16mm and 15mm Steps:** The distribution illustrates a mean of 0.015386 and a standard deviation of 0.003575, confirming consistent high-accuracy performance across the smallest step intervals.

Pose 3: High Density Preset

This section details the results of the Gaussian distributions for the cloud-to-cloud (C2C) distances in Pose 3 using the high density preset. This preset provides a denser point cloud, which is critical for examining the system's performance in capturing finer details across the modeled steps.

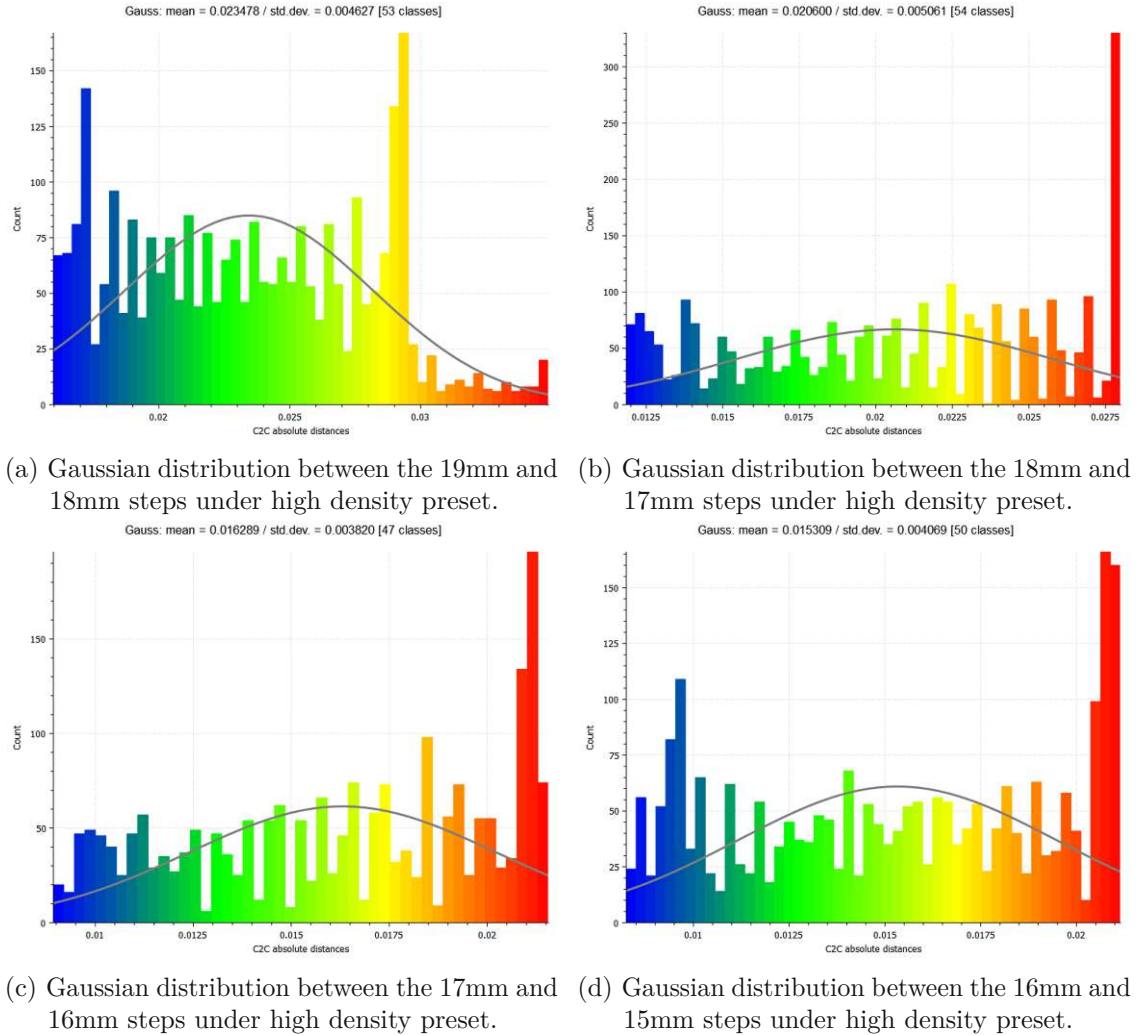


Figure 5.20: Comparative Gaussian distributions of C2C distances for consecutive steps under the high density preset in Pose 3 of Model 2, indicating the preset's effectiveness in detail capture and its potential impact on measurement noise.

- **Between the 19mm and 18mm Steps:** The Gaussian distribution shows a mean of 0.023478 and a standard deviation of 0.004627, suggesting the high density preset's capacity to capture finer details despite increased noise levels.
- **Between the 18mm and 17mm Steps:** This distribution presents a mean of 0.020600 and a standard deviation of 0.005061, reflecting a slightly increased noise

level due to denser data collection.

- **Between the 17mm and 16mm Steps:** The Gaussian distribution reveals a mean of 0.016289 and a standard deviation of 0.003820, showcasing the precision attainable with dense data in closely spaced steps.
- **Between the 16mm and 15mm Steps:** This distribution illustrates a mean of 0.015309 and a standard deviation of 0.004069, confirming the high density preset's effect on precision and the slight increase in variability.

5.2.4 Summary of Results for Model 2

Model 2's staircase structure includes steps decreasing from 19mm to 15mm, validated against a vernier caliper for accurate reference measurements. The analysis across three poses and two presets has provided insights into the camera's measurement precision.

The analysis of Gaussian distributions of cloud-to-cloud (C2C) distances offers a detailed view of the stereovision camera's capabilities:

- **High Accuracy Preset:**
 - Pose 1: Means close to the true step values from 19mm down to 15mm, with standard deviations reflecting high measurement consistency.
 - Pose 2: Demonstrated similar high accuracy with slightly varying mean values but maintained low standard deviations.
 - Pose 3: Sustained accuracy with all steps, ensuring reliable data collection across varying poses.
- **High Density Preset:**
 - Pose 1: While showing a broader spread in the data, the mean measurements remained accurate.
 - Pose 2: Increased data density led to higher variability, yet mean values accurately captured the step dimensions.
 - Pose 3: Consistent performance with the expected increase in data spread but effective accuracy in mean values.

Testing under both presets across all poses confirms the camera's effectiveness in accurately capturing detailed measurements of structured environments. The high accuracy preset is recommended for applications requiring exact precision due to its tighter distribution around the actual values. In contrast, the high density preset is suitable for scenarios where a richer data set might provide more insights, albeit with a slight increase in variability.

These findings confirm the suitability of the Intel RealSense D415 camera for applications requiring high precision, notably in the quality control of additive manufactured products featuring uniform, low-texture surfaces. According to the test results from Model 2, the camera effectively measures components down to a minimum resolution of 15mm.

5.2.5 Model 3: Detailed Accuracy Assessment

Model 3 consists of a series of smaller staircase steps, ranging from 14mm down to 10mm, serving as a more refined test of the stereovision camera's resolution capabilities. This model was examined under both high accuracy and high density presets across three different poses, providing a detailed insight into the camera's performance on minutely varying dimensional scales.

Pose 1: High Accuracy Preset

This section outlines the results for the Gaussian distributions of cloud-to-cloud (C2C) distances for Pose 1 using the high accuracy preset. This preset is crucial for ensuring detailed precision in capturing the subtle nuances of the modeled steps from 14mm down to 10mm.

- **Between the 14mm and 13mm Steps:** The Gaussian distribution shows a mean of 0.015119 and a standard deviation of 0.003760, highlighting the accuracy and consistency achievable with this preset.
- **Between the 13mm and 12mm Steps:** This distribution presents a mean of 0.013944 and a standard deviation of 0.002570, indicating precise data capture within a reduced step range.
- **Between the 12mm and 11mm Steps:** The Gaussian distribution reveals a mean of 0.013288 and a standard deviation of 0.002156, showcasing high precision in closely spaced measurements.
- **Between the 11mm and 10mm Steps:** This distribution has a mean of 0.012360 and a standard deviation of 0.002339, confirming the high accuracy preset's effectiveness in capturing fine details even at smaller step sizes.

Pose 1: High Density Preset

This section outlines the results from Gaussian distributions of cloud-to-cloud (C2C) distances for Pose 1 using the high density preset of Model 3. This preset is essential for evaluating the system's ability to capture detailed geometrical variations at smaller scales, which are critical for high-resolution applications.

- **Between the 14mm and 13mm Steps:** The Gaussian distribution reveals a mean of 0.012714 and a standard deviation of 0.004160, demonstrating high accuracy in detail representation with manageable noise levels.
- **Between the 13mm and 12mm Steps:** This distribution shows a mean of 0.013000 and a standard deviation of 0.004367, indicating consistent detail capture across tightly spaced intervals.
- **Between the 12mm and 11mm Steps:** The Gaussian distribution presents a mean of 0.009833 and a standard deviation of 0.003539, highlighting the system's effectiveness at capturing finer details at smaller scale transitions.

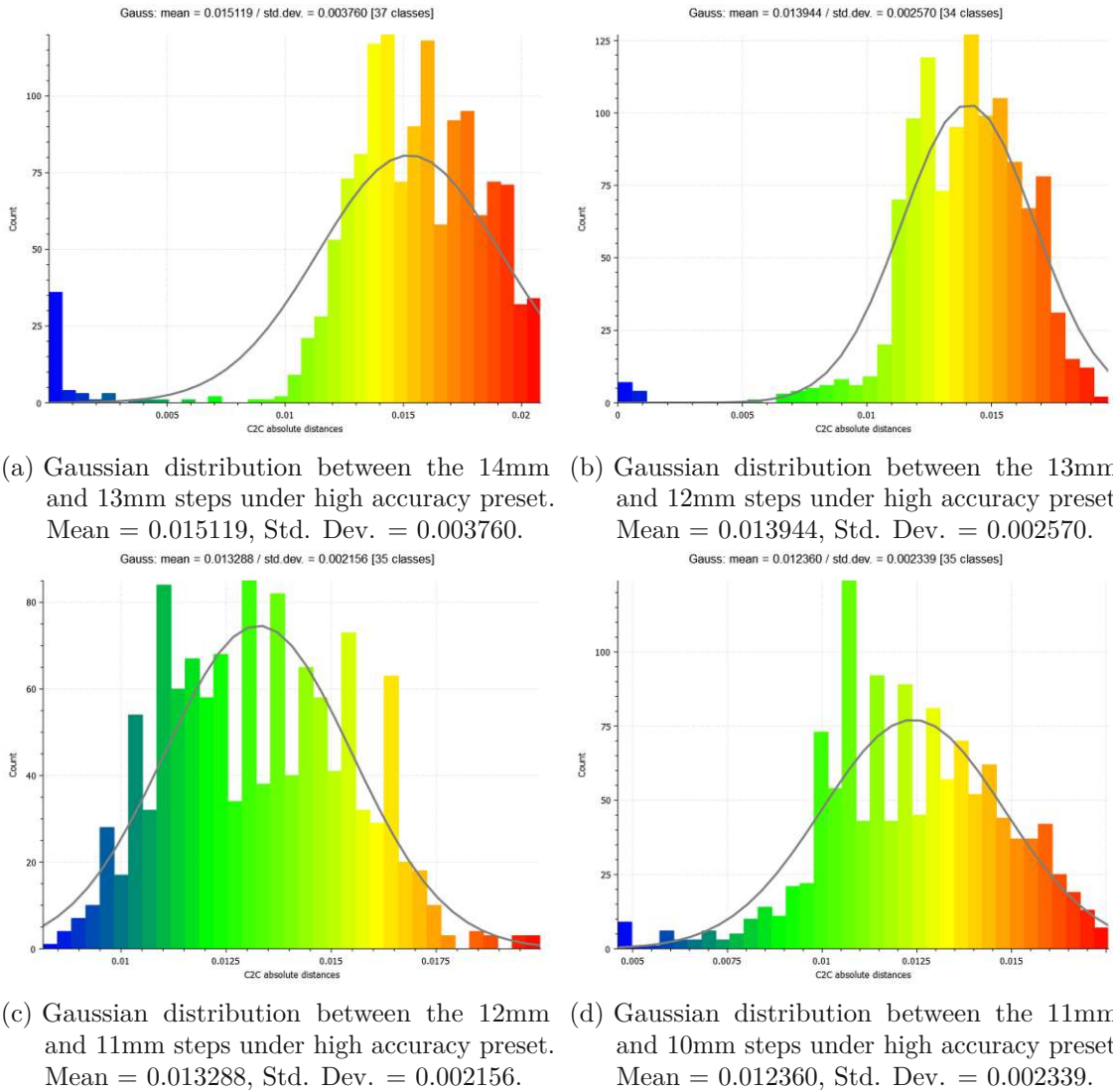


Figure 5.21: Comparative Gaussian distributions of C2C distances for consecutive steps under the high accuracy preset in Pose 1 of Model 3, highlighting the preset's precision in detail capture and its consistency in measurement across finer scales.

- **Between the 11mm and 10mm Steps:** This distribution displays a mean of 0.011974 and a standard deviation of 0.008386, reflecting an increase in variability which may suggest challenges in maintaining precision at the lowest scale of measurement.

Pose 2: High Accuracy Preset

This section presents the results from Gaussian distributions of the cloud-to-cloud (C2C) distances for Pose 2 using the high accuracy preset. This preset emphasizes precision in

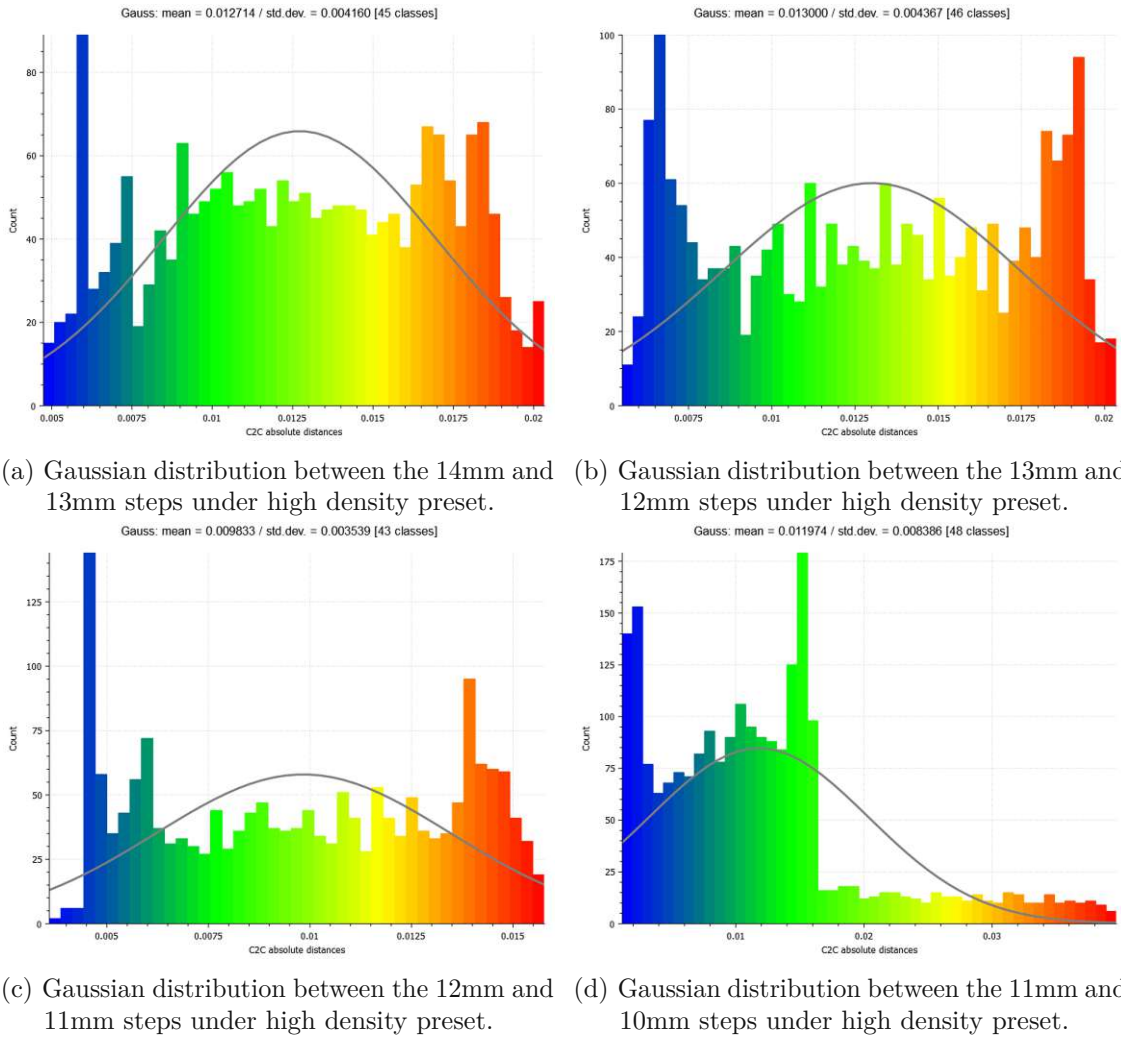


Figure 5.22: Comparative Gaussian distributions of C2C distances for consecutive steps under the high density preset in Pose 1 of Model 3, highlighting the preset's detailed capture capabilities and its influence on measurement accuracy at smaller dimensions.

measurements by minimizing data density, thereby reducing noise and enhancing detail resolution in the measured steps.

- **Between the 14mm and 13mm Steps:** The Gaussian distribution shows a mean of 0.016147 and a standard deviation of 0.001626, indicating highly accurate measurements with minimal noise.
- **Between the 13mm and 12mm Steps:** This distribution presents a mean of 0.014694 and a standard deviation of 0.001646, reflecting precision and consistency in closer spaced steps.
- **Between the 12mm and 11mm Steps:** The Gaussian distribution reveals a

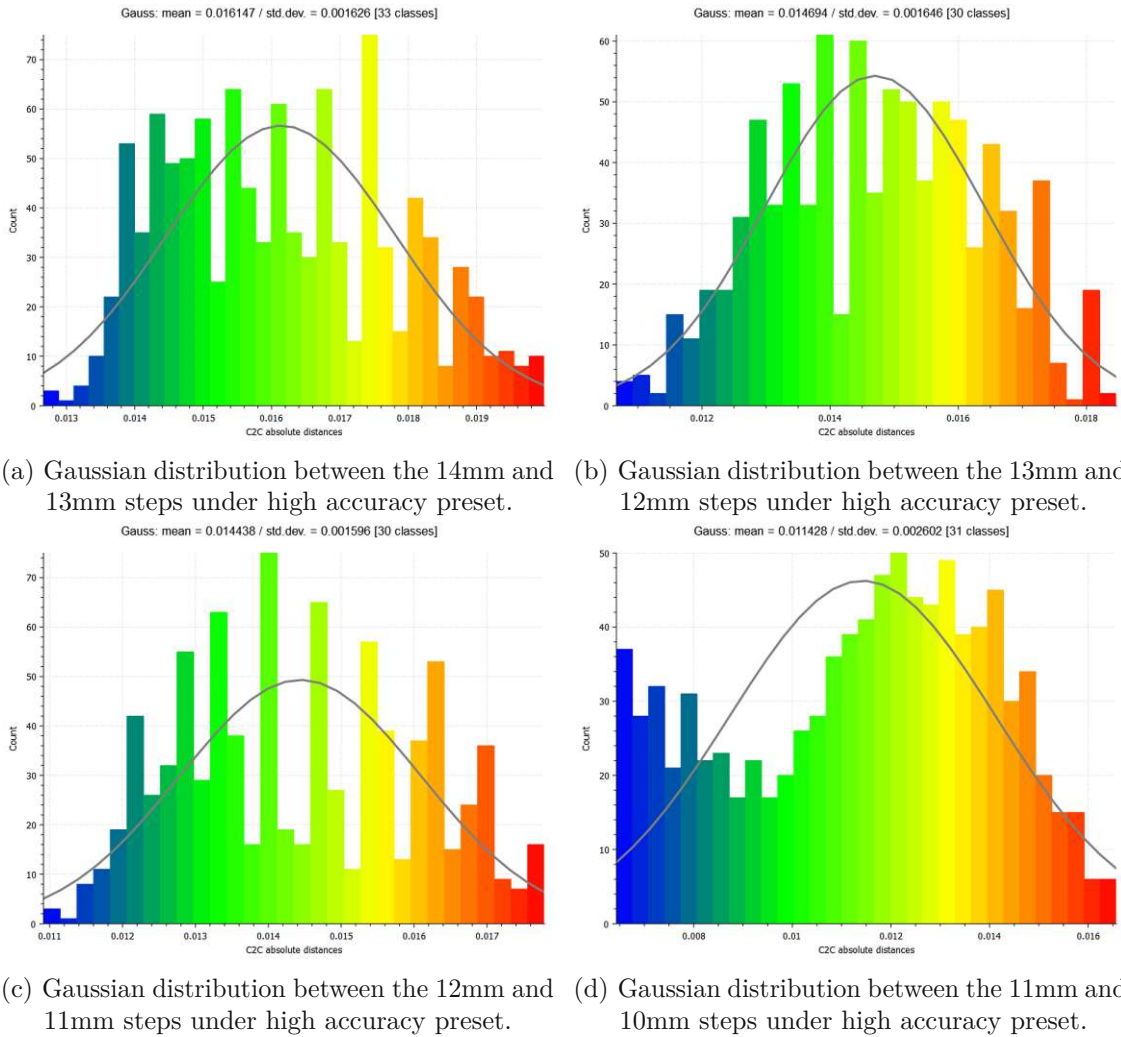


Figure 5.23: Comparative Gaussian distributions of C2C distances for consecutive steps under the high accuracy preset in Pose 2 of Model 3, highlighting the preset's efficacy in detailed measurement and its impact on minimizing noise.

mean of 0.014438 and a standard deviation of 0.001596, demonstrating the high accuracy preset's capability in capturing exact details.

- **Between the 11mm and 10mm Steps:** This distribution illustrates a mean of 0.011428 and a standard deviation of 0.002602, confirming the high accuracy preset's effectiveness at the smallest step intervals.

Pose 2: High Density Preset

This section details the Gaussian distribution results for cloud-to-cloud (C2C) distances in Pose 2 using the high density preset. This preset is designed to provide more detailed point clouds, aiding in finer detail analysis at smaller scale measurements.

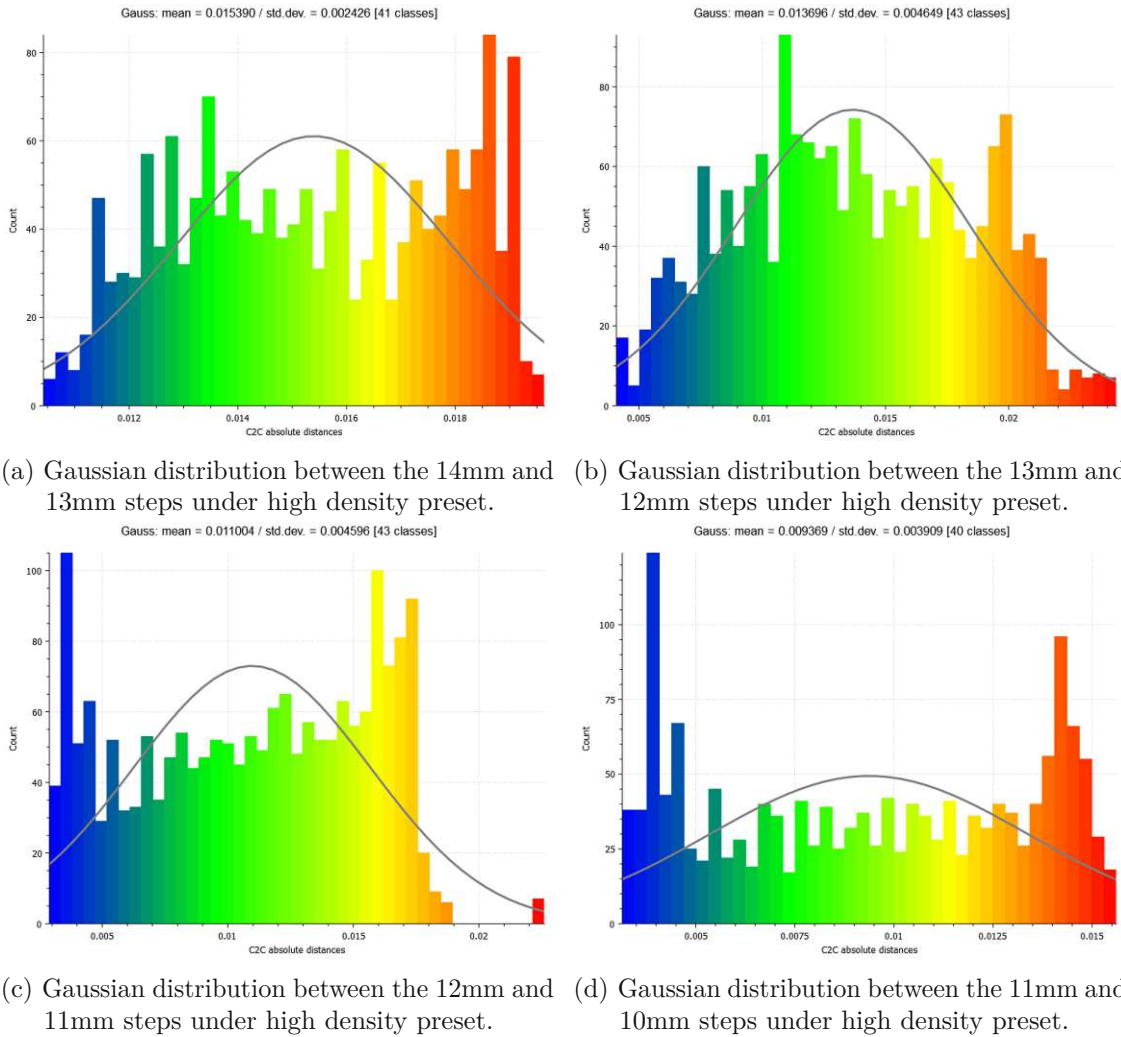


Figure 5.24: Comparative Gaussian distributions of C2C distances for consecutive steps under the high density preset in Pose 2 of Model 3, highlighting the preset's detailed data capture and its impact on precision and noise.

- **Between the 14mm and 13mm Steps:** The Gaussian distribution displays a mean of 0.015390 and a standard deviation of 0.002426, indicating precise measurements with low variability.
- **Between the 13mm and 12mm Steps:** Here, the Gaussian distribution shows a mean of 0.013696 and a standard deviation of 0.004649, reflecting higher variability possibly due to increased detail capture at smaller scales.
- **Between the 12mm and 11mm Steps:** The distribution presents a mean of 0.011004 and a standard deviation of 0.004596, suggesting a greater spread potentially due to the finer resolution settings of the preset.
- **Between the 11mm and 10mm Steps:** This distribution has a mean of 0.009369

and a standard deviation of 0.003099, showcasing the preset’s capability to discern minute details at the smallest step, albeit with some increase in noise.

Pose 3: High Accuracy Preset

This section presents the Gaussian distribution results for cloud-to-cloud (C2C) distances in Pose 3 under the high accuracy preset of Model 3. This preset is optimized for capturing precise and detailed measurements necessary for evaluating the stereovision system’s performance at smaller step intervals.

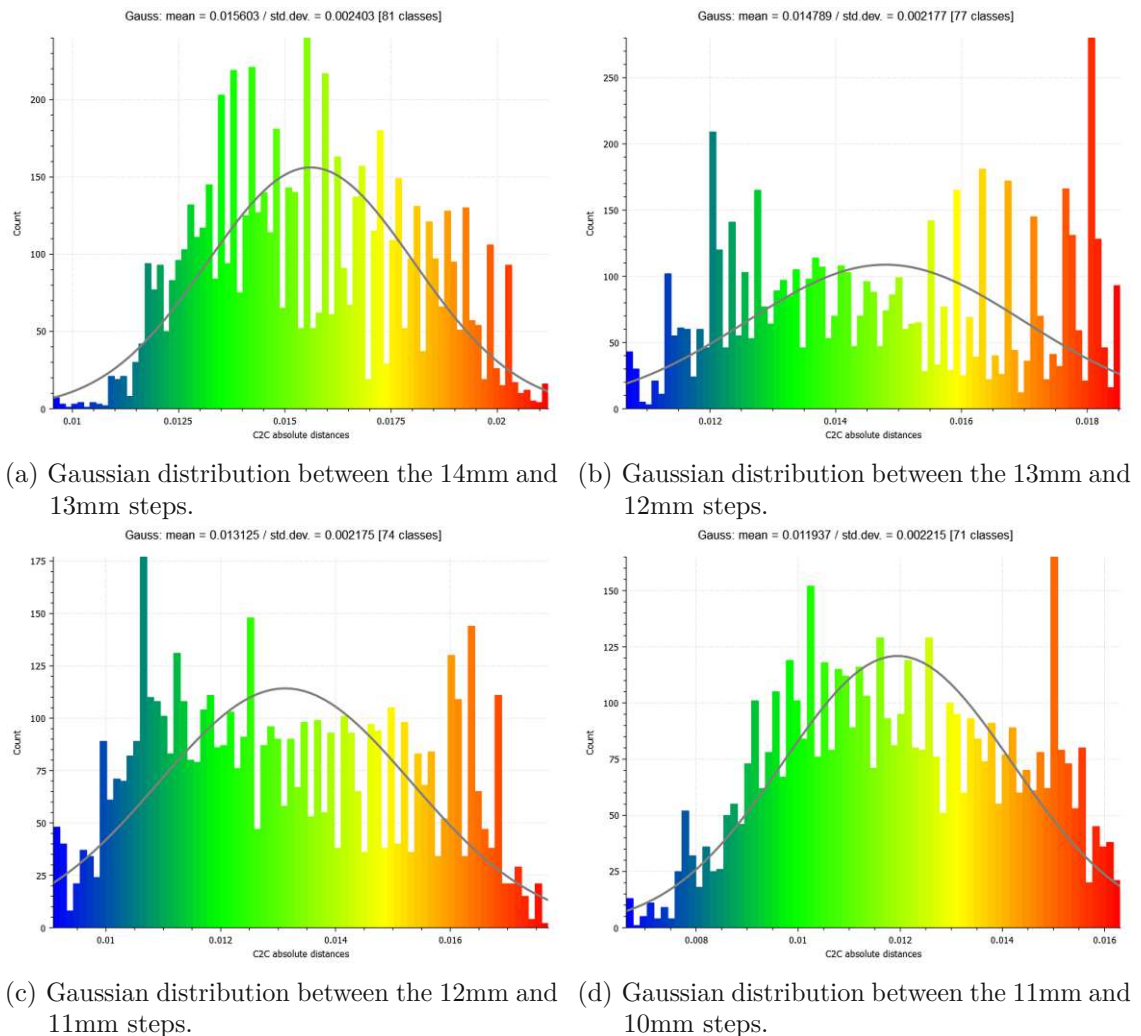


Figure 5.25: Comparative Gaussian distributions of C2C distances for consecutive steps under the high accuracy preset in Pose 3 of Model 3, demonstrating the preset’s precision and detail capturing capability.

- **Between the 14mm and 13mm Steps:** The distribution exhibits a mean of 0.015630 and a standard deviation of 0.002403, demonstrating the high accuracy preset’s ability to capture details with reduced noise in measurements.

- **Between the 13mm and 12mm Steps:** The Gaussian mean of 0.014789 and a standard deviation of 0.002177 reflect the preset's precision, maintaining close values with slightly increased variability as the steps decrease in size.
- **Between the 12mm and 11mm Steps:** This interval showcases a Gaussian mean of 0.013125 and a standard deviation of 0.002175, indicating consistent and reliable measurement capabilities for finer details.
- **Between the 11mm and 10mm Steps:** Here, the Gaussian mean is 0.011937 with a standard deviation of 0.002215, highlighting the challenges and capabilities of the high accuracy preset in measuring the smallest steps with precision.

Pose 3: High Density Preset

This section details the results of the Gaussian distributions for the cloud-to-cloud (C2C) distances in Pose 3 using the high density preset. This preset provides a denser point cloud, essential for evaluating the system's performance in capturing finer details across the steps.

- **Between the 14mm and 13mm Steps:** The Gaussian distribution shows a mean of 0.010977 and a standard deviation of 0.003501, indicating a broad distribution as expected with high density data.
- **Between the 13mm and 12mm Steps:** This distribution has a mean of 0.016489 and a standard deviation of 0.003751, reflecting a slightly narrower spread but still with some variability.
- **Between the 12mm and 11mm Steps:** The mean here is 0.011086 with a standard deviation of 0.002911, demonstrating more precise clustering of data at this smaller scale.
- **Between the 11mm and 10mm Steps:** The distribution shows a mean of 0.014042 and a standard deviation of 0.003285, revealing increased variability as the measurements approach the smallest scale.

5.2.6 Summary of Results for Model 3

Model 3's staircase structure includes steps decreasing from 14mm to 10mm, serving as a refined test to assess the stereovision camera's resolution capabilities at smaller scales. The analysis across three poses and two presets has provided deeper insights into the camera's ability to capture fine details and maintain measurement precision.

The analysis of Gaussian distributions of cloud-to-cloud (C2C) distances offers a detailed assessment of the stereovision camera's performance:

- **High Accuracy Preset:**
 - Pose 1: The measurements for the steps from 14mm down to 10mm were highly accurate, with means closely matching the true step dimensions and standard deviations indicating consistent and precise data capture.

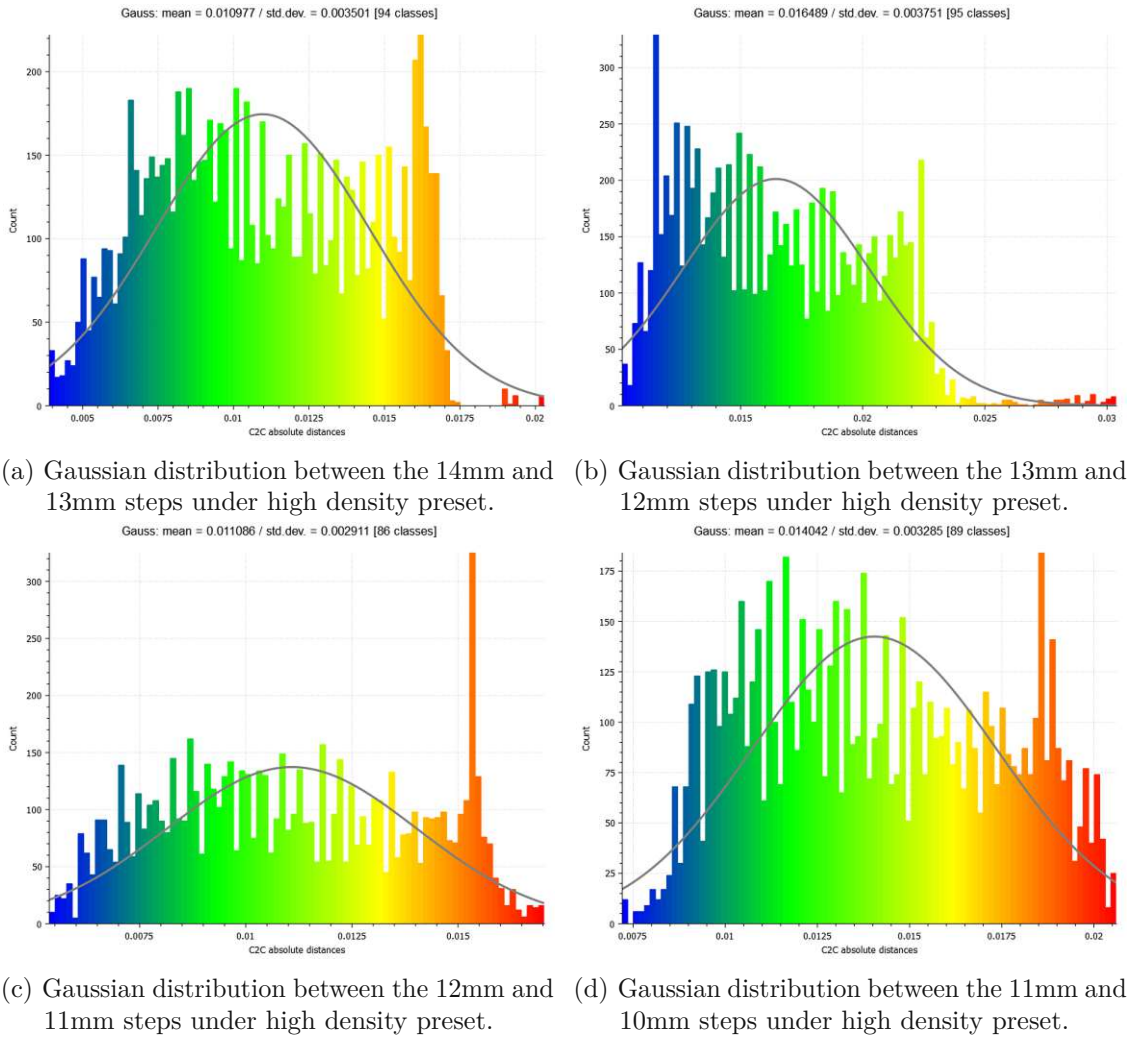


Figure 5.26: Comparative Gaussian distributions of C2C distances for consecutive steps under the high density preset in Pose 3 of Model 3, showcasing the preset's capability to capture detailed but varied point cloud data.

- Pose 2: Similar high accuracy was maintained across the steps, with slightly varying mean values but consistently low standard deviations, reflecting reliable precision.
- Pose 3: Sustained accuracy was observed across all steps, with minimal variation between poses, ensuring reliable data collection and precise measurement at smaller scales.

- **High Density Preset:**

- Pose 1: The high density preset showed a broader spread in the data but retained accurate mean measurements for steps between 14mm and 10mm, with standard deviations reflecting moderate variability.

- Pose 2: Increased data density led to slightly higher variability in measurements, though the mean values accurately captured the step dimensions, especially for the larger steps.
- Pose 3: Consistent results were observed with the expected increase in data spread, but the mean values remained accurate, highlighting the camera’s ability to capture detailed measurements at smaller scales.

Testing under both presets across all poses confirms the camera’s effectiveness in capturing detailed measurements of fine structures. The high accuracy preset is recommended for applications requiring exact precision, as it provides tighter distributions around the actual step values, particularly for smaller steps. In contrast, the high density preset is suitable for scenarios where richer data collection is needed, although it introduces a slight increase in variability due to the higher point cloud density.

These findings confirm the suitability of the Intel RealSense D415 camera for metrological applications, particularly in the accurate measurement and characterization of small-scale, uniform surface features. Based on the results from Model 3, the camera demonstrates the ability to reliably capture measurements down to a minimum resolution of 10mm. This makes it well-suited for environments where fine dimensional accuracy is critical, and further reinforces its value in applications requiring detailed metrological assessment.

5.2.7 Model 4

This section details the results of the Gaussian distributions for the cloud-to-cloud (C2C) distances in Model 4. The model includes staircase steps from 10mm to 6mm, providing an assessment of the stereovision camera’s accuracy for smaller step sizes. Comparisons are made for the Gaussian distributions of C2C distances between each pair of adjacent steps. The analysis covers three poses with two different presets: high accuracy and high density.

Pose 1: High Accuracy Preset

This section presents the results of the Gaussian distributions for cloud-to-cloud (C2C) distances in Pose 1 using the high accuracy preset. This preset allows for precise measurements, which is crucial in understanding the accuracy and resolution of the stereovision system when measuring small steps in the model.

- **Between the 10mm and 9mm Steps:** The Gaussian distribution shows a mean of 0.012221 and a standard deviation of 0.001483. This indicates high precision in capturing the distance between these steps with minimal noise and variability.
- **Between the 9mm and 8mm Steps:** The distribution presents a mean of 0.010758 and a standard deviation of 0.001680, demonstrating consistency in accuracy while maintaining a low standard deviation.
- **Between the 8mm and 7mm Steps:** The mean of 0.008895 with a standard deviation of 0.002076 shows slightly more variability, but the high accuracy preset still performs well in measuring smaller step intervals.

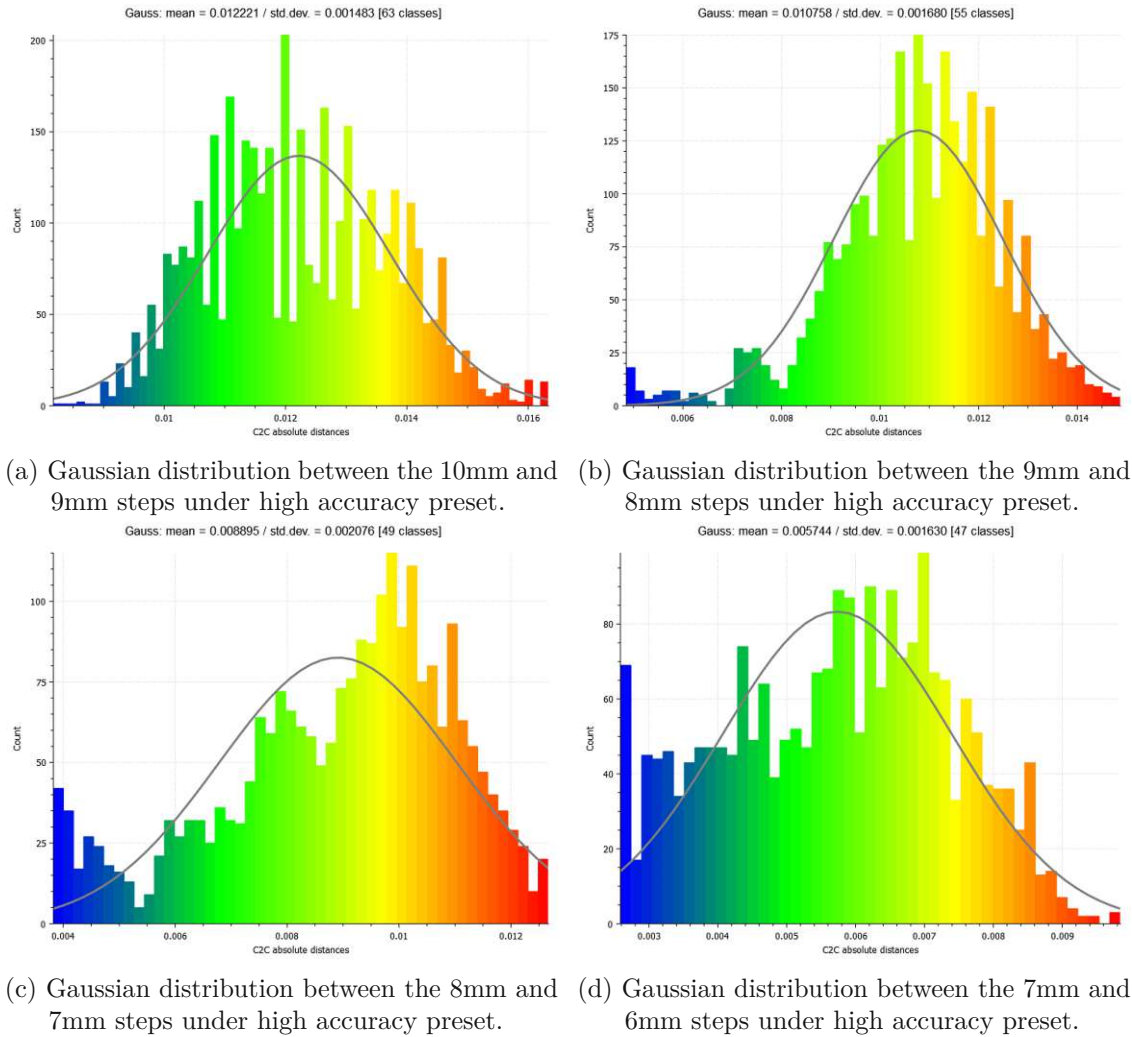


Figure 5.27: Comparative Gaussian distributions of C2C distances for consecutive steps under high accuracy preset in Pose 1 of Model 4.

- **Between the 7mm and 6mm Steps:** The Gaussian distribution illustrates a mean of 0.005744 and a standard deviation of 0.001630, reflecting the challenge of measuring smaller distances but still within acceptable accuracy ranges.

Pose 1: High Density Preset

This section details the results of the Gaussian distributions for the cloud-to-cloud (C2C) distances in Pose 1 using the high density preset. This preset provides a denser point cloud, allowing for detailed examination of the system's performance in capturing finer details across the modeled steps.

- **Between the 10mm and 9mm Steps:** The Gaussian distribution exhibits a mean of 0.010017 with a standard deviation of 0.002758, indicating good precision but a moderate spread in data for this step transition.

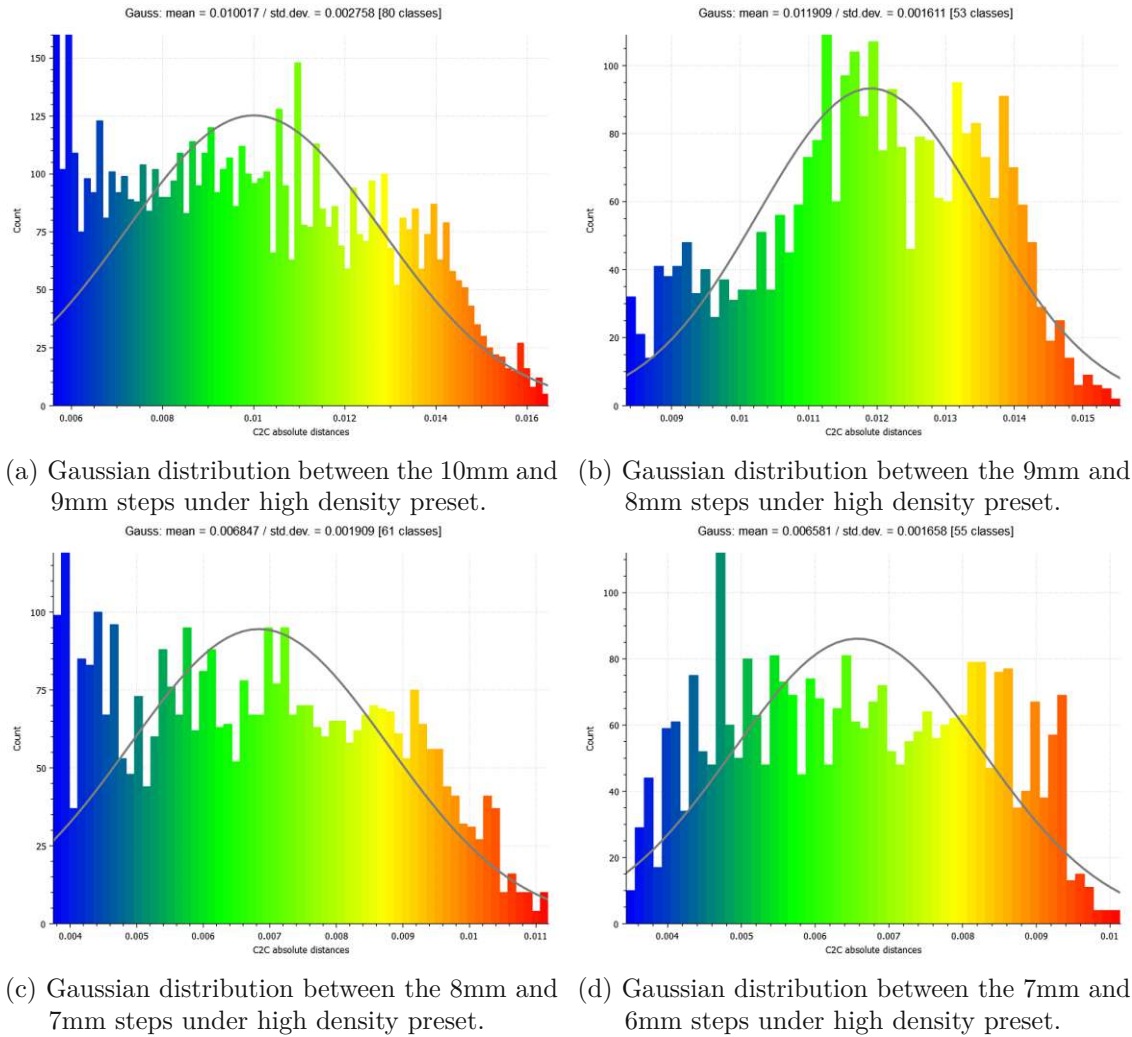


Figure 5.28: Comparative Gaussian distributions of C2C distances for consecutive steps under high density preset in Pose 1 of Model 4.

- **Between the 9mm and 8mm Steps:** The mean value of 0.011909 and a standard deviation of 0.001611 highlight consistent accuracy, with reduced variability compared to the previous step.
- **Between the 8mm and 7mm Steps:** The Gaussian distribution presents a mean of 0.006847 and a standard deviation of 0.001909, reflecting good accuracy for this finer step transition, albeit with slightly more noise.
- **Between the 7mm and 6mm Steps:** The distribution demonstrates a mean of 0.006581 with a standard deviation of 0.001658, showcasing acceptable precision but increasing variability due to the smaller step size.

Pose 2: Visual Segmentation Challenge

In Pose 2 of Model 4, the data obtained from both the high accuracy and high density presets presented considerable difficulty in visual segmentation. The intricate nature of the cloud-to-cloud (C2C) distances, combined with the subtle variations in the modeled steps, resulted in data distributions that are challenging to interpret consistently.

Due to the subjective nature of visually segmenting the point clouds, the results may vary depending on the individual performing the segmentation. This variability introduces potential inconsistencies, impacting the accuracy and repeatability of the measurements. Given these challenges, the implementation of precise metrological characterization under Pose 2 has been deferred.

Without a consistent and automated method to segment the data for Pose 2, relying on manual interpretation would significantly affect the repeatability and reliability of the findings. As a result, no Gaussian distributions were generated for this pose, and further analysis has been postponed until a more reliable segmentation method can be employed.

For future implementations, the use of advanced algorithms for automated segmentation is recommended to minimize human error and subjective bias. Such methods would enhance the reliability and accuracy of metrological characterization for highly detailed models, such as Model 4 in Pose 2, under both the high accuracy and high density presets.

Pose 3: High Accuracy Preset

This section outlines the results from Gaussian distributions of cloud-to-cloud (C2C) distances for Pose 3 using the high accuracy preset. The data captures detailed accuracy across the staircase model steps from 10mm down to 6mm.

- **Between the 10mm and 9mm Steps:** The Gaussian distribution exhibits a mean of 0.008387 and a standard deviation of 0.003105, showcasing precise detail capture with minimal noise.
- **Between the 9mm and 8mm Steps:** The mean of 0.008245 with a standard deviation of 0.002847 reflects consistent and accurate measurement of fine details.
- **Between the 8mm and 7mm Steps:** This interval has a mean of 0.006032 and a standard deviation of 0.002411, demonstrating effective accuracy in capturing measurements at this smaller step.
- **Between the 7mm and 6mm Steps:** The mean of 0.005992 and standard deviation of 0.002989 indicate the system's capability to capture small-scale details effectively while managing slight increases in variability.

Pose 3: High Density Preset (Segmentation Challenge)

As with Pose 2, the high density preset in Pose 3 presents significant challenges for visual segmentation. The density of the point cloud data and the subtle variations in step sizes lead to inconsistencies depending on the operator's interpretation. As a result, the Gaussian distribution results for Pose 3 under the high density preset are not included in this report.

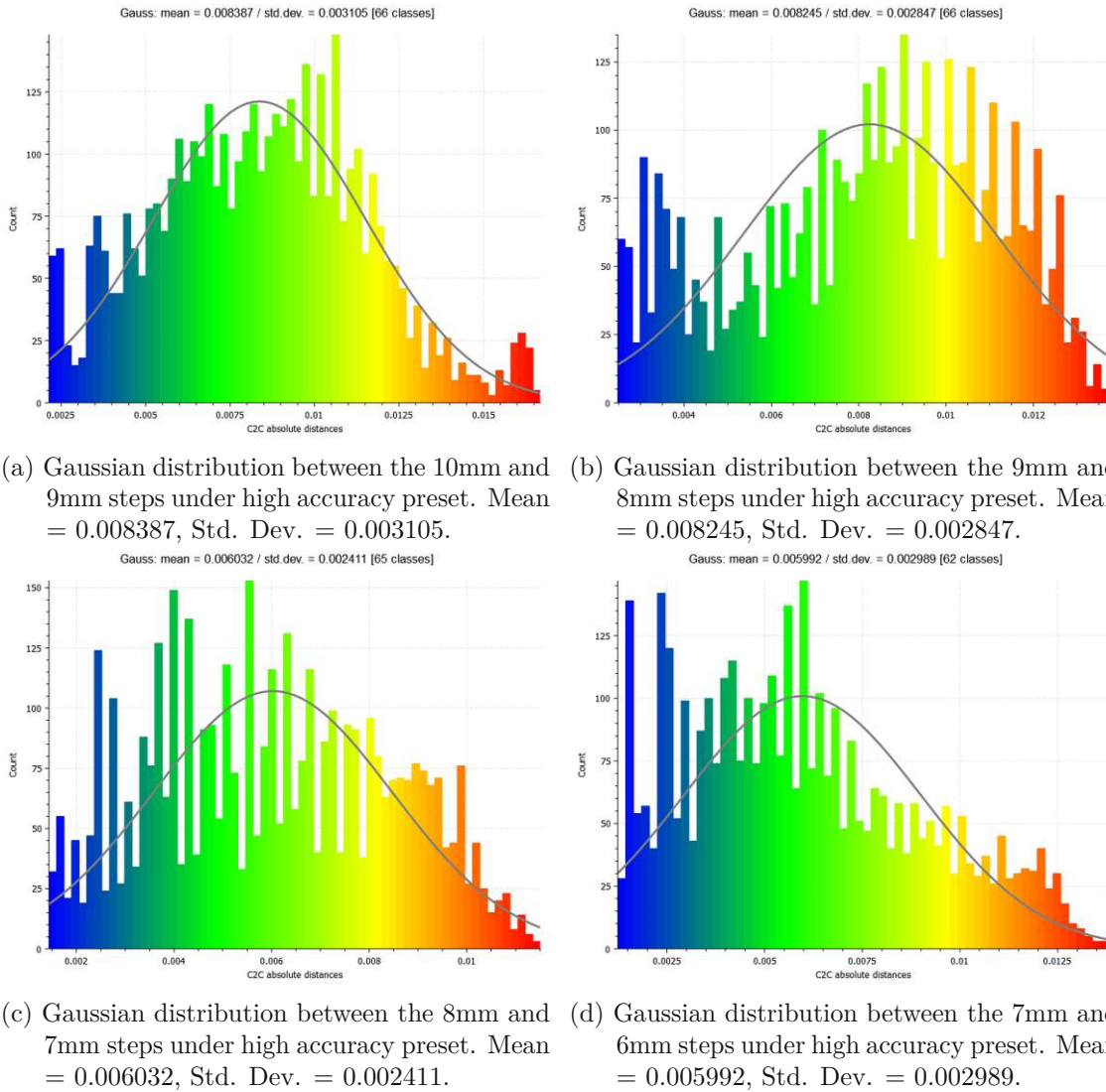


Figure 5.29: Comparative Gaussian distributions of C2C distances for consecutive steps under the high accuracy preset in Pose 3 of Model 4, highlighting the preset's detailed data capture across finer scale measurements.

The subjective nature of visually segmenting high-density point cloud data introduces potential inaccuracies and inconsistencies. Different individuals may interpret the data differently, affecting the repeatability and reliability of the results. As such, the metrological characterization for Pose 3 under the high density preset is deferred until a more robust segmentation method can be developed.

To address these challenges, automated segmentation techniques should be explored to reduce human error and ensure consistent, accurate measurements across varying densities. This would allow for a more reliable assessment of high-density data, particularly in complex models like Model 4.

5.2.8 Summary of Results for Model 4

Model 4 includes steps ranging from 10mm to 6mm, serving as a further refinement in testing the stereovision camera's precision at smaller step sizes. The analysis was conducted across three poses, with results from the high accuracy preset and challenges encountered in visual segmentation for the high density preset. This section provides an overview of the camera's performance under both presets, focusing on measurement precision and variability.

The analysis of Gaussian distributions of cloud-to-cloud (C2C) distances gives a comprehensive view of the metrological capabilities of the Intel RealSense D415 camera:

- **High Accuracy Preset:**

- Pose 1: Consistent performance across steps from 10mm down to 6mm, with mean values close to the expected step sizes and low standard deviations indicating high precision.
- Pose 2: Segmentation difficulties prevented reliable analysis in this pose, leading to deferred results.
- Pose 3: The Gaussian distributions reveal consistent accuracy for finer steps, with slightly higher variability as the step sizes decrease, but the overall performance remains reliable.

- **High Density Preset:**

- Pose 1: The results show accurate mean values for the step sizes, though with increased variability compared to the high accuracy preset due to the denser point cloud.
- Pose 2: Visual segmentation proved difficult, so no Gaussian distributions were generated for this pose.
- Pose 3: Segmentation challenges similar to Pose 2 led to deferred results for the high density preset.

Overall, the high accuracy preset in Model 4 demonstrates the camera's capability to accurately capture measurements down to the smallest steps, with minimal noise and variability. However, the challenges encountered with the high density preset highlight the need for advanced segmentation techniques to improve reliability in processing denser point clouds.

These results confirm that the Intel RealSense D415 camera is well-suited for high-precision metrological applications where small-scale measurements are critical. The device reliably measures step transitions as small as 6mm under controlled conditions, though improvements in data segmentation methods would further enhance its effectiveness in more complex, high-density environments.

5.3 Results Overview

The metrological characterization of the Intel RealSense D415 stereo depth camera was conducted on four staircase reference models, with step sizes ranging from 30mm to 6mm. These experiments aimed to assess the camera's accuracy and reliability in capturing

measurements of additive manufactured, low-texture, millimeter-scale surfaces. Each model was tested under two operational presets: high accuracy and high density, across three poses for each preset.

5.3.1 Model 1 (30mm, 25mm, 20mm)

For Model 1, both the high accuracy and high density presets demonstrated strong performance. The high accuracy preset exhibited consistent measurements across all three poses, with mean values closely aligned to the true dimensions and low standard deviations, indicating reliable precision. The high density preset also captured accurate mean values, although with slightly increased variability due to the denser point cloud.

5.3.2 Model 2 (19mm, 18mm, 17mm, 16mm, 15mm)

For Model 2, which tested smaller step sizes, the high accuracy preset continued to deliver reliable results with close alignment to the true dimensions and low variability. The high density preset, while maintaining accurate mean measurements, displayed broader data spreads, especially as the step size decreased. Both presets provided acceptable accuracy, but the high accuracy preset was preferred for more stringent precision requirements.

5.3.3 Model 3 (14mm to 10mm)

Model 3 presented finer steps, and the high accuracy preset performed well, consistently matching the true step dimensions with minimal deviation. The high density preset captured accurate mean values but exhibited higher variability, particularly for the smaller steps. This result suggests that the high accuracy preset is better suited for applications requiring precise measurement at smaller scales, while the high density preset remains useful for detailed data capture, albeit with careful interpretation due to increased noise.

5.3.4 Model 4 (10mm to 6mm)

For Model 4, which includes the smallest steps, the high accuracy preset continued to perform well for steps down to 6mm, with accurate mean measurements and manageable variability. However, challenges in segmentation and data processing were encountered with the high density preset, particularly in Pose 2 and Pose 3, where reliable results could not be obtained. This issue highlights the difficulties in using denser data for very fine-scale structures without advanced segmentation techniques.

5.4 Accuracy Assessment

The Intel RealSense D415 performed satisfactorily across all models, with reliable results for steps down to 10mm, especially under the high accuracy preset. This confirms the camera's suitability for metrological tasks involving uniform, low-texture surfaces at the millimeter scale, especially when using the high accuracy preset. The high density preset, while effective for capturing detailed point clouds, introduced more variability and segmentation challenges, particularly at finer scales, suggesting its use should be limited to cases where higher detail is needed, but precision is less critical.

Given the results, the Intel RealSense D415 is suitable for applications requiring a minimum accuracy of 10mm. For steps below 10mm, performance can still be reliable under the high accuracy preset, but care must be taken in interpreting results when using the high density preset.

5.5 Quantization Effects on C2C Distances

In the analysis of Cloud-to-Cloud (C2C) distances across all experiments, quantization effects were consistently observed. Quantization occurs when the stereo camera groups points at similar depth values into discrete bins, as a result of its limited depth resolution. This effect manifests as clustering of points at specific C2C distances, distorting the expected Gaussian distribution of those distances.

One notable example of this phenomenon is observed in the experiment for **Model 1, Pose 2, High Density Preset**. The C2C distance histogram between the stair steps of 30mm and 25mm exhibits a pronounced quantization effect, with a high concentration of points around discrete depth values:

- **Mean C2C Distance:** 0.034284 mm
- **Standard Deviation:** 0.003573 mm

The significant clustering of points, especially in the blue region of the histogram, demonstrates how the camera's depth resolution limits its ability to differentiate between similar depths. As a result, many points are quantized into the same depth bin, which leads to an **artificial reduction in variability**. The lower standard deviation in this case reflects the constrained variability, even though the true surface variation is higher.

This behavior is representative of the quantization effect observed in other experiments as well. Across different poses, models, and presets, the same pattern emerges: points that should be distributed smoothly along the surface are instead grouped into discrete clusters, skewing the Gaussian distribution. While the mean C2C distances remain relatively consistent with the expected values, the standard deviation is artificially reduced, masking the true variability of the measurements.

5.5.1 General Impact of Quantization on Results

Across all experiments, quantization introduces significant challenges in measuring fine geometric details. This effect is particularly noticeable on low-texture surfaces, where the stereo camera struggles to distinguish between similar depths. The impact of quantization can be summarized as follows:

- **Mean Shift:** The mean C2C distance is often skewed toward the most densely clustered depth values, where the camera groups many points into similar quantized bins.
- **Reduced Standard Deviation:** Quantization artificially lowers the standard deviation, giving the appearance of lower variability, when in reality, the depth resolution limits the camera's ability to capture finer surface variations.

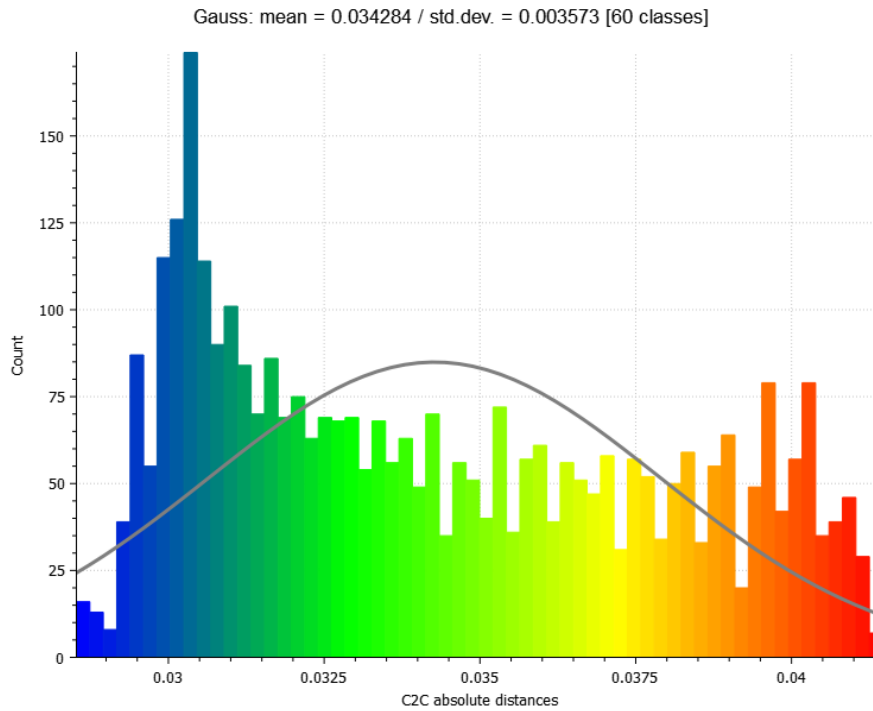


Figure 5.30: Quantization effect in C2C distances for Model 1 (Step 30mm to 25mm), Pose 2, High Density preset.

Overall, the quantization effect consistently distorts the C2C distance measurements, particularly for surfaces with minimal texture or fine detail. The example presented here highlights a typical case, but similar effects were seen throughout the dataset. Therefore, it is critical to consider these limitations when interpreting results from stereo vision systems like the Intel RealSense D415. Although the mean and standard deviation offer useful insights, careful examination of the underlying distribution is essential for understanding the true impact of quantization on measurement accuracy.

6 Conclusion

The goal of this research was to explore and evaluate the feasibility of using the Intel RealSense D415 stereovision camera for the metrological characterization of small-scale, additive-manufactured (AM) components with low-texture, uniform surfaces. The primary motivation behind this work stemmed from the need for accurate, non-contact measurement systems in the quality control of AM products. Traditional contact-based measurement methods face significant limitations in handling fragile or complex components produced via AM. Therefore, this study sought to address these limitations by assessing the reliability and precision of stereovision-based depth measurement, focusing on millimeter-scale parts at close-range distances of 50 cm.

Given the diverse factors that influence AM product quality, including material properties, print temperatures, and slicing parameters, it was essential to establish a robust method for verifying the geometric accuracy of the printed components. This research aimed to contribute to the broader development of enhanced quality assurance techniques for AM, leveraging stereo depth cameras for improved in-process and post-process measurement capabilities.

6.1 Summary of the Proposed Solution

To achieve the research objective, a novel methodology was introduced, named **Stereo Accuracy Assessment in Additive Manufacturing via Plane Fitting (SAAPF)**. This method provides a structured approach to assessing the accuracy of stereovision cameras, with a particular focus on capturing low-texture, millimeter-scale features.

The SAAPF framework integrates several advanced techniques designed to overcome the challenges posed by low-texture surfaces, which often lead to inaccurate disparity calculations in stereo vision systems. The key components of the SAAPF framework include:

- **Plane Fitting:** This technique is used to define precise reference surfaces, ensuring that the stereovision system can be accurately calibrated in environments where traditional methods struggle.
- **Cloud-to-Cloud (C2C) Distance Comparison:** These methods provide quantitative evaluations of spatial deviations between the reconstructed model and the reference surfaces, ensuring dimensional accuracy.
- **Statistical Evaluation:** Using mean and standard deviation analyses, this method assesses the consistency and reliability of the stereo vision system's depth measurements across different poses and presets.

This framework was evaluated on a series of additive-manufactured staircase models with step sizes ranging from 30mm down to 6mm. Testing was conducted under two

operational presets (high accuracy and high density) across three different poses, allowing for a comprehensive evaluation of the Intel RealSense D415 camera's performance.

6.2 Results and Evaluated Outcome

The experimental results across the four test models (ranging from 30mm to 6mm step heights) provided significant insights into the performance of the Intel RealSense D415 camera for metrological purposes. One of the key findings was the influence of quantization on the depth measurements, which had a notable effect on both the mean and standard deviation of the Gaussian distributions derived from the Cloud-to-Cloud (C2C) distance analysis.

- For step sizes down to 10mm, the camera consistently delivered reliable and accurate measurements under the high accuracy preset, with minimal deviation from the true dimensions. This demonstrates the camera's suitability for applications requiring a precision of 10mm or greater.
- The high density preset, while providing denser point clouds, introduced greater variability and noise in the data, particularly for smaller step sizes. This suggests that while high density may be useful for capturing richer data sets, its use is less suitable for applications requiring stringent dimensional accuracy.
- For step sizes below 10mm, particularly in Model 4 (steps from 10mm to 6mm), the camera continued to perform well under the high accuracy preset. However, segmentation challenges were encountered with the high density preset, highlighting the need for advanced processing techniques when dealing with dense data on low-texture surfaces.
- A key finding was the presence of quantization in the depth measurements, which introduced clustering of points at discrete depth levels. This clustering skewed the mean of the Gaussian distribution toward the most common quantized values, while simultaneously reducing the standard deviation due to the grouping of points into fewer depth bins. As a result, the standard deviation may appear artificially lower, masking the true variability in the measurements.

The research successfully demonstrated that the Intel RealSense D415 is capable of achieving metrological accuracy in the range of 10mm for low-texture, small-scale components produced via AM. The SAAPF framework not only validated the accuracy limits of the camera but also provided a robust method that could be adapted for broader applications in the quality control of additive-manufactured products.

6.3 Future Work

This research has laid the groundwork for integrating stereo vision systems into the quality assurance process for AM. However, further work is necessary to refine the SAAPF framework, particularly in improving segmentation techniques for dense point clouds on small-scale, low-texture surfaces. Additionally, exploring the integration of in-process monitoring using stereo vision systems in AM could further enhance the accuracy and efficiency of quality control in AM environments.

Bibliography

- [1] E. Sachs, M. Cima, J. Cornie, *et al.*, „Three-dimensional printing: The physics and implications of additive manufacturing,“ *CIRP annals*, vol. 42, no. 1, pp. 257–260, 1993.
- [2] A. A. Hassen and M. M. Kirka, „Additive manufacturing: The rise of a technology and the need for quality control and inspection techniques,“ *Materials Evaluation*, vol. 76, no. 4, 2018.
- [3] *Additive manufacturing market size, share trends analysis report by 2030 | linkedin*, <https://www.linkedin.com/pulse/additive-manufacturing-market-size-share-trends-analysis-hancock-8vfef/> [Accessed: 2024-07-01].
- [4] K. V. Wong and A. Hernandez, „A review of additive manufacturing,“ *International scholarly research notices*, vol. 2012, no. 1, p. 208 760, 2012.
- [5] T. Peng, K. Kellens, R. Tang, C. Chen, and G. Chen, „Sustainability of additive manufacturing: An overview on its energy demand and environmental impact,“ *Additive Manufacturing*, vol. 21, pp. 694–704, 2018, ISSN: 2214-8604. [Online]. Available: <https://www.sciencedirect.com/science/article/pii/S2214860417302646>.
- [6] P. d’Angelo and C. Wöhler, „Image-based 3d surface reconstruction by combination of photometric, geometric, and real-aperture methods,“ *ISPRS Journal of Photogrammetry and Remote Sensing*, vol. 63, no. 3, pp. 297–321, 2008.
- [7] T. Borgmann, M. Tok, and T. Sikora, „Image guided phase unwrapping for real-time 3d-scanning,“ in *2015 Picture Coding Symposium (PCS)*, IEEE, 2015, pp. 114–118.
- [8] K. Ide and T. Sikora, „Real-time active multiview 3d reconstruction,“ in *2012 International Conference on Computer Vision in Remote Sensing*, IEEE, 2012, pp. 203–208.
- [9] S. Mathavan, K. Kamal, and M. Rahman, „A review of three-dimensional imaging technologies for pavement distress detection and measurements,“ *IEEE Transactions on Intelligent Transportation Systems*, vol. 16, no. 5, pp. 2353–2362, 2015.
- [10] A Barsi, I Fi, T Lovas, *et al.*, „Mobile pavement measurement system: A concept study,“ in *Proc. ASPRS Annual Conference, Baltimore*, 2005, p. 8.
- [11] J.-P. Tarel, S.-S. Ieng, and P. Charbonnier, „Accurate and robust image alignment for road profile reconstruction,“ in *2007 IEEE International Conference on Image Processing*, IEEE, vol. 5, 2007, pp. V–365.
- [12] Z. Hou, K. C. Wang, and W. Gong, „Experimentation of 3d pavement imaging through stereovision,“ in *International Conference on Transportation Engineering 2007*, 2007, pp. 376–381.
- [13] A. B. Slimane, M. Khoudeir, J. Brochard, and M.-T. Do, „Characterization of road microtexture by means of image analysis,“ *Wear*, vol. 264, no. 5-6, pp. 464–468, 2008.

- [14] A. El Gendy, A. Shalaby, M. Saleh, and G. W. Flintsch, „Stereo-vision applications to reconstruct the 3d texture of pavement surface,“ *International Journal of Pavement Engineering*, vol. 12, no. 03, pp. 263–273, 2011.
- [15] E Salari and G Bao, „Automated pavement distress inspection based on 2d and 3d information,“ in *2011 IEEE International Conference on Electro/Information Technology*, IEEE, 2011, pp. 1–4.
- [16] C. Zhang and A. Elaksher, „An unmanned aerial vehicle-based imaging system for 3d measurement of unpaved road surface distresses 1,“ *Computer-Aided Civil and Infrastructure Engineering*, vol. 27, no. 2, pp. 118–129, 2012.
- [17] A. Stumpf, J.-P. Malet, P. Allemand, M. Pierrot-Deseilligny, and G. Skupinski, „Ground-based multi-view photogrammetry for the monitoring of landslide deformation and erosion,“ *Geomorphology*, vol. 231, pp. 130–145, 2015.
- [18] D. Girardeau-Montaut, M. Roux, R. Marc, and G. Thibault, „Change detection on points cloud data acquired with a ground laser scanner,“ *International Archives of Photogrammetry, Remote Sensing and Spatial Information Sciences*, vol. 36, no. 3, W19, 2005.
- [19] D. Lague, N. Brodu, and J. Leroux, „Accurate 3d comparison of complex topography with terrestrial laser scanner: Application to the rangitikei canyon (nz),“ *ISPRS journal of photogrammetry and remote sensing*, vol. 82, pp. 10–26, 2013.
- [20] R. K. Slocum and C. E. Parrish, „Simulated imagery rendering workflow for uas-based photogrammetric 3d reconstruction accuracy assessments,“ *Remote Sensing*, vol. 9, no. 4, p. 396, 2017.
- [21] R. Fan, X. Ai, and N. Dahnoun, „Road surface 3d reconstruction based on dense subpixel disparity map estimation,“ *IEEE Transactions on Image Processing*, vol. 27, no. 6, pp. 3025–3035, 2018.
- [22] A. Berveglieri and A. M. Tommaselli, „Reconstruction of cylindrical surfaces using digital image correlation,“ *Sensors*, vol. 18, no. 12, p. 4183, 2018.
- [23] M. D. Moghari, P Noonan, D. L. Henry, *et al.*, „Characterization of the intel realsense d415 stereo depth camera for motion-corrected ct imaging,“ in *2019 IEEE Nuclear Science Symposium and Medical Imaging Conference (NSS/MIC)*, IEEE, 2019, pp. 1–3.
- [24] M. T. Al Muallim, H. Küçük, F. Yılmaz, and M. Kahraman, „Development of a dimensions measurement system based on depth camera for logistic applications,“ in *Eleventh International Conference on Machine Vision (ICMV 2018)*, SPIE, vol. 11041, 2019, pp. 251–258.
- [25] A. Dawda and M. Nguyen, „Defects detection in highly specular surface using a combination of stereo and laser reconstruction,“ in *2020 35th International Conference on Image and Vision Computing New Zealand (IVCNZ)*, IEEE, 2020, pp. 1–6.
- [26] A. Dawda, M. Nguyen, and R. Klette, „Accurate 3d measurement of highly specular surface using laser and stereo reconstruction,“ in *2019 International Conference on Image and Vision Computing New Zealand (IVCNZ)*, IEEE, 2019, pp. 1–6.

- [27] N. Shatnawi, „Accurate metric reconstructions of historical places using geomatics techniques,“ in *Proceedings of the 2020 3rd International Conference on Geoinformatics and Data Analysis*, 2020, pp. 35–37.
- [28] M. Carfagni, R. Furferi, L. Governi, *et al.*, „Metrological and critical characterization of the intel d415 stereo depth camera,“ *Sensors*, vol. 19, no. 3, p. 489, 2019.
- [29] M. Servi, E. Mussi, A. Profili, *et al.*, „Metrological characterization and comparison of d415, d455, l515 realsense devices in the close range,“ *Sensors*, vol. 21, no. 22, p. 7770, 2021.
- [30] F. Lourenço and H. Araujo, „Intel realsense sr305, d415 and l515: Experimental evaluation and comparison of depth estimation.,“ in *VISIGRAPP (4: VISAPP)*, 2021, pp. 362–369.
- [31] E. Curto and H. Araujo, „An experimental assessment of depth estimation in transparent and translucent scenes for intel realsense d415, sr305 and l515,“ *Sensors*, vol. 22, no. 19, p. 7378, 2022.
- [32] J. G. da Silva Neto, P. J. da Lima Silva, F. Figueredo, J. M. X. N. Teixeira, and V. Teichrieb, „Comparison of rgb-d sensors for 3d reconstruction,“ in *2020 22nd Symposium on Virtual and Augmented Reality (SVR)*, IEEE, 2020, pp. 252–261.
- [33] B. Parr, M. Legg, and F. Alam, „Analysis of depth cameras for proximal sensing of grapes,“ *Sensors*, vol. 22, no. 11, p. 4179, 2022.
- [34] O. A. Adamides, A. Avery, K. Subramanian, and F. Sahin, „Evaluation of on-robot depth sensors for industrial robotics,“ in *2023 IEEE International Conference on Systems, Man, and Cybernetics (SMC)*, IEEE, 2023, pp. 1014–1021.
- [35] Intel, *Depth camera d415*, <https://www.intelrealsense.com/depth-camera-d415/>, Accessed: [insert date of access], n.d.
- [36] Intel Corporation, *Intel realsense d400 series datasheet*, Accessed: 2024-08-22, 2019. [Online]. Available: <https://www.intel.com/content/dam/support/us/en/documents/emerging-technologies/intel-realsense-technology/Intel-RealSense-D400-Series-Datasheet.pdf>.
- [37] A. Bradski, *Learning OpenCV, [Computer Vision with OpenCV Library ; software that sees]*, 1. ed. O’Reilly Media, 2008, Gary Bradski and Adrian Kaehler, ISBN: 0-596-51613-4.
- [38] P. Corke, *Robotics, Vision and Control: Fundamental Algorithms in MATLAB*, 1st. Springer Publishing Company, Incorporated, 2013, ISBN: 3642201431.
- [39] S. J. D. Prince, *Computer Vision: Models, Learning, and Inference*, 1st. USA: Cambridge University Press, 2012, ISBN: 1107011795.
- [40] G. Bradski, „The OpenCV Library,“ *Dr. Dobb’s Journal of Software Tools*, 2000.
- [41] R. Siegwart, I. R. Nourbakhsh, and D. Scaramuzza, *Introduction to Autonomous Mobile Robots*, 2nd. The MIT Press, 2011, ISBN: 0262015358.
- [42] Wikipedia contributors. „Epipolar geometry.“ SVG image. (2021), [Online]. Available: https://en.wikipedia.org/wiki/File:Epipolar_geometry.svg.

- [43] National Instruments, *Stereo calibration*, Accessed: Aug. 18, 2024, 2024. [Online]. Available: https://www.ni.com/docs/en-US/bundle/ni-vision-concepts-help/page/stereo_calibration_in-depth.html.
- [44] C. Ernould, B. Beausir, J.-J. Fundenberger, V. Taupin, and E. Bouzy, „Chapter one - measuring elastic strains and orientation gradients by scanning electron microscopy: Conventional and emerging methods,“ in *Advances in Imaging and Electron Physics*, M. Hýtch and P. W. Hawkes, Eds., vol. 223, Elsevier, 2022, pp. 1–47. [Online]. Available: <https://www.sciencedirect.com/science/article/pii/S1076567022000544>.
- [45] National Instruments, *Stereo image rectification*, Accessed: Aug. 17, 2024, 2024. [Online]. Available: https://www.ni.com/docs/de-DE/bundle/ni-vision-concepts-help/page/stereo_image_rectification.html.
- [46] Intel, *Camera depth testing methodology*, Intel RealSense Technology Documentation, Accessed: insert-access-date-here, 2023. [Online]. Available: <https://dev.intelrealsense.com/docs/camera-depth-testing-methodology>.
- [47] I. Corporation, *Intel® realsense™ product family d400 series datasheet*, Online, Accessed: insert-access-date-here, n.d. [Online]. Available: <https://gzhls.at/blob/1db/6/b/4/c/05be0444ad0c164f3bc668be3bcd1275bd26.pdf>.